Nathaniel Narra

Multiscale Geometric Methods for Isolating Exercise Induced Morphological Adaptations in the Proximal Femur

Tampere 2018

Nathaniel Narra

Multiscale Geometric Methods for Isolating Exercise Induced Morphological Adaptations in the Proximal Femur

Thesis for the degree of Doctor of Science in Technology to be presented with due permission for public examination and criticism in Tietotalo Building, Auditorium TB109, at Tampere University of Technology, on the 23rd of March 2018, at 12 noon.

Doctoral candidate: Narra Girish Nathaniel
                        Computational Biophysics and Imaging Group
                        Faculty of Biomedical Sciences and Engineering
                        Tampere University of Technology
                        Finland

Supervisor: Dr. Jari Hyttinen, Professor
                        Computational Biophysics and Imaging Group
                        Faculty of Biomedical Sciences and Engineering
                        Tampere University of Technology
                        Finland

Pre-examiners: Dr. Timo Jämsä, Professor
                        Research Unit of Medical Imaging, Physics and
                        Technology
                        University of Oulu
                        Finland

                        Dr. Mika Tarvainen, Senior Researcher
                        Department of Applied Physics
                        University of Eastern Finland
                        Finland

Opponent: Dr. Simo Jaakko Saarakkala, Associate Professor
                        Research Unit of Medical Imaging, Physics and
                        Technology
                        University of Oulu
                        Finland

Abstract

The importance of skeletal bone in the functioning of the human body is well-established and acknowledged. Less pervasive among the populace, is the understanding of bone as an adaptive tissue which modulates itself to achieve the most construction sufficient for the role it is habituated to. These mechanisms are more pronounced in the long load bearing bones such as the femur. The proximal femur especially, functions under significant loads and does so with high degree of articulation, making it critical to mobility. Thus, exercising to buttress health and reinforce tissue quality is just as applicable to bone as it is to muscles. However, the efficiency of the adaptive (modelling/remodelling) processes is subdued after maturity, which makes the understanding of its potential even more important. Classically, studies have translated the evaluation of strength in terms of its material and morphology. While the morphology of the femur is constrained within a particular phenotype, minor variations can have a significant bearing on its capability to withstand loads. Morphology has been studied at different scales and dimensions wherein parameters quantified as lengths, areas, volumes and curvatures in two and three dimensions contribute towards characterising strength. The challenge has been to isolate the regions that show response to habitual loads. This thesis seeks to build on the principles of computational anatomy and develop procedures to study the distribution of mechanically relevant parameters. Methods are presented that increase the spatial resolution of traditional cross-sectional studies and develop a conformal mapping procedure for proximal femur shape matching. In addition, prevalent methods in cross-sectional analyses and finite element simulations are employed to analyse the morphology of the unique dataset. The results present the spatial heterogeneity and a multi-scale understanding of the adaptive response in the proximal femur morphology to habitual exercise loading.

.

Preface

Tampere 13.09.2017

Contents

List of Symbols and Abbreviations

2D	two dimensional
3D	three dimensional
BMD	bone mineral density
BMU	basic multicellular unit
CA	cortical area
CT	computed tomography
DICOM	digital imaging and communications in medicine
DXA	dual-energy X-ray absorptiometry
FE	finite element
FFD	free form deformation
FH	femoral head
GPA	generalised Procrustes analysis
GT	greater trochanter
HI	high impact
HM	high magnitude
HSA	hip structural analysis
ICP	iterative closest point
LT	lesser trochanter
MDL	mean descriptor length
MRI	magnetic resonance imaging
OI	odd impact
pQCT	peripheral quantitative computed tomography
QCT	quantitative computed tomography
RBF	radial basis function
RI	repetitive impact
RNI	repetitive non-impact
ROI	region of interest
SAM	statistical appearance model
SPHARM	spherical harmonics
SPM	statistical parametric mapping
SSM	statistical shape model
TA	total area

χ	Euler characteristic of surface
∂M	boundary of discrete mesh
∂S	surface boundary
$\triangle$	Laplace-Beltrami operator
$\boldsymbol{g}$	Riemannian metric of surface
G_s	genus of surface
I	second moment of area
J	polar moment of inertia
M	discrete mesh
S	Surface

List of Publications

Publication 1   Narra N, Nikander R, Viik J, Hyttinen J, Sievänen H. Femoral neck cross-sectional geometry and exercise loading. Clin Physiol Funct Imaging. Jul, 33(4):258-66, 2013.

Publication 2   Niinimäki S, Narra N, Härkönen L, Abe S, Nikander R, Hyttinen J, Knüsel C, Sievänen H. The relationship between loading history and proximal femoral diaphysis cross-sectional geometry. Am J Hum Biol., Jul, 8;29(4), 2017.

Publication 3   Abe S, Narra N, Nikander R, Hyttinen J, Kouhia R, Sievänen H. Exercise loading history and femoral neck strength in a sideways fall: A three-dimensional finite element modeling study. Bone, Nov, 92:9-17, 2016.

Unpublished manuscripts

Publication 4   Narra N, Abe S, Dimitrov V, Nikander R, Kouhia R, Sievänen H, Hyttinen J. Ricci-flow based conformal mapping of the proximal femur to identify exercise loading effects.

Author's contribution

The contribution of the author in each of the 4 published articles compiled in this thesis are summarised below:

Publication 1   Segmentation of cortical bone from MR image data. Development and implementation of algorithms in MATLAB. Processing data to extract features and statistical testing. Manuscript drafting (figures, tables and text).

Publication 2   Co-design of the study and implementation of procedures to extract cross-sectional parameters. Co-drafting of manuscript (text and figures).

Publication 3   Processing of segmented label images to create surface meshes. Contribution towards evaluating procedures for conversion to volume meshes. Contribution towards manuscript text, study results interpretation and review.

Publication 4   Study design and data processing. Development and implementation of all methods in MATLAB. Statistical testing of results. Manuscript drafting (figures and text).

1 Introduction

Robustness of bone is a multifaceted concept characterised by its strength, stiffness, toughness and fatigue resistance. These parameters, derived by applying mechanical engineering principles, are a function of its material as well as morphological properties and help in quantifying robustness. Thus, the structural content and construction in a normal healthy bone is functionally optimal for a given bone mass to achieve necessary robustness. It is a remarkable engineering construct that is not only efficient but also adaptive to the biomechanical demands placed on it in its functional capacity. The adaptive mechanisms of the bone are expressed most clearly in the load bearing long bones such as the femur. Consistent loading that necessitates an increase in robusticity, acts as a stimulus for an adaptive response (Frost,1987). The bones in a skeletal system function within a particular range of motion and loads – which could be said to constitute its functional envelope. With larger range of motion, the direction of the loading can have greater variation depending on the position of the bone within its joint. Thus, some bones may have an expanded envelope, covering a greater range of expected loads and directions. The human femur is the longest and the strongest bone in the skeleton and due to the highly articulated ball and socket joint at the proximal end (hip), experiences loads under multiple directions. In comparison, the distal femur is relatively restricted in its range of motion and consequently the loading directions. This thesis aims to develop methods to enhance the ability to spatially isolate and analyse the relationship between specific habitual loading and effects on bone robusticity.

The human femur is essential for locomotion and various load bearing activities that not only affect health and survival but also the quality of life. As an active biological tissue, it is in a continuous state of maintenance and repair throughout its lifetime. However, the efficiency of these processes declines with age and is also affected by genetic and environmental factors. These factors can significantly impact the structure of the femur and may ultimately compromise its robustness. If the structure of the femur is incapable of absorbing the incident loads effectively, it increases the likelihood of material failure, resulting in a fracture. Hip fractures are a major public health issue facing the elderly population (Kanis 1993). In epidemiological studies, the probability of incidence of osteoporotic fracture after age 50 years was found to be about 20% in men and 50% in women, and increased with advancing age. (Johnell and Kanis, 2005; Lippuner et al., 2009). While the femur does progressively weaken with age, the risk of fracture is not uniform among individuals. The result of adaptive processes during growth and after skeletal maturity can ameliorate these risks. The loss or reinforcement of femoral robustness and the factors responsible can be seen as a cause and effect relationship. Due to the complex interplay between the various cellular activities that lead up to an adaptive response, it is of interest to understand what factors affect or induce what kind of response within the bone histo-morphometry. The ability to isolate such a relationship spatially can be used to target vulnerable regions of the cortex susceptible to fracture.

Any physical activity that loads the proximal femur induces stresses and strains that are either within or beyond its functional capacity. Habitual loading that is above the functional capacity and within material limits necessitates an adaptive response. The response is expressed either in terms of material and/or morphological changes. Loading related adaptations during adolescence and early adulthood are expressed through an osteogenic response, which is reflected in variations in its morphology. These variations are of considerable interest to understand the efficacy of physical activity in alleviating fracture risk through regional or local strengthening (Allison et al., 2015). Established or hypothesized patterns in morphology are also used in anthropology to derive activity patterns of past human populations (Ruff and Larsen, 2014). Traditional methods for evaluating the morphology calculate proxies for bone strength and stiffness at anatomically significant locations (Kaptoge et al., 2007). Morphological shape is evaluated through spatial distribution of a set of anatomical and derived landmarks (Richtsmeier et al., 2002). Morphological distribution is evaluated through cross sectional properties e.g. cortical bone area, total bone area, shape ratios and area moments (Kaptoge et al., 2003). Often the cross-sections are separated into sectors defined with respect to the femoral anatomy (i.e. anterior, posterior, inferior, superior, medial and lateral) and the statistical significance of parameters tested among these sectors. With greater availability of three dimensional (3D) data, methods are being developed to analyse the morphological variations over the entire surface of the femur. Thus, significant regional variations are explored without restricting the analyses to predefined locations (Gee et al., 2015).

Prevalent methods and the evolving field of computational anatomy have resulted in tools that provide results with increasing levels of localisation – i.e. whole bone, cross-sections, sectors and surface regions (Yang et al., 2012; Carballido-Gamio et al., 2015) . The thesis seeks to address the specific area of localising geometric variations in the proximal femur in response to different loading patterns. Employing traditional and computational anatomy methods, we develop procedures that illustrate the patterns at different levels of localisation. The consolidated set of tools are applied to a dataset from a cohort study (Nikander et al., 2009) to explore the effect of habitual loading in female athletes on their morphological parameters and contrast them with active reference subjects. Based on a dataset consisting of magnetic resonance imaging (MRI) of the hip of 111 female subjects, the work presents inferences derived through cross-sectional and 3D analyses reported in 4 separate publications. Publication 1 analyses the cross-sectional shape and circumferential cortical thickness distribution at 2 anatomically significant locations in the femoral neck. The traditional cross-sectional sector based division is extended towards a polar presentation. This enables an analysis for statistical significance within cross sections beyond defined angular spans. Publication 2 studies morphological distribution of the cortex at 3 locations employing traditional metrics defined for the entire cross-section. Group differences in the vicinity of the lesser trochanter are studied in the context of activity reconstruction to determine which site-specific parameters can potentially serve as discriminators of physical activity. Publication 3 studies stress distributions in the femoral neck

volume through computational simulations under fall induced unphysiological (or 'supraphys-iological') loading. The 3D neck volume is divided into octants to compare and contrast statistical significance of the induced stress distributions. Publication 4 studies the 3D distribution of morphological parameters through a novel application of Ricci flow based conformal mapping on the femur surface. This method treats the femur as a topological surface to achieve robust correspondence between multiple shape instances.

2 Background

Locomotion in vertebrates is primarily achieved through the musculo-skeletal system. The muscles act as force generators while the skeletal system, made up of bones and connective tissue, forms an efficient linked system of rigid structures. Other tissues such as ligaments, tendons and cartilage have subsidiary roles and function as flexible linkages and lubricated contact patches. In the skeletal system, mineralized bone is the primary tissue responsible for providing strength and rigidity to the body. It does have a non-mechanical role as a reservoir of minerals and contributes significantly to the metabolic function of the body. The human skeletal system has bones with a wide range of sizes and functionality. Different bones of the skeleton provide varying levels of strength, rigidity and protection. For example, the skull primarily provides protection as a rigid enclosure. The thoracic rib cage provides protection to the vital organs in the thorax, which is accomplished not as a solid shell construction but as a pliable cage. However, not every bone participates directly in locomotion. The bones which are responsible for locomotion can vary in their size, shape and function as well, but primarily provide some combination of load bearing capability, rigid attachment sites and mechanical leverage. The long bones in the limbs function as load bearing bones while providing effective leverages for mobility. The spinal column is an interesting implementation of a protective, strong and flexible linked system, indispensable to mobility. Thus, it is clear that bone morphology can be different according to its primary role. Its functional role under normal 'operation' characterizes its morphology. However, the conditions under which a load bearing bone operates can vary significantly and the response of bone in adapting to such variations can produce distinct histo-morphometric changes. The following chapters will present basic biology of the bone and its behaviour in its biomechanical environment. Subsequently, the proximal femur will be presented in greater detail to finally touch upon the methods employed in studying, characterising and analysing this important anatomy.

2.1 Bone tissue

Bone is a remarkably engineered construct that has major mechanical and metabolic functions in the body. It has a high capacity for repair and adaptation and seeks to achieve functional efficiency for its biomechanical role. Its functional role, and consequently behaviour, varies significantly within the body and is achieved by variations in its composition and layout. The basic building units of the tissue and their hierarchical arrangement will be introduced in the following sections.

2.1.1 Material composition and structure

At the material level, bone is a composite tissue made up of mineral, cells, water, collagen and non-collagenous proteins. The distribution of the organic and inorganic phases varies according to the type of bone, age and pathology (where present). The unique triple helical collagen protein structure is the basic building element which forms the substrate for the tissue (Lees et al., 1994). The mineral, which is the largest component by weight (65%), is an impure form of calcium phosphate (hydroxyapatite: $Ca_{10}(PO_4)_6(OH)_2$). In its biological form, it exists as small crystals shaped as needles, plates or rods. It is distributed in and around the collagen fibres providing rigidity and strength. The collagen fibres themselves provide tensile strength and toughness (Currey, 2003). The non-collagenous proteins, present in small quantities in the extracellular bone matrix, play important homeostatic and metabolic roles (Boskey, 1992; Roach, 1994). All activity within bone is achieved through 4 cell types: osteoblasts, osteocytes osteoclasts and bone lining cells. Osteoblasts are responsible for synthesising bone matrix and are located on the bone surface (periosteum and endosteum). Osteoclasts are multinucleated giant cells responsible for removing bone. Osteocytes are encased within the bone matrix and convey nutrition and mechano-sensory signals responsible for bone turnover. The osteoblasts and osteoclasts are functionally coupled in a normal tissue (Manolagas & Jilka, 1995). Bone lining cells cover inactive (non-remodelling) bone surfaces and together with the network of interconnected osteocytes, provide the cellular system that senses changes in bone loading and subsequently activates osteoclasts and osteoblasts to resorb or produce bone matrix (Miller et al., 1989). It should be noted that these descriptions only summarize the primary roles of these cells. The precise functional pathways and complex interaction between the cellular mechanisms involve many factors that are currently understood and continue to be studied. Finally, water within the bone matrix has an important role in the viscoelastic material behaviour of bone and mechanically strengthens it. Additionally, it participates in the hydrodynamic signalling sensed by the osteocytes and bone lining cells (Weinbaum et al., 1994).

The hierarchical structure of the bone is centred on the arrangement of the collagen proteins, which are aggregated with increasing organisational complexity (Figure 1) (Rho et al., 1998; Launey et al., 2010). The mineralized collagen molecules form fibrils, which are bundled as fibres. These fibres are arranged in thin circular sheets with uniform fibre orientation, called lamellae. Concentric arrangement of these lamellae, form the basic unit of the lamellar bone. Importantly, fibre orientations between each neighbouring ring alternate. The lamellar rings including the central channel (Haversian canal) are called osteons. These osteons are cylindrical in shape with a diameter of 200-250 μm and 1-3mm length, running along the long axis of the bone. At the top of the structural hierarchy, bones consist of trabecular (or cancellous) and cortical (or compact) bone. Trabecular bone is a highly porous, irregular and inter-con-

nected arrangement of lamellae. It is nourished by the red bone marrow which fills and sur-rounds it. The cortical bone is significantly higher in density and forms a hard shell that pro-vides rigidity and strength against external stresses.
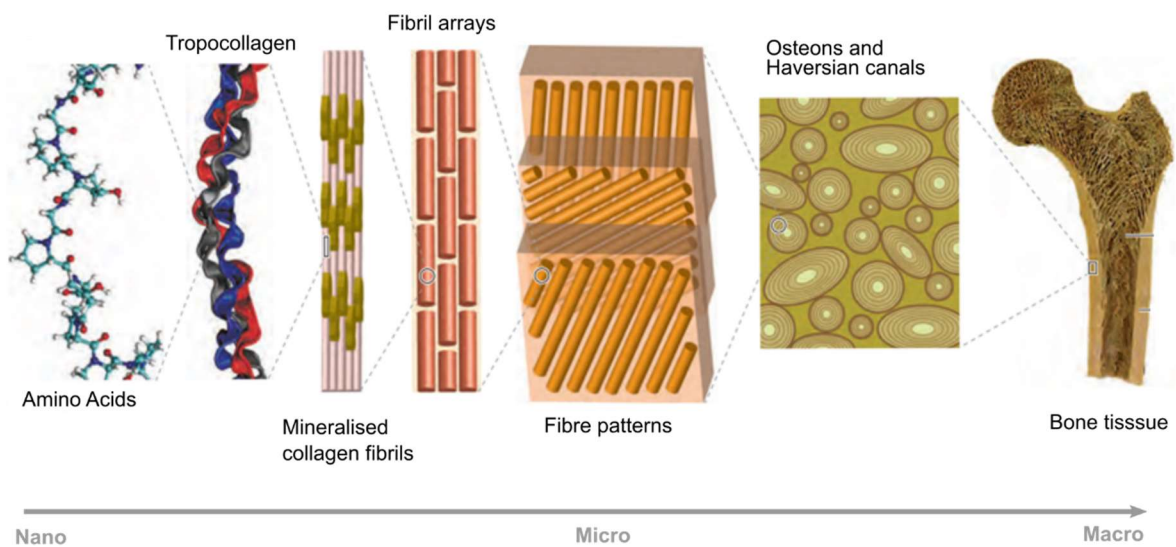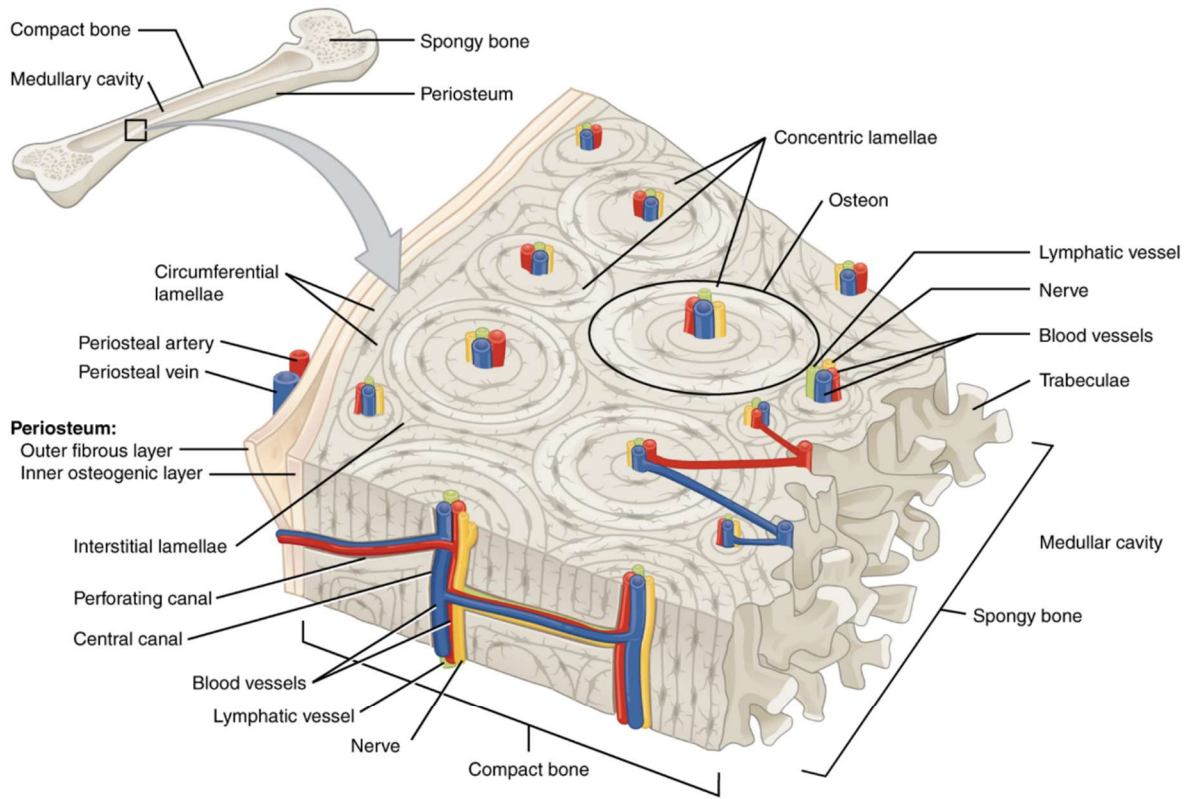
Figure 1 A descriptive schematic of the cortical bone (source: Openstax) and the various levels of the hierarchical construction of the bone tissue (Launey et al., 2010)

2.1.2 Bone strength

The precise construction and composition of different bones in the skeletal system vary according to their function. Their functional purpose and the mechanical demands placed on them result in variations in their mechanical behaviour. The robustness of bone can be gauged by studying its response to, or the ability to resist, the most common mechanical forces such compression, tension, bending and torsion (Figure2).
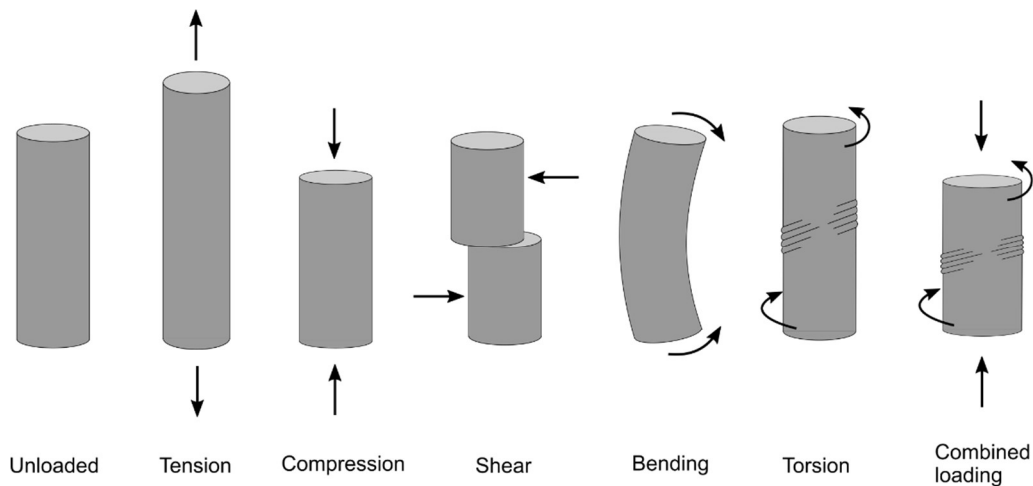
Figure 2 Basic loading schemes experienced by bone. They include simple schemes such as tension, compression and shear. Compound loading patterns such as bending and torsion are a combination of the simple loading patterns.

These forces are produced either by the application of external loads (and the corresponding reaction forces) or internally through muscle contractions at the attachment sites. Mechanical parameters such as strength, stiffness, toughness and fatigue resistance are used to describe behaviour under loads. These parameters are commonly extracted from load-deformation curves, which plot the response to applied loads in terms of observed deformation in an experimental setup (Figure 3). Several mechanically significant parameters such as stiffness (slope of curve), ultimate load (failure load) and work to failure (area under curve) can be calculated from these graphs.
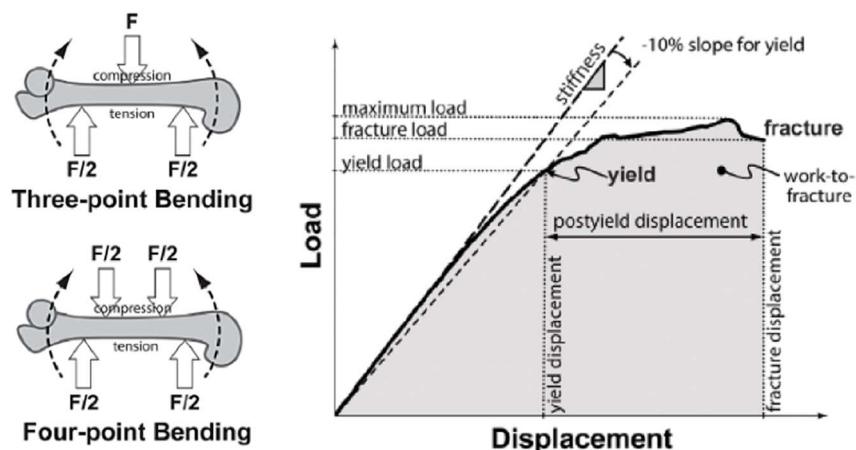
Figure 3 Illustration of common setup for calculating the load-deformation curves of the bone using 3-point or 4-point bending experiments. Bone parameters are calculated from the curves. (Jepsen et al., 2015)

The cortical and trabecular bones differ in their properties significantly. The cortical bone properties are strongly correlated with the degree of mineralization and porosity, accounting for 80% of the variation in its elastic modulus (Currey, 1990). Due to the organisation of the mineralized collagen, the material axis of the cortical bone is along the longitudinal axis of long bones. Due to its transversely isotropic nature, the cortical bone is stronger under longitudinal loading, exhibiting high compressive stresses and tensile strains. It is weakest under transverse loading where the pattern of arrangement of the osteons cannot be leveraged for mechanical strength. The trabecular bone on the other hand, displays much lower strength properties in comparison. However, their properties can vary by a couple of orders of magnitude, even regionally within the same bone (Keaveny & Hayes, 1993). It has a very diverse and heterogeneous structural organization. Its apparent density (i.e. volume fraction) is the most important variable in explaining the variations in their strength (Hernandez et al., 2001; Morgan & Bouxsein, 2008). In the long bones, it is present only in the epiphyses and thought to help in dispersing impact loads at these locations. While the trabecular bone is not primarily involved in load bearing, it does serve secondary functions by buttressing the thinner cortical shells against buckling (Thomas et al., 2009).
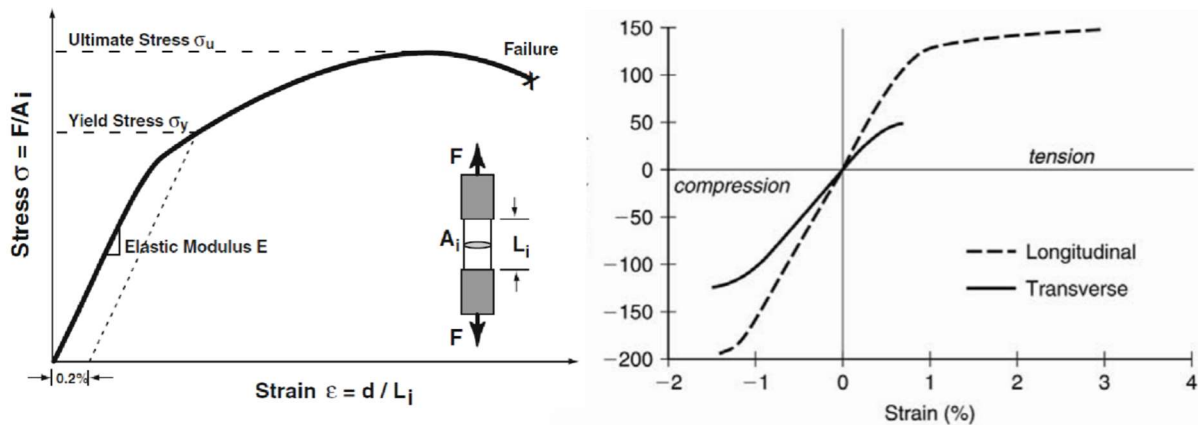
Figure 4 The material properties of bone tissue is typically studied through their response curves under tensile and compressive loading. The mechanical characteristics are quantified through measures of curve properties and area under curves. (Cole & van der Meulen, 2011; Bartel et al., 2006)

The mechanical parameters quantified through the load-deformation curves, describe the macroscopic behaviour of bone, such as the femur under external loading. This behaviour however, is a consequence of material properties as well as geometric/histomorphometric properties. The material properties of bone are described by the analogous stress-strain curves (Figure 4). They discount the geometry effects and describe only the material proper- ties, where mineralization, micro-damage extent and collagen characteristics are important determinants of bone strength. The measurements depend on the loading mode (tension or compression) and on the orientation of the sample with respect to tissue anisotropy (longitu- dinal to transverse). Bone exhibits viscoelastic material properties (Johnson et al., 2010). The elastic modulus and strength of the bone is dependent on the strain rate, such that at higher loading rates the stiffness of bone increases accompanied by a proportionate decrease in ductility (Bartel et al., 2006). Thus, dynamic loading and static loading assume significance in studying bone characteristics. In addition to the intrinsic material properties, additional factors such as the histological distribution of bone material (such as secondary osteons density and size, lamellar bone) are important determinants of bone behaviour (Skedros, 2012).

However, robustness of bone is not exclusively a function of its material quality, micro-archi- tecture and organization. Bone geometry plays an equally significant role, especially in the long, load bearing, appendicular bones. These bones are principally subjected to bending and torsional loads (Martin, 1993). Increased resistance to the consequent stresses have been observed to be a function of bone size (Silva & Gibson, 1997) and bone mass distribution (Crabtree et al., 2001, Bouxsein & Seeman, 2009).

Outer/Inner radii:	r / 0	r / 0.5r	1.25r / 0.75r	1.414r / r	1.5r / r
Cortical area:	1	0.75	1	1	1.25
Section Modulus:	1	0.94	1.7	2.12	4.06
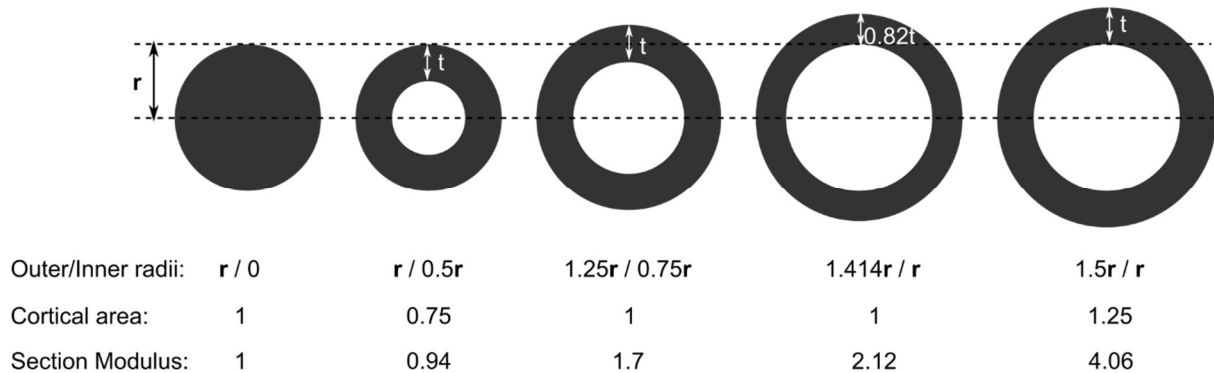
Figure 5 An illustration of the nominal change in strength under loads in response to change in crossectional geometry. The geometry variations are illustrated with respect to the area of a solid circular cross-section of radius **r.** The drifting periosteal and endosteal surfaces (and associated cortical thickness **t**) effects bone strength, i.e. the ability of the bone to resist fracture. Section modulus is proportional to the bending failure strength and the cortical area is proportional to tensile/compressive strength. (modified from Cole & van der Meulen, 2011)

The stiffness of bone increases with size, achieved either through an increase in average cortical thickness or by distributing the bone mass further from the neutral axis of bending (Figure 5). Additionally, regional variations in cortical thickness of a cross-section can alter the shape which can significantly affect the curvature of the bone. These changes in curvature can significantly enhance the bending resistance of bone.

2.1.3 Adaptive processes

Throughout its lifespan, bone manipulates the material quality, microarchitecture, organization and distribution in order to accommodate the loads it is subjected to. Subsequent to osteogenesis, these manipulations occur primarily through the modelling and remodelling processes. The results of these processes are observed as regional (or total) and temporal variations in mechanically relevant material and structural parameters. Besides the genetic and epi-genetic factors, there exist extra-genetic factors that stimulate these processes. These external stimuli can be in the form of habitual loading patterns due to activity, which cause regional variations in stress and strain patterns. The various ontogenic phases of the human bone compiled in Figure 6, illustrate the progressive changes in bone mass and quality and the affecting factors involved.
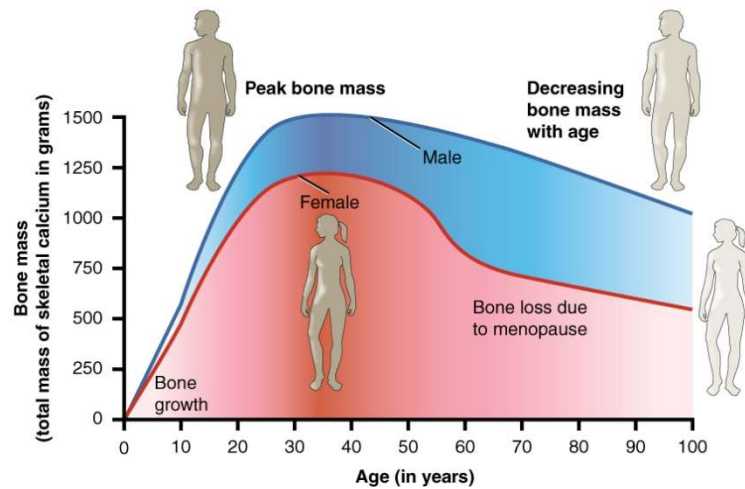
Figure 6 Ontogenic phases of human bone mass in males and females. In females there is considerable loss of bone mass between ages of 45-60 years due to menopause. (source: OpenStax)

It is clear that the distinct contributions of bone material and structural parameters couple towards maintaining the robustness of the bone. Understanding the mechanisms (modelling and remodelling) that affect these individual parameters is essential in understanding the adaptive potential of bone. Modelling induces bone formation or resorption on the periosteal and endosteal surfaces, which are evidenced as changes in the cortical thickness, curvature and overall cross-sectional shape. It could be said that modelling influences the structural layout of the whole bone. Remodelling influences the intra-cortical bone by manipulating the creation and organisation of secondary osteons through the activation of basic multicellular units (BMUs, containing osteoclasts and osteoblasts) (Parfitt et al., 1996). The affects can be observed histologically as changes in osteon density, osteon size, collagen fibre orientation and porosity (Currey 2002; Ehrlich & Lanyon 2002). However, the degree of synergism between the modelling-remodelling processes has not yet been established very well.

2.2 Proximal Femur
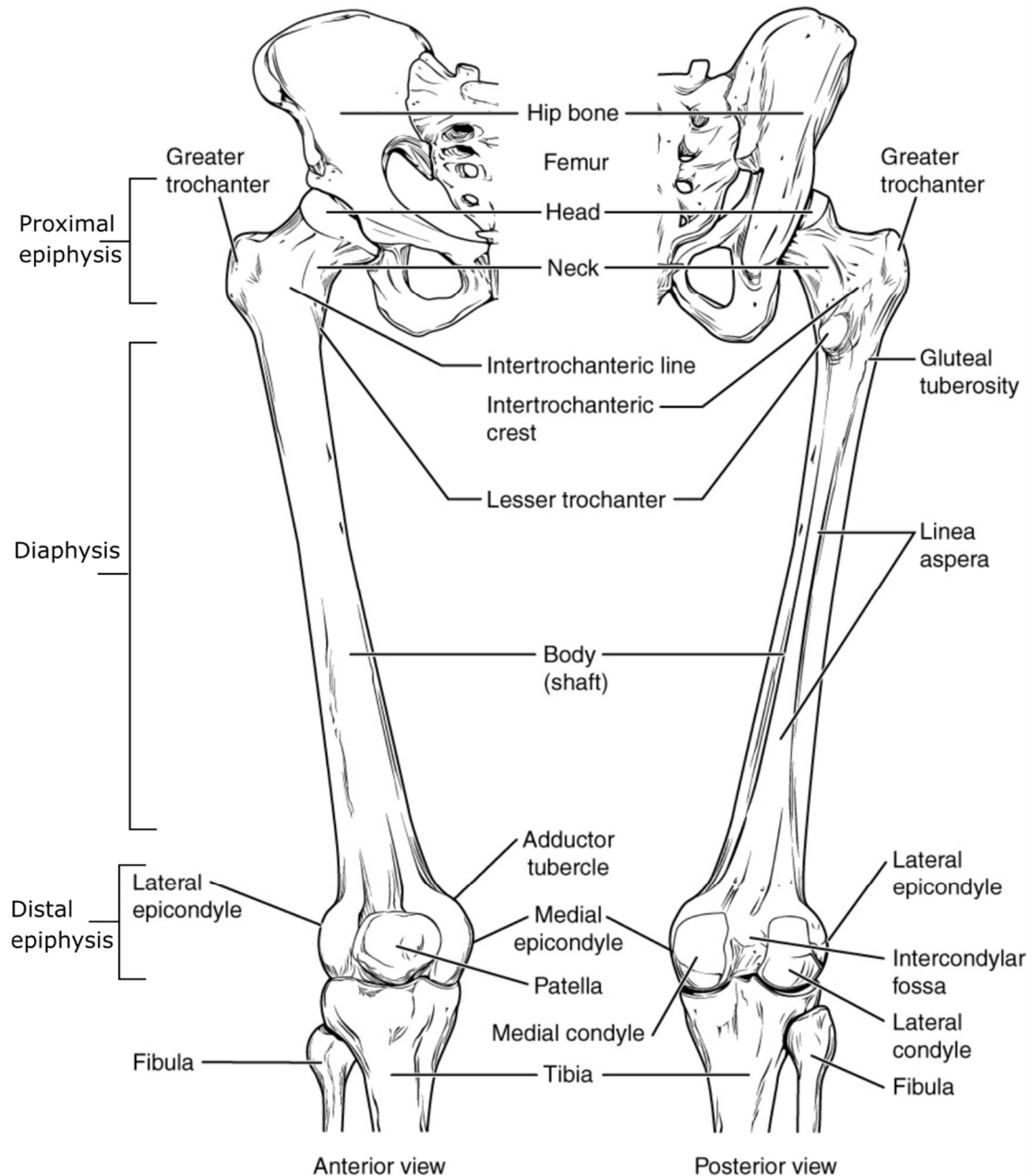
Figure 7 The morphology of the human femur and its anatomical features. (modified from source: OpenStax)

The femur is the longest bone in the human body, making up for about 26.74% of an individ-ual's height with limited variation (Feldesman et al., 1990). Functionally, it plays a significant role in locomotion and mobility as a weight bearing skeletal element and as a rigid attachment site for various muscle groups. It is surrounded by some of the largest and strongest muscle groups such as the quadriceps and the glutes. Activation of these along with others such as the psoas major and psoas minor utilize the femur as an efficient moment arm. A description

of its morphology starts with considering its three sections: proximal epiphysis, diaphysis (femoral shaft) and the distal epiphysis (Figures 7). The femur articulates with the hip at the proximal epiphysis through a ball and socket joint and with the knee at the distal epiphysis. The features contained at the proximal end of the femur include the femoral head, neck, greater trochanter process and the lesser trochanter process. The head is covered with articular cartilage and is the surface that interfaces with the hip joint. The neck connects the articulating head with the main body of the femur. The trochanters are sites of muscle attachments and show great variation in form and relative position between individuals.

Structurally, the design of the femur transfers loads between its interfacing epiphyses, through the diaphysis. From the head to the region of the lesser trochanter, the bone is primarily a thin cortical shell enclosing trabecular bone. While the trabecular bone does not directly contribute towards bone strength and stiffness, they do however, dissipate compressive and tensile loads acting on the femoral head and neck (Rudman et al., 2006). Unlike the hollow thick walled near-cylinder like structure of the shaft, the cortical shell of the proximal femur is relatively thin. The inferior region of the femoral neck is an exception where the cortex thickens to resist the high compressive forces due to loads acting on the head. Under normal 'operation' the absolute tensile stresses are lower than the compressive stresses (Mayhew et al., 2005; Qian et al., 2014). Consequently, the superior region of the neck subjected to predominantly tensile forces is thinner.

The femoral head articulates within the acetabellum socket of the hip, influenced by the neck-shaft angle. This angle represents an advantageous design for bipedal motion that keeps the lower extremity away from the pelvis and allows greater rotation at the hip joint (Isaac et al., 1997). The joint is kept firmly coupled by the surrounding ligaments and muscles. The most significant of the ligaments are the ligamentum teres and acetabular ligaments. Due to the versatility of the joint design, the proximal femur has a significantly large range of motion. Typically, the values are 80°-140° for flexion, 5°-40° for extension, 45°-50° for abduction and 20°-30° for adduction. Internal rotations range from 42°-50° with the knee bent at 90° (Greene & Heckman, 1994; Elson & Aspinall, 2008). Naturally, these values vary slightly between individuals based on their mobility and specific bone morphology. An individual may not utilize the entire available range of motion on a regular basis. Indeed, common locomotive activities such as walking, jogging, climbing stairs and related mobility do not require the extremes of the available ranges. However, they do exercise the proximal femur, albeit to a lesser degree, through nearly all individual movements: extension, flexion, abduction and adduction. When the proximal femur is functionally subjected to loads in various 'poses' during these movements, it results in a complex combination of tensile, compressive and shear forces. Additionally, the regional distribution of these forces is dependent on the loading magnitude, rate of loading, frequency and number of repetitions.

2.2.1 Morphological measures

In order to study the variations and adaptations in the proximal femur, it is essential to establish methods to quantify its morphology. Changes in these quantities can then be analysed to determine trends and the factors responsible. In morphpmetry, morphology is expressed in terms of metrics that represent anatomically significant features and various measures between them (Bookstein, 1991). These metrics can be in one, two or three dimensions and commonly constitute lengths, angles and areas. The geometric properties conveyed by these metrics are used as proxies for biomechanical properties. Morphology is also studied by constructing wireframes based on appropriate landmarks (Figure 8) and subsequent statistical shape analysis (Harmon, 2007). Cross-sectional analyses have been widely used to study the commonly accepted significant regions in the proximal femur: femoral neck, inter-trochanteric region, lesser trochanter region and the proximal shaft (up to mid-shaft).

Femoral Head
1 Most superior point
2 Centre of fovea capitis
3 Most anterior point
4 Most posterior point
5 Volumetric centre of head
6 Intersection: neck axis with head surface

Head-Neck junction
7 Most superior point
8 Most inferior point
9 Most anterior point
10 Most posterior point

Femoral neck
11 Most superior point
12 Most inferior point
13 Most anterior point
14 Most posterior point
15 Neck centre: smallest crossection along neck axis

Greater trochanter
16 Most superior point
17 Centre: trochanteric fossa
18 Most lateral point
19 Intersection of neck axis with trochanter surface
20 Intersection of shaft axis with trochanter surface

Lesser Trochanter
21 Tip of trochanteric process
22 Postero superior point

Inter-trochnateric region
23 Intersection: shaft-neck axis
24 Superoinferior midpoint of intertrochanteric crest
25 Posterosuperior point on intertrochanteric crest

Proximal shaft (inferior to lesser trochanter)
26 Most medial point
27 Most lateral point
28 Most anterior point
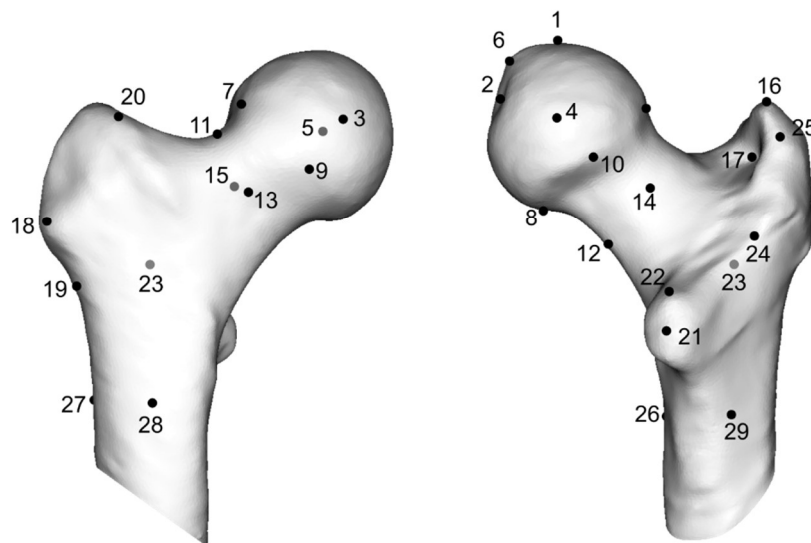29 Most posterior point

Figure 8 Illustration of commonly landmarked features of the proximal femur typically employed in morphometry/shape analysis studies. These examples are compiled from the works of Harmon (2007), Holliday et al. (2010) and Väänänen et al. (2012).

2.2.2 Morphological variations and adaptations

The modelling and remodelling mechanisms work on the bone continuously throughout its lifetime, as part of a feedback system aimed at biomechanical efficiency. There are multiple factors that trigger and control these mechanisms which may be coupled to the ontogenic phase that the bone is in: attainment, maintenance or senescence. These influences can be broadly considered as genetic, epigenetic and extra-genetic (Skedros et al., 2007). Genetic and epigenetic factors are those that are inherited and their expression induces variations and adaptations that are entirely intrinsic to the individual biology. Extra-genetic factors in contrast, are external to the biological makeup of the individual. While these factors may not be heritable, it must be acknowledged that they do act on the inherited biological machinery. The following paragraphs will briefly introduce these factors behind morphological variations in the proximal femur.

Ontogenic Variations: During osteogenesis and the initial growth phase the femur undergoes marked changes in size and shape (Djuric et al., 2012). The differences in body proportions, skeletal development and immature gait, load the femur in distinct patterns from adults. Greater medio-lateral ground reaction forces were found to affect the mid-shaft shape of young walkers (Cowgill et al., 2010). The second major growth spurt that occurs after puberty induces changes that take the femur to maturity. The collo-diaphyseal angle decreases, femoral neck widens, the fovea position lowers and the greater and lesser trochanters increase in size (Pujol et al., 2014; Pujol et al., 2016). During this period of adolescence, the velocity of bone mass accrual is at its peak, reaching maximum values by early adulthood. In males, peak cross-sectional area and bending resistance is achieved by about age 22.3. In females, the peaks values are achieved by about age 21 (Jackowski et al., 2011). The post-maturity morphology of the femur is maintained till the senescence phase, where the inability of the body to maintain the material quality of bone results in morphological changes. In females, the section modulus at the narrow neck and the shaft remains nearly constant into their 50's, declining thereafter. In males, there is a modest decrease in the section modulus at the narrow neck until the 50's (constant thereafter), while the shaft section modulus was static till the 50's and subsequently increased steadily (Beck et al., 2000). The results indicate that the decreased robustness due to loss of BMD at these sites (and possibly increased porosity) is mitigated by the expansion of the sub-periosteal diameter. This widening mechanically offsets the net loss of medullary bone mass (at the cost of increased brittleness); suggesting that age-related loss of bone mass does not necessarily translate into proportional reduction in mechanical strength.

Genetic and epi-genetic variations: Apart from age effects, pathological conditions and abnormal ontogeny, sex and ethnicity also account for certain variations observed between populations. For example, among a sample of 3,305 North Americans including Black, Hispanic, White and Asian men (>65 yrs), femoral neck dimensions revealed similar mean neck volumes. However, Black and Asian men had thicker cortices (Marshall et al., 2008). In another study

of the proximal femur of 1190, examining Black, Hispanic and White men, greatest bone strength was observed among the Black men. The greatest age related difference was observed among the Hispanic men (Travison et al., 2008). Femoral head diameter, calcar-canal width ratio and neck-shaft angle (calculated from radiographs) were found to be differing significantly amongst the Chinese, Indian and Malay women (Tang et al., 2016). In a study of 214 peri- or postmenopausal women (46-85 years), thicker cortical bone and lower cortical buckling ratio were found in Asians in comparison to their American, European, and African counterparts (Kim et al., 2011). Sexual dimorphism is reflected in the femur most commonly through a combination of all or some metrics such as femoral head diameter, bone length, mid shaft cross-sectional geometry and distal epiphyseal measures (Purkait et al., 2004; Brown et al., 2007). The precise set of parameters that are sufficient for reasonably accurate discrimination depends on the ethnicity of the population.

Adaptations to activity: Habitual physical activities involving the proximal femur can induce loads varying in magnitude, rate of generation and direction, resulting in differences in regional distribution of these loads. The existing morphology, according to its ability to accommodate these loads, will experience varying magnitudes of strains. Depending on where they fall within the different strain zones of the mechanostat (Frost 1987; Figure 9), these localized or regional strains can act as stimuli for bone adaptation (Thompson et al., 2016).
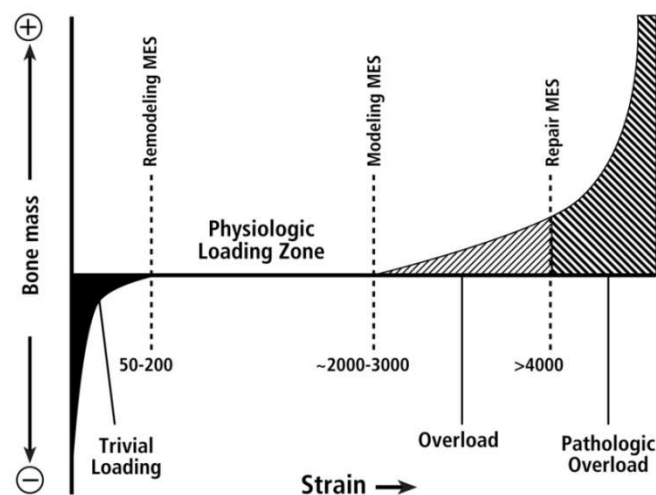
Figure 9 The four zones according to the Mechanostat hypothesis where in incident strains effect the remodelling and modelling processes effecting bone mass. 1) Trivial loading zone: remodelling processes are activated when the strains are below the minimum effective strain (MES) of remodelling. 2) Physiologic loading zone: when strains are between the remodelling MES and modelling MES, remodelling and modelling processes are relatively balanced (while under hormonal and metabolic influences). 3) Overload zone: strains above the modelling MES result in addition of lamellar bone through increased modelling processes. 4) Pathological overload: strains above repair MES result in rapid addition of woven bone to the bone surface. In the extreme (>15000) it can result in initiation of fracture in the material. (Skedros et al., 2001)

Establishing a one to one relationship between activity and bone adaptation is not straightforward, since other factors (strain rate, strain distribution, number of repetitions and frequency)

are also important in determining the effectiveness as the stimulus (Nikander, 2009; Lanyon, 1987; Mcleod & Rubin 1992, Rubin & McLeod, 1994; Rubin et al., 2002). In the context of the highly articulate hip joint, regional strain distribution is of significance. Lanyon (1987) proposed that loading directions that differ from common predictable loading are more osteogenic. Thus, any activity that stresses the proximal femur in a manner different from simple locomotive patterns has the potential to be more effective as a stimulus. When such activities become habitual, even with low repetitions but consistent in frequency and rest, they can be effective stimuli for adaptation (Turner & Robling, 2003; 2005). Measuring strains induced in the bone (in-vivo) as a result of activity is however very difficult to achieve and as a result very few studies have attempted such measurements (Al Nazer et al., 2012). The difficulty in accessing the proximal femur in the hip further increases the difficulty in realising such projects. In-vitro measurements have been performed on cadaver samples through mechanical testing under realistic loading conditions (Cristofolini et al., 2009; Grassi et al., 2014). In-vivo measurements based on strain gauges have been used to gather strain patterns post-operatively (Aamodt et al., 1997). Specific MRI protocols have been developed for non-invasive in-vivo measurement of strains in the articular cartilage at the tibiofemoral joint (Chan and Neu, 2012; Chan et al., 2016). While these methods are promising, studying the proximal femur biomechanical environment is a significant challenge and solutions for 3D strain measurement in the cortex remain elusive. Given this paucity of methods, strains have been indirectly estimated through measuring ground reaction forces and kinematic modelling of the lower extremity (Daly et al., 1999; Heikkinen et al., 2007; Heinonen et al., 1996, 2001; Vainionpää et al., 2006; van der Bogert et al., 1999; Weeks and Beck, 2008; Weeks et al., 2008; Bassey et al., 1995; Ebben et al., 2010; Wang et al., 2012; Tolly et al., 2014; Puddle and Maulder, 2013; Nin et al., 2016). Some common activities and the associated load magnitudes and rates are listed in Table 1 and illustrated in Figure 10

Table 1 Various activties and sports measured for maximum vertical ground reaction forces and loading rates (rate of force)

Activity	Peak GRF (BW)	Rate of Force (BW/s)	References
Walk (3 km/h)	1.5	8	Vainionpää et al. 2006; Ebben et al. 2010
Walk (5 km/h)	1.85	20	van der Bogert et al. 1999; Heinonen et al. 2001; Vainionpää et al. 2006; Weeks and Beck 2008; Ebben et al. 2010
Walk (6km/h) + 32kg load	1.92	35	Wang et al. 2012
Stairs ascent	1.14	6	Stacoff et al. 2005
Stairs descent	1.6	14	Stacoff et al. 2005
Side-step	2.9	120	Weeks & Beck 2008
Hop	3.4	50	Weeks & Beck 2008
High jump take off	3.5	120	Weeks & Beck 2008
Long/triple take off	3.5	140	Weeks & Beck 2008
Heel drop	3.6	40	Weeks & Beck 2008

Running stop & turn	1.8	40	Weeks & Beck 2008
Running (6 km/h)	2.34	28	Ebben et al. 2010
Running (13 km/h)	3.9	87	Heikkinen et al. 2007; Weeks & Beck 2008; Ebben et al. 2010
Running (18 km/h)	4.03	183	Ebben et al. 2010
Jump	4.7	70	Vainionpää et al. 2006; Weeks & Beck 2008
Foot stomp	4.6	470	Weeks & Beck 2008
Drop jump	6.5	170	Vainionpää et al. 2006; Heikkinen et al. 2007; Weeks & Beck 2008;
Powerlifting	3.25	3	Fauth et al. 2010
Power clean 60%wt	3	16	Comfort et al. 2011
Cricket (bowling)	9	346	Feros 2015
Basketball	7.29	213	Nin et al. 2016
Gymnastics (landing)	10.4	610	Daly et al. 1999
Steeplechase	6	282	Kipp et al. 2017
Cyclocross	2.9	63	Tolly et al. 2014
Parkour	3.2	83	Puddle & Maulder 2013
Slalom skiing	7.8	-	van der Bogert et al. 1999;
Mogul skiing	10.35	-	van der Bogert et al. 1999;
Triple jump second contact	22	-	Heinonen et al. 2001
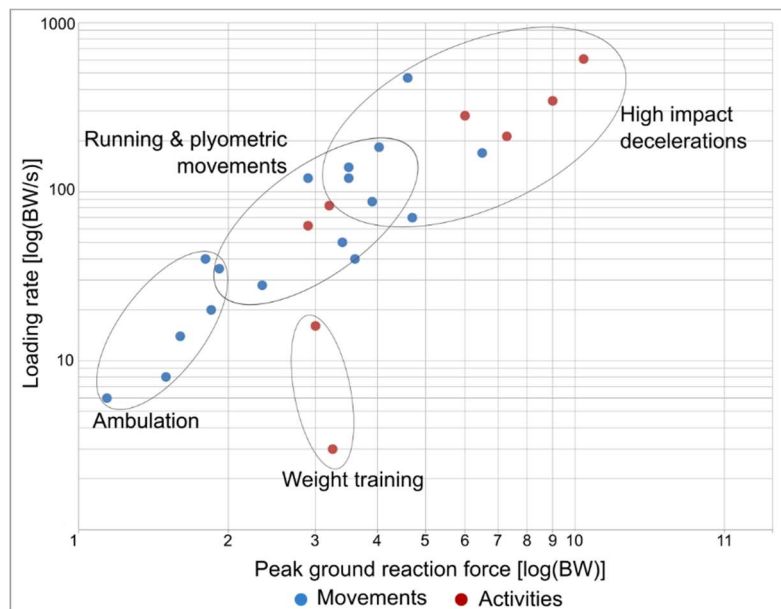
Figure 10 Illustration of the relative positions of different activities and sports with respect to the typical maximum ground reaction forces (GRF) and maximum loading rates. These values represent the maximum magnitudes measured by various studies (listed in Table 1). Simple movements are plotted in blue and sports, which are commonly a sequence of movements, are plotted in red. The encircled clusters are very broad categorizations of the underlying activity drawn for convenience. The axes are on a logarithmic scale.

The beneficial effects of weight bearing physical activity on bone robustness and health is well established (Fuchs et al., 2017). The evidence is based on studies on data from habitual practitioners (exercise), randomized controlled trials and past populations. Cohort studies collect the femoral morphology from subjects with established pattern of activity, quite often sports or exercise regimen practiced either professionally or recreationally (Nikander 2009, Nikander et al., 2009; Scerpella et al., 2016; Dowthwaite et al., 2012; Dowthwaite and Scerpella, 2009). The effect of prescribed activity has been studied in controlled trials, where the intervention is often administered as targeted exercise programmes (e.g. high-impact loading, low-impact weight bearing, resistance training, balance and agility exercises). Other valuable sources of data are the bones of past populations which are categorized by appropriate factors: e.g. gender, ethnicity, socio-economic status, nutritional habits and physical activity. Studying the effects on proximal femur bone structure and bone mass distribution is commonly based on DXA scans and pQCT cross-sections (femoral neck and intertrochanteric): pre- and peri-pubertal girls and boys (Fuchs et al., 2001; MacKelvie et al., 2004; Macdonald et al., 2008; Fritz et al., 2016), postmenopausal women (Hamilton et al., 2010). The established effects and hypotheses through these studies have been applied in reverse by anthropologists. Referred to as activity reconstruction, they serve to explore the factors contributing to the differences observed in morphology. These factors can provide information regarding the likely physical activity patterns past populations were engaged in, which can give insight into their socio-economic environment.

2.3 Methods in analysis

Procedurally, any analysis of the morphology starts with extracting the defined morphological parameters. Direct manual measurement on ex-vivo samples is the simplest method, often performed on archaeological and cadaver samples. However, this can be tedious and also limits the morphological variation than can be analysed. Tools such as microscribes have improved working on such samples (Holliday et al., 2010) by digitizing the operator selected feature points in 3D. Laser and optical scanning methods have been used to remove operator involvement by densely sampling the surface to represent it as a point cloud (Slizewski and Semal, 2009; Filiault, 2012; Verim et al., 2013; Rein and Harvati, 2014; White, 2015). These methods are limited to analyses of only the surface based metrics of ex-vivo samples – positions, distances, shapes and cross-sectional contours. To calculate metrics based on internal structure and distribution of bone in ex- and in-vivo samples, projection (DXA) and tomographic (CT, pQCT, MRI) imaging methods have been used (Macintyre and Lorbergs, 2012). Neutron imaging modality has also been used for acquiring bone densitometry data (Sartoris & Resnick, 1990; Moghaddam et al., 2008). With ex-vivo samples, an imaging modality can be chosen according to the required scale and type of features that are to be extracted and analysed. For these samples, radiographic methods are extensively used as ionizing radiation

is not of concern. However, for in-vivo imaging radiation dosage is of prime concern and there-fore, dictates the imaging modality than can be used for a study. The various modalities com-monly used for imaging bone are illustrated in Figure 11 along with the common features that are extracted from them.
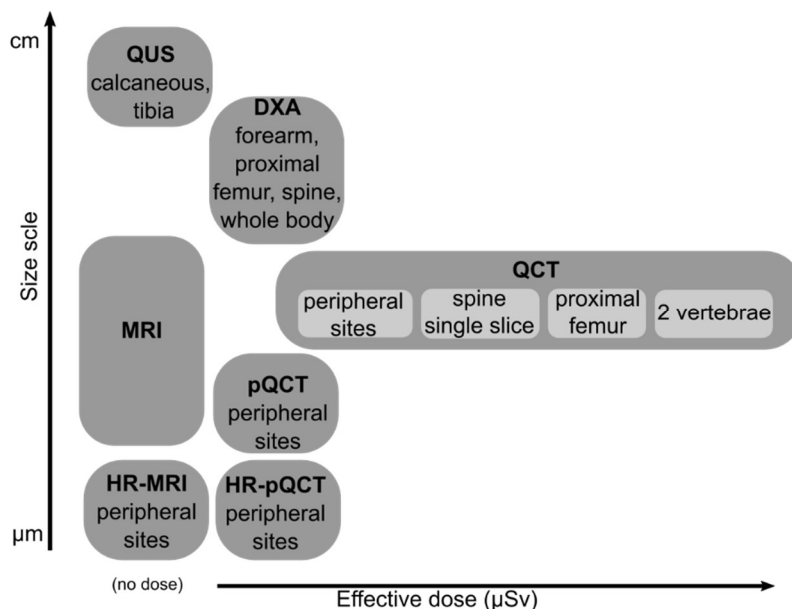
Figure 11 Various imaging modalities employed in studies to analyse the morphology of bone. This figure illustrates the different imaging modalities and their relative positions in terms of radiation dosage and imaging accuracy (adapted from Macintyre et al 2012)

Thus, the amount of radiation dosage administered needs to be justifiable, especially for healthy individuals recruited in cohort studies. Consequently, DXA has been the most common modality of imaging for assessing bone health. Besides direct measurements of morphology from these images (e.g. neck width, neck axis), the hip strength analysis (HSA) technique has been employed to obtain additional bone structural parameters from DXA images (Beck, 2007, Bonnick, 2007). As it is a projection image which averages volumes of bone over a projected area, the spatial information in the 3rd dimension is lost. Thus, the periosteal and endosteal contours of the cortical bone in the cross-sectional plane cannot be precisely derived. At the femoral neck, the HSA method models the cortical bone as a uniform circular distribution ac-counting for 60% of bone mass (Beck and Broy, 2015). These assumptions are an oversim-plification of the spatial distribution of the cortical bone and have been known to overestimate the approximated thickness measure (Kersh et al., 2013). These irregularities can subse-quently obscure the presence (or absence) of regional adaptations at important sites (Järvinen et al., 1999) such as the superolateral cortex of the femoral neck.

The limitations of analyses based on 2D projection images have led to the development of techniques for 3D image data. Radiation tomography based modalities (CT, pQCT) are often

the most accurate methods available for obtaining the structure as well as the material characteristics (density) of the bone. However, administered radiation dosage is strictly restricted in the ethical collection of data from healthy human subjects, which limits the available 3D modalities to pQCT and MRI. Unlike pQCT, in which dosage can only be kept low for peripheral sites, MRI is much more widely applicable. This versatility comes at a slight cost of image resolution and long imaging times. However, technological developments have made MRI an effective way to acquire bone morphology (Neubert et al., 2017), albeit without the material density information. Image processing and segmentation procedures represent the anatomical shape as either surfaces or labelled volumes. Subsequently, features such as area, volume, thickness and landmark relative positions are calculated over them. These parameters are calculated as bulk parameters in regions of interest (ROI) whose extent, location and demarcation is defined according to the study design. In some studies, the selected cross-sections are divided into anatomical sectors (quadrants, octants or more). These studies then report observations and make inferences with respect to these intuitive anatomical orientations. They convey the findings with greater resolution (within cross-sectional plane) when compared to bulk parameters and help localize the factors and their effects with respect to the pose of the femur at specific cross-sections (Nikander et al., 2009; Johannesdottir et al., 2013; Abe et al., 2016).

In recent years, methods have been developed that go beyond pre-defined ROI's towards spatially dense, whole structure analysis; often at or below the resolution of the native image data. This methodology, known as computational anatomy, is a collection of algorithms employing methods in image analysis, geometry and statistics to analyse and model anatomy and the variations of relevant features across populations (Carbadillo-Gamio and Nicolella, 2013, Pennec and Fillard, 2015). Thus, without assuming significance of ROI's, the features across the spatial domain (curves, surfaces or volumes) for multiple subjects can be compared and their statistical significance visualized as colour maps (Treece et al., 2010). To name a few of their major applications, they have been used in conjunction with in-vivo QCT and clinical CT data, to study the risk factors for hip fracture (Li et al., 2009; Poole et al., 2012; Johannesdottir et al., 2014), age effects (Carballido-Gamio et al., 2013), spaceflight effects (Li et al., 2007) and effect of drug treatment (Poole et al., 2011). There are 2 steps at the core of the computational anatomy approach – spatial normalization and statistical testing. They are usually preceded by shape representation and feature extraction from image data. Spatial normalization involves finding correspondence between anatomical regions of multiple instances of shapes with respect to a common standardized space. Due to the large number of corresponding points that are involved in statistical inference calculations, corrections need to be made for multiple comparisons. In numerous studies dealing with the proximal femur, statistical parametric mapping (SPM) based on random field theory has been employed (Friston et al., 1994). The MATLAB implementation is available as the SurfStat toolkit (Worsley et al., 2009).

2.3.1 Shape registration

In large group studies, statistical shape and appearance models (Cootes et al., 1995, Castro-Mateos et al., 2014) are frequently used to put all the individual femur shape instances in a common framework. The shapes are commonly represented as meshes or gridded data (pixels in 2D, voxels in 3D). A mesh is defined by nodes and the connectivity between them. Nodes represent specific locations relevant for describing the shape or geometry of the anatomy. These can be boundaries in 2D, surface of a volume in 3D, volume meshes with nodes also representing the interior of the body. Implicitly describing shapes through gridded data is performed through distance maps (Aslan et al., 2010) and intensity values within the object of interest (Li et al., 2009). The most frequently used approaches for establishing correspondence are:

(1) Explicit landmark placement: A common method used with 2D images where an expert manual identifies the landmarks (Harmon, 2007). The landmarks can also be identified semi-automatically based on shape feature detection (Väänänen et al., 2015).

(2) Mesh deformation: A reference mesh is deformed to fit every target mesh, often with the objective of producing a set of iso-topological meshes (Bryan et al., 2009; Grassi et al., 2014a). The training set can be surface meshes, volume meshes or intensity volumes (binary volumes, distance maps, etc).

(3) Volume to volume: A reference image is selected and segmented. Then, the image volume (Whitmarsh et al., 2011; Bonaretti et al., 2014) or the segmented volume (Fritscher et al., 2007) is deformed to adapt it to all the training samples.

In these approaches, the computational process of transforming the source to the target is called the registration step. Rigid alignment through Generalized Procrustes Analysis (GPA) (Gower, 1975) is a common first step in the landmark based registration process for normalising pose and scale. An equivalent method for the volume to volume approach is based on mutual information developed for QCT image volumes (Li et al., 2006). Due to the presence of non-isometric variations in bone geometry, rigid alignment has to be supplemented with non-rigid (elastic) registration for greater accuracy. However, this is a challenging task, especially for shapes with complex topologies or in the presence of noise. Numerous algorithms have been developed and applied for non-rigid registration of the femur for the different correspondence approaches. These include methods based on – multi-scale 3D cross-correlation (Collins et al., 1994; Li et al., 2007), iterative closest point (ICP: Besl and McKay, 1992; Treece et al., 2010; Tree and Gee, 2015), B-splines (Bryan et al., 2009), log-demons (Vercauteren et al., 2009; Bonaretti et al., 2014), radial basis functions (Grassi et al., 2011; Arezoomand et al., 2015), greedy algorithms (Wang and Shi, 2017), spherical harmonics (SPHARM) (Styner et al., 2003, 2006; Funkhouser et al., 2003; Frome et al., 2004) and minimum descriptor length (MDL) (Davies et al., 2002).

Additionally, methods have been developed for surface registration that find application in other fields or anatomies. These are based on – surface curvature (Vemuri et al., 1986), regional point representation (Sun and Abidi, 2001; Ruiz-Correa et al., 2003), shape distributions (Osada et al., 2002), physics-based deformable models (Terzopoulos et al., 1988), free form deformation (FFD) (Huang et al., 2003) and Level-sets (Malladi et al., 1996). Of interest are harmonic and conformal geometric methods that have been developed for numerous applications in computer vision (Angenent et al., 1999; Zhang and Hebert, 1999; Haker et al., 2000; Levy et al., 2002; Gu et al., 2994; Sharon and Mumford, 2004; Wang et al., 2005a,b; Wang et al., 2007; Zeng et al., 2008). They are an elegant way of handling non-rigid deformations in complex topologies through a landmark-free approach (Lui et al., 2010; Yeo et al, 2010). One such approach based on Ricci flow, first introduced in differential geometry by Hamilton (1988), is a powerful curvature flow method in geometric analysis. It operates by deforming the Riemannian metric of the manifold (surface) such that the curvature evolves according to a heat diffusion process. Eventually, the deformed metric results in a uniformization where the curvature is constant everywhere on the manifold. This produces a conformal deformation of shapes to one of three canonical domains ($\mathbb{R}, \mathbb{S}, \mathbb{H}$), thereby transferring shape analysis problems from a 3D domain to 2D. Cylindrical projection has been used in studies of hominoid long bones (Naoki, 2012). However, this projection method does not produce point-to-point homology. Conformal mapping of the proximal femur as yet has not been applied for 3D feature studies.

2.3.2 Ricci-flow based conformal parameterization

This section will briefly introduce the motivation behind Ricci-flow and the terms and definitions critical to understand this concept. The text has been summated from various works of Xianfeng Gu and colleagues (Gu et al., 2004, Zeng et al., 2008, Yang et al., 2009; Zeng et al., 2010) which contain algorithmic details. For the theoretical development and necessary proofs, being beyond the scope of this thesis, the readers are referred to the books by Chow & Knopf (2004) and Zeng & Gu (2013).

Any surface in the Euclidean space is characterised by – topology, Riemannian metric and embedding. Topology of the surface is described by the Euler characteristic, which can be calculated for a closed surface S of genus G_s (intuitively determined by the number of 'handles') as

$$\chi(S) = 2 - 2g_S \qquad \textit{closed surface}$$
$$\chi(S) = 2 - 2g_S - b \qquad \textit{open surface with b boundaries}$$

Definition – Riemannian metric: *For a surface S, the Riemannian metric is a tensor $g = (g_{ij})$ which is positive definite and defines an inner product for the tangent space of S.*

Riemannian metric defines measures such as angles and lengths of tangent vectors through the first fundamental form. For two tangent vectors $\mathbf{v}_1$ and $\mathbf{v}_2$ on the tangent plane at a point $p \in S$ (in terms of local coordinates (x, y)), the inner product is defined as

$$\langle \mathbf{v}_1, \mathbf{v}_2 \rangle_g = \sum_{ij} g_{ij} dx_i dy_j$$

And the angle between the two vectors measured by $\mathbf{g}$ is given by

$$\theta_g = \cos^{-1} \frac{\langle \mathbf{v}_1, \mathbf{v}_2 \rangle_g}{\sqrt{\langle \mathbf{v}_1, \mathbf{v}_1 \rangle_g \langle \mathbf{v}_2, \mathbf{v}_2 \rangle_g}}$$

The second fundamental form describes the embedding of the surface in the Euclidean space. The first and second fundamental forms together determine surface uniquely up to rotation and translation in $\mathbf{R}^3$. The Gaussian curvature of a surface at a point, measures the proximity of its neighbourhood to a plane (i.e. zero curvature). It is determined by the Riemannian metric, is independent of its embedding in space, and constrained by the surface topology.

Definition – Gauss-Bonnet: *The total curvature of a metric surface $(S, \boldsymbol{g})$ is given by its Euler number $\chi(S)$*

$$\int_S K dA_g + \int_{\partial S} k_g ds = 2\pi \chi(S)$$

In parameterization, the surface is mapped onto to a canonical domain. When the target domain is planar, it is equivalent to finding the Riemannian metric that induces 0 Gaussian curvature over the entire surface. In Ricci-flow, the Gaussian curvatures are modified through scaling of the Riemannian metric.

Definition – Conformal deformation: *Two Riemannian metrics on S are conformal, if there is a function defined on the surface $u: S \to \mathbb{R}$ such that $\bar{\mathbf{g}} = e^{2u} \mathbf{g}$, where u is called the <u>conformal factor</u>*

It can be shown that for the two conformal metrics, the angles remain constant for tangent vectors defined at the point such that $\theta_g = \theta_{\bar{g}}$. If the surface metric $\mathbf{g}$ is conformal to the Euclidean metric $dx^2 + dy^2$, then they are called isothermal coordinates.

Definition – Gaussian curvature: *Let S be a surface with a Riemannian metric $\mathbf{g}$ and (x, y) be isothermal coordinates of S, then the Gaussian curvature is defined as $(x, y) = \Delta_g u(x, y)$, where $\Delta_g = \frac{1}{e^{2u(x,y)}} \left(\frac{\partial^2}{\partial x^2} + \frac{\partial^2}{\partial y^2} \right)$ is the Laplace-Beltrami operator induced by the original metric* $\mathbf{g}$

Thus, when the metric of S is changed from $\mathbf{g}$ to $\bar{\mathbf{g}} = e^{2u}\mathbf{g}$, the Gaussian curvature k of the interior points changes to k and to $\bar{k}_{\partial S}$ for boundary points.

$$\bar{k} = e^{-2u}(k - \Delta_g u)$$

$$\bar{k}_{\partial S} = e^{-2u}(k_{\partial S} - \frac{\partial u}{\partial \mathbf{n}})$$

Here $\mathbf{n}$ is the normal to the boundary of the surface (∂S). While locally the curvatures are determined by the deforming metric, the total curvature of the surface S is determined by its topology and holds the Gauss-Bonnet theorem. Thus, the metric at each point is locally scaled according to a factor determined by the existing curvature at that point. This process is performed iteratively to evolve the metric, and consequently the curvature evolves as a heat diffusion process

$$\frac{d\mathbf{g}}{dt} = -2k\mathbf{g}$$

Definition – Uniformization theorem: Let (S, g) be a compact 2D surface with a Riemannian metric $\mathbf{g}$, then there exists a conformal metric $\bar{\mathbf{g}}$ which induces constant Gaussian curvature everywhere according to $\chi(S)$; the constant is one of {+1, 0, -1}. While there are an infinite number of conformal metrics $\bar{\mathbf{g}}$, the metric that induces constant curvature is unique.

3 Material and Methods

The material for each publication and the methods used and developed are summarised in Figure 12.
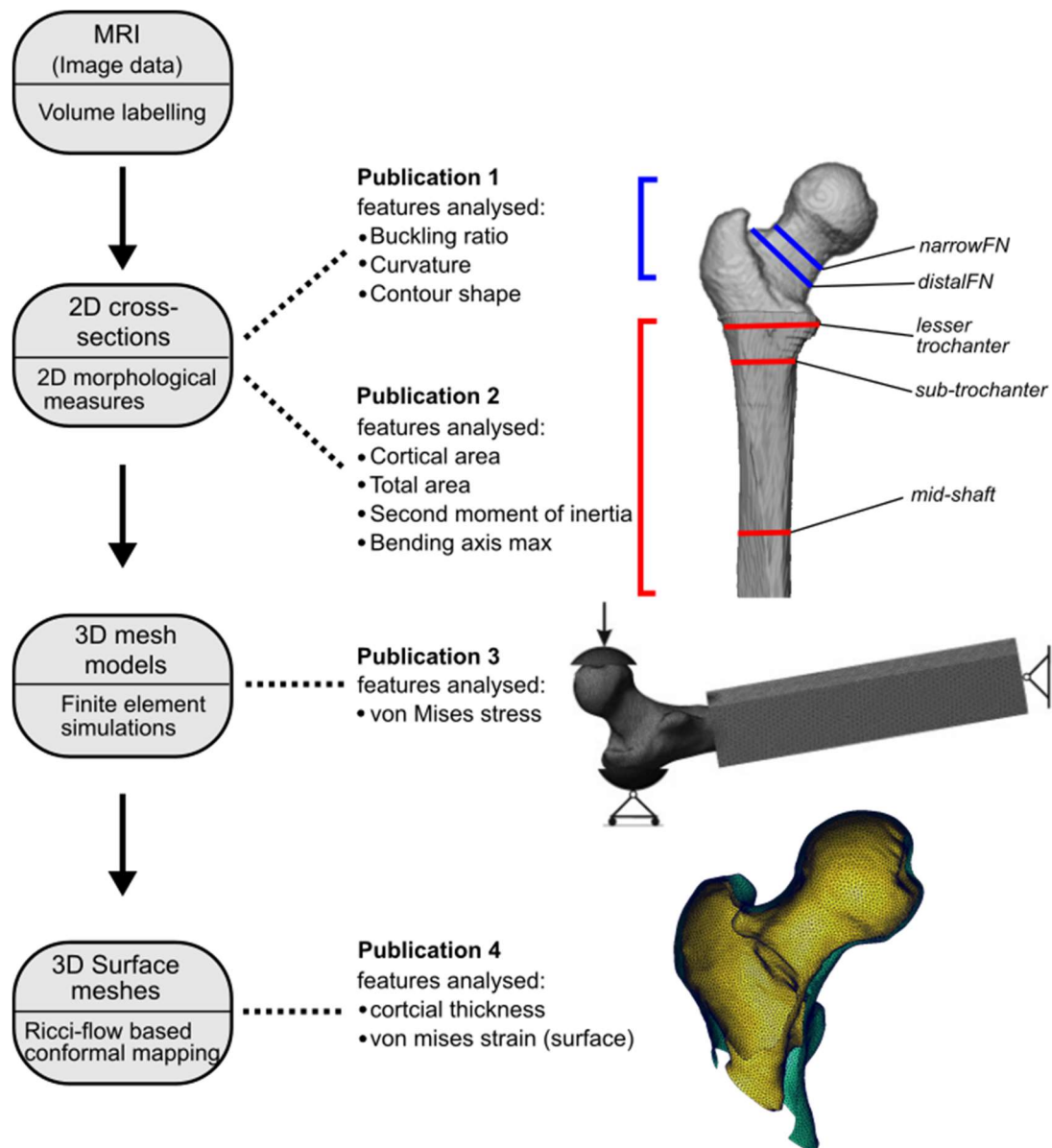
Figure 12 A summary of the material for each publication and the corresponding methods used. Features analysed as proxies for bone strength are listed for each publication.

3.1 Study material

A group of 111 subjects were chosen in order to study the geometry of their proximal femora (Table 2) (Nikander et al., 2005; Nikander et al., 2009). The study subjects consist of 91 female athletes and 20 active non-athlete females. The athletes, actively competing at the national and international level, were recruited through their respective associations and clubs. They competed in sports representing differing loading patterns: 10 high-jumpers, 9 triple-jumpers, 9 soccer players, 10 squash players, 17 power-lifters, 18 endurance runners, and 18 swimmers. Loading history was established by considering both typical sport performance as well as the typical training form. The non-athletes were age matched students recruited from nearby medical and nursing schools. The non-athletes did not practice any sport at a competitive level and were only involved in recreational physical activity two to three times a week. All the study participants were asked about potential factors affecting bone metabolism, such as medications, diseases, menstrual status, use of hormonal contraceptives, calcium intake, alcohol, tobacco, and coffee consumption, as well as their history of previous injuries and fractures. The study protocol was approved by the Ethics Committee of Pirkanmaa District Hospital, and each participant gave her written informed consent prior to the measurements.

3.1.1 Image data

All study subjects had their hip and proximal thigh anatomy (dominant leg) imaged in a Magnetic Resonance (MR) device (1.5T Avanto Syngo MR B15, Siemens, Erlangen, Germany). The tomographic image data, also called image volume, for each subject consists of a 3D stack of contiguous 2D cross-sectional images. The 3D MR image acquisition protocols were such that the anatomy of the proximal half of the femur was scanned in two separate volumes (with slight overlap): femoral head (pixel size: 0.9115 x 0.9115mm; slice thickness: 1mm) and proximal shaft (pixel size: 0.8125 x 0.8125mm; slice thickness: 3mm).

Table 2 Descriptive statistics of all 111 subjects in the study data.

	High-impact (HI)		Odd-impact (OI)		High-magnitude (HM)	Repetitive low impact (RI)	Repetitive non impact (RNI)	Non-athletic reference
	High jump	Triple jump	Football	Squash	Powerlifting	Endurance running	Swimming	Non-athletes
N	10	9	9	10	17	18	18	20
Age (years)	22 ± 4	23 ± 4	21 ± 3	29 ± 7	28 ± 6	29 ± 6	20 ± 2	24 ± 4
Height (cms)	178 ± 4	170 ± 4	162 ± 5	168 ± 9	158 ± 3	168 ± 5	173 ± 5	164 ± 5
Weight (kg)	60 ± 5	60 ± 6	58 ± 7	64 ± 9	63 ± 13	54 ± 3	65 ± 6	60 ± 7
Sport specific training (hrs/week)	11 ± 3	12 ± 2	11 ± 1	8 ± 3	9 ± 3	11 ± 3	20 ± 4	3 ± 1
Competitive career (years)	11 ± 4	10 ± 3	9 ± 3	10 ± 6	8 ± 5	12 ± 7	9 ± 3	
Bi-iliac breadth (mm)	290 ± 15	266 ± 22	263 ± 12	265 ± 15	259 ± 21	273 ± 16	282 ± 16	274 ± 12
Femoral head height (mm)	46 ± 2	43 ± 2	42 ± 1	42 ± 3	41 ± 2	43 ± 1	44 ± 2	42 ± 2
Femoral head-neck length (mm)	97 ± 3	91 ± 4	89 ± 5	92 ± 6	86 ± 4	91 ± 4	93 ± 5	91 ± 4
Isometric leg press (kg)	182 ± 44	203 ± 39	184 ± 26	195 ± 48	226 ± 39	170 ± 46	177 ± 39	145 ± 25
Dynamic strength (kg)	1712 ± 317	2277 ± 652	1643 ± 302	1634 ± 356	1730 ± 329	1436 ± 315	1617 ± 185	1450 ± 199
Counter movement jump (W/kg)	51.5 ± 6.0		43.2 ± 4.8		46.6 ± 6.8	38.3 ± 5.2	42.8 ± 4.5	36.5 ± 3.8
Figure-8 running (s)	11.3 ± 0.4		11.6 ± 0.6		12.5 ± 0.8	12.1 ± 0.5	12.0 ± 0.5	13.1 ± 0.6
Fat %	20 ± 4		25 ± 6		28 ± 7	14 ± 4	25 ± 5	32 ± 6

The femoral head volume extends from the femoral caput to the sub-trochanteric region of the shaft, with the imaging plane oriented axially to the oblique femoral neck axis. The axis was determined by the physicist through scout images. The proximal shaft volume extends distally 210-240mms from the trochanteric region, with the imaging plane oriented perpendicularly to the length of the supine subject. All image volumes were acquired in a single session with the subject maintaining pose within the MRI instrument. (Figure 13)
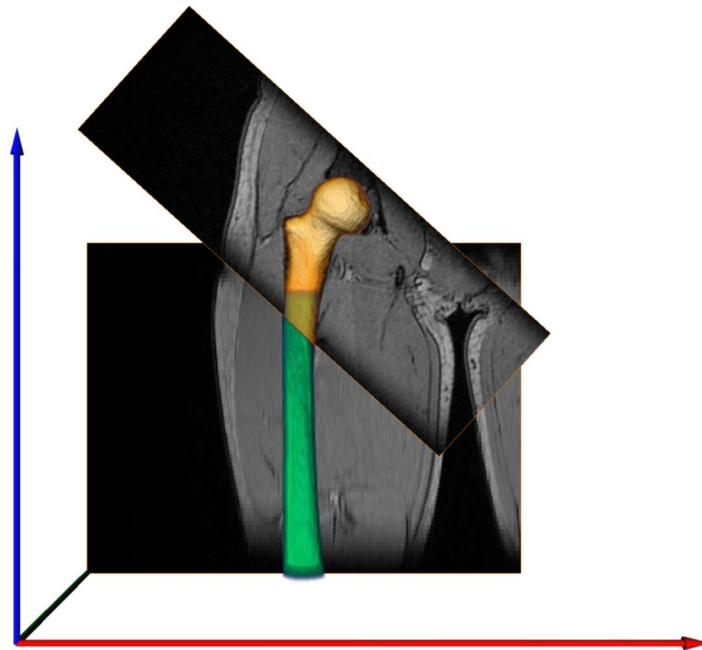
Figure 13 The grayscale images from the tomographic data of the 2 sub-volumes (femoral head and proximal shaft).The blue arrow indiactes the z direction embedded in the DICOM images. The labelled femur contained in each of the subvolumes is voxel rendered to illustrate the extent of the anatomy contained.

The cortical bone in these two anatomical sections was individually segmented from the respective image volumes. The segmentation was performed manually by labelling the bone region in the images, between periosteal and endocortical boundaries of the cortical bone, using a touch panel (Wacom Tablet Cintiq 12WX, Wacom Technology Corp., Vancouver, WA, USA) with the ITK-snap software tool (Yushkevich et al., 2006). The orientations of the segmented volumes were aligned in Avizo (VSG/FEI, Mérignac Cedex, France) by using the global coordinate system information in the DICOM files of the image datasets. Subsequently, all 111 segmented femora were made anatomically consistent by mirroring the left femur (about the sagittal plane) to mimic the right.

3.1.2 Surface meshes

The segmented bone geometries were imported into Avizo as label volumes to generate surface meshes through an inbuilt module (Hege et al., 1997). The shaft end of the volume was

left open resulting in a boundary. The resulting raw mesh contained a very high number of nodes and faces (~1,000,000 faces). The surface meshes were decimated (~50k faces) and smoothed in MeshLab (Visual Computing Lab–ISTI–CNR, http://meshlab.sourceforge.net/) through quadric error metric based surface simplification (Garland & Heckbert, 1997) and the Taubin algorithm (Taubin, 1995). Subsequently, the meshes were remeshed for isotropic vertex placement through the method implemented in Avizo (Zilske et al., 2008). This method strives to achieve meshes with triangles with equilateral sides. This produces a relatively regular sampling over the surface area. Where surfaces were required to be reconstructed from point clouds without modifying the positions, they were sampled using Poisson disk sampling (Corsini et al, 2012).

3.2 Cross-sectional analysis (2D)

Five different locations in the proximal femur were identified as anatomically significant for studying cross-sectional morphological features. These sites, along the femoral neck and the proximal diaphysis, were: narrowest femoral neck, distal femoral neck, lesser trochanter, sub-trochanter and mid-shaft (Figure12). The narrowest FN site is defined as the cross-section along the femoral neck region with the smallest cross-sectional area. DistalFN site is defined at the location corresponding to the insertion of the articulation capsule. The lesser trochanter site was defined by the maximal protrusion of the trochanteric process (i.e. tip of lesser trochanter). The corresponding cross-section was selected from the femoral head volume. Details regarding the selection procedure for these 2 sites can be found in Publication 1. The sub-trochanter cross-section was determined by tracing the location commonly used for osteometric measurements of proximal femur shaft diameter (Wescott, 2005). The location was determined by identifying a site where the medial neck-shaft junction and lesser trochanter curvature were no longer visible, while in all the subjects the locations should be within about 1-2cm below the maximum lesser trochanter transverse width. The mid-shaft site is defined in literature as the standardized cross-section observed at 50% of femur length for maximum length, physiological length or biomechanical length (Ruff and Hayes, 1983; Davies and Stock, 2014; Mongle et al., 2015). Due to the absence of the distal diaphysis in the image volume, the mid-shaft site was estimated based on projected femur lengths for each subject. Thus, the physiological femur length (Martin and Saller, 1957) was regressed from stature using its similarity to the anthropometric measurement of femur length (Montagu, 1960). It should be noted that cross-sections standardized to physiological femur length are located more proximally, compared to cross-sections standardized to maximum length and biomechanical length (Ruff and Hayes, 1983; Mongle et al., 2015). The relationship between physiological femur length and stature was based on a sample of modern Finnish females (age 18-25, N=85). The calculated half-length measurement was offset from the location of the greater trochanter to obtain the location of the appropriate cross-section. As the greater trochanter and the mid-shaft

regions are in the two separate image data volumes, it was necessary to position the two volumes in a common coordinate space. The labelled volumes were thus imported into an image processing and analysis software tool, Avizo. The 3D visualization of this composite was used in extracting the 50% location of the shaft with respect to the superior apex of the greater trochanter. Details regarding the selection procedure for the 3 sites can be found in Paper 2.

In Publication 1, the cross-sections at the 2 sites located along the femoral neck were analysed for cortical thickness, curvature and buckling ratio. These parameters were calculated along the length of the periosteal contours. The contour was sampled with respect to the polar co-ordinate angles with respect to the geometric centroid (360º = 360 points). Thus, the spatial localization along the contour of the cross-section is increased beyond the large anatomical sectors commonly used (e.g. octants: Nikander et al., 2007). In Publication 2, the parameters calculated for the 2 cross-sections in the metaphysis and the mid-shaft were bulk cross-sectional such as: cortical area, moments of inertia, bone shape ratio and theta. Four moments of inertia were calculated: i) about medio-lateral axis in the antero-posterior plane (I_x); ii) about the antero-posterior axis in the medio-lateral plane (I_y); iii) about the minimum cross-sectional diameter (I_{min}); iv) about the maximum cross-sectional diameter (I_{max}). The torsional moment (J) is derived from either of the orthogonal bending moment pairs ($I_x + I_y$ or $I_{min} + I_{max}$). Similarly, the bone shape ratio was derived from the bending moments (I_x, I_y), describing the circularity of the cross-section. The theta angle (θ) describes the orientation of the greatest bending rigidity ($\angle I_{max}, I_x$).

3.3 3D simulation (octant analysis)

The proximal femur structure of all the 111 subjects was simulated under a mechanical loading condition to mimic a lateral fall. The mesh modelling procedure started with preparation of the periosteal and endosteal surface meshes for mesh quality, which were combined into a single closed surface. Subsequently, they were converted into solid bodies in SolidWorks (Solid-Works Corp., Waltham, MA, USA). Each of the solid bodies was imported into ANSYS (AN-SYS Inc., Houston, PA, USA) for volume meshing and setting up the simulation model. The final meshed bodies consisted of 10-node tetrahedral finite elements for both materials (cortical and trabecular bone). The femoral neck region was defined in the ANSYS environment and boundary conditions were applied. After a sensitivity analysis for mesh size, a 1mm mesh element size was implemented for all individual parts of the model assembly. The cortical and trabecular bones were modelled as homogeneous isotropic, linear elastic materials. The incident loads in the simulation were setup to closely reflect the condition when a subject falls on her side and slightly towards the back. To simulate the force directions resulting from such a fall, the femoral shaft was tilted 10° with respect to the ground and the femoral neck was

internally rotated by 15°. The impact load applied in this direction was calculated by (Bouxsein et al., 2007),

$$F_{peak} = \sqrt{2gh_{cg}KM}$$

where g is the gravitational constant (9.81 m/s^2), h_{cg} is the height of the center of gravity of the body assumed as 0.51 × height (m), K is the stiffness constant (71 kN/m), and M is the effective mass calculated by (7/20 × total body mass).

The induced von Mises stresses were analysed in the femoral neck region. For each subject, this region was consistently defined to be between the head-neck junction and the inter-trochanteric line. Spatial heterogeneity of the stresses in this region of interest was achieved by dividing it into 3 sections (proximal, middle, distal) and octants within each section (superior, supero-posterior, posterior, infero-posterior, inferior, infero-anterior, anterior, supero-anterior). The octant division was performed with respect to the femoral axis which was defined as the line between the geometric centres of the femoral head and the thinnest cross-section of the neck. The procedure followed for the modelling, simulation and selection of neck region is detailed in Publication 3.

3.4 Regional surface analysis (3D)

The cortical thickness distribution over the entire proximal femur was analysed without limiting the locations to designated cross sections and predefined regions/sectors. The geometric parameters studied were cortical thickness and surface von Mises stresses. The femoral surface data was obtained from the volume mesh models constructed in Publication 3. Cortical thickness was calculated as the minimum distance from the periosteal to the endosteal surface. The stress values at the surface nodes (periosteal) of the volume mesh were extracted from the simulation results. To facilitate this analysis, a procedural chain was implemented to enable the calculation, analysis and visualization of the relevant features over the entire surface of the anatomy. Based on the surface meshes, the major tasks involved establishing correspondence between individual shape instances and statistical analysis of distributed features. In order to achieve correspondence between the shapes, the surface meshes were transformed from their 3D domain to a 2D planar domain. This transformation, called parameterization, was performed through an angle preserving conformal mapping method.

3.4.1 Surface parameterization: Ricci-flow based conformal mapping

The Ricci-flow theory for smooth surfaces was developed for discrete surfaces by Chow and Luo (2003) and a computational algorithm was introduced by Jin and colleagues (Jin et al.,

2008). The most common method for discrete representation of surfaces is through approximation by piecewise linear triangular meshes. A mesh $M(V, E, F)$, also called a simplical complex, is composed of a set of vertices V, edges E and faces F. Within these sets – the ith vertex is denoted by v_i, an edge between v_i and v_j by $e_{ij} = [v_i v_j]$ and the face formed by the ith, j^{th} and k^{th} vertices by $f_{ijk} \in [v_i v_j v_k]$.

Background geometry: Let M be a 2D simplical complex with a discrete metric. If each face of M is a triangle in the Euclidean plane, then the mesh is with Euclidean $\mathbb{E}^2$ background geometry.

The topology of the surface meshes of the femur in this study can be described as simply connected open surfaces (genus 0). The single boundary is located anatomically at the proximal section of the femoral shaft. The discrete equivalents for the characterisation of surface meshes (in $\mathbb{E}^2$) are:

  i.   Topology: determined by the connectivity of the mesh contained in the set of faces F
  ii.   Riemannian metric: edge lengths l_{ij} of edges in E
  iii. Embedding: dihedral angles at the edge e_{ij}

Discrete Riemannian metric: A discrete metric on M is a function $l : E \to \square^+$ such that on each face $f_{ijk} \in [v_i v_j v_k]$, the triangle inequality holds $l_{ij} < l_{jk} + l_{ik}$. The metric determines the corner angles at every vertex of the triangle through the cosine law

$$\theta_i = \cos^{-1} \frac{l_j^2 + l_k^2 - l_i^2}{2 l_j l_k}$$

Discrete Gaussian Curvature: Suppose M is a mesh with a discrete metric in Euclidean background geometry, $\mathbb{E}^2$. $[v_i v_j v_k]$ is a face in M and θ_i^{jk} represents the corner angle at v_i on the face. The discrete Gaussian curvature of v_i is defined as

$$K_i = \begin{cases} 2\pi - \sum_{jk} \theta_i^{jk}, & v_i \notin \partial M \\ \pi - \sum_{jk} \theta_i^{jk}, & v_i \in \partial M \end{cases}$$

Thus, the curvature at the interior vertices v_i is the difference of the sum of incident angles and the plane (2π). Curvature at the boundary vertices calculates the difference with respect to a line (π). The topology of the mesh constrains the total Gaussian curvature

$$\sum_i K_i = 2\pi \chi(M)$$

The metric is deformed in an angle preserving manner evolving to a flat metric that induces zero Gaussian curvature. The key to translating the conformal diffusion process from smooth surfaces to discrete surfaces is the circle packing metric (Thurston, 1980). Introduced by Thurston, it associates each vertex of the mesh with a circle of finite radius. The two circles on an edge between two vertices can interact in the following ways–

i. The two circles intersect each other such that the intersection angle φ_{ij} is acute (Andreev-Thurston circle packing)
ii. The two circles are disjoint (Inversive distance circle packing)

It implements the notion of the conformal deformation of the Riemannian metric by locally transforming an infinitesimal circle to an infinitesimal circle. Additionally, it preserves the intersection angles between two infinitesimal circles c_i and c_j (neighbouring on edge e_{ij}). Traditional circle packing metric requires the intersection angles between circles to be acute for a unique solution (Chow and Luo, 2003). To relax this restriction, a generalised circle packing scheme was developed (Yang et al., 2009). It guarantees the existence of a circle packing for an arbitrary triangular mesh such that the induced Euclidean metric is consistent with the circle packing metric. This in turn guarantees high conformality in parameterization.

Inversive distance: Suppose the length of edge e_{ij} between vertices v_i and v_j is l_{ij}, the radii of c_i and c_j are γ_i and γ_j respectively, then the inversive distance between c_i and c_j is given by,

$$I(c_i, c_j) = \frac{l_{ij}^2 - \gamma_i^2 - \gamma_j^2}{2\gamma_i\gamma_j}$$

Thus, a conformal deformation is effected by changing only the radii at each vertex, while preserving the inversive distance. The generalised circle packing metric is defined as,

Generalised circle packing metric: Given a mesh M and a circle packing with an associated inversive distance l_{ij} defined on every edge e_{ij}, the edge length is given by

$$l_{ij} = \sqrt{\gamma_i^2 + \gamma_j^2 + 2I_{ij}\gamma_i\gamma_j}$$

Discrete Ricci flow: Given a mesh M with a circle packing metric G and non-negative inversive distances I, the discrete Ricci flow is given by

$$\frac{du_i}{dt} = K_i - \bar{K}_i$$

where $\bar{K}_i$ is the user defined curvature at vertex v_i, and $u_i = \log\gamma_i$.

The implementation procedure for the proximal femur surfaces is detailed in a flowchart illustrated in Figure 14. In the numerical computation of the Ricci flow, the Newton method is used to improve the convergence speed. In this method, calculating the Hessian matrix is essential and is illustrated in Figure 15. The geometric interpretation of the Hessian matrix was presented by Yang et al. (Appendix, 2009).

3.4.2 Shape correspondence

After all femur surfaces are parameterised and embedded in the complex plane, their pose is rationalised by positioning the boundaries consistently in the coordinate plane. Consequently, each coordinate in the plane represents a corresponding location across the surfaces. A template mesh was created based on a randomly selected surface from the data, whose parameterised mesh was modified into a rectangle. The template mesh was then registered to all 111 parameterisations. In the resulting set of isotopological meshes, every node represents anatomically similar locations and as such the set of nodes in the mesh are treated as a dense set of landmarks. However, due to residual isotropic deformations between the native femur shapes, local improvements in matching were necessary. The details for template creation, matching and local improvements are detailed in Publication 4.

Figure 14 A flowchart summarising the procedure for the Ricci flow based registration of the proximal femur surface meshes.

Parameterize mesh to disk $M(V,E,F) \rightarrow M_{Disk}(V,E,F)$ with free boundary condition on the single boundary $\partial_1 M$

Detect feature points (FH and GT) based on the conformal factor of vertices in the disk embedded in $\mathbb{R}^2$

Introduce artificial boundary ($\partial_2 M$) in mesh M along the shortest path between feature points (calculated on M_{Disk}).

Parameterize to annulus and embed in complex plane $M(V,E,F) \rightarrow M_{Annulus}(V,E,F)$

Transform (rigid) parametric mesh embedded in complex plane $\mathbb{C}$ to align $\partial_2 M$ along the imaginary axis and scaled between $[0, 2\pi]$

2D correspondence between template mesh and all 111 parametric planes in common coordinate frame.

Algorithm 1 – Initial circle packing metric

Input: Triangular mesh M in $\mathbb{R}^3$

1. for every face $f_{ijk} = [v_i, v_j, v_k] \in M$ calculate $\gamma_i^{jk} = \frac{l_{ij} + l_{ki} - l_{jk}}{2}$

2. for every vertex $v_i \in M$ calculate radius: $\gamma_i = \min_{jk} \gamma_i^{jk}$

3. for every edge $e_{ij} = [v_i, v_j]$ calculate inversive distance: $I(v_i, v_j) = \frac{l_{ij}^2 - \gamma_i^2 - \gamma_j^2}{2\gamma_i \gamma_j}$

Algorithm 2 – Euclidean Ricci flow

Input: Triangular mesh M, target curvature $\overline{K}$, initial circle packing metric I

repeat

1. for all edges e_{ij} calculate edge length: $l_{ij} = \sqrt{\gamma_i^2 + \gamma_i^2 + 2I_{ij}\gamma_i\gamma_j}$

2. for all faces f_{ijk} calculate corner angles $\{\theta_i, \theta_j, \theta_k\}$ using $\mathbb{E}^2$ cosine laws:
$$\theta_i = \cos^{-1}\frac{l_j^2 + l_k^2 - l_i^2}{2l_j l_k}$$

3. for all faces f_{ijk}, calculate Hessian matrix entries as (Figure 15):
$$\frac{\partial \theta_i}{\partial u_j} = \frac{\partial \theta_i}{\partial u_j} = \frac{h_k}{l_k}, \quad \frac{\partial \theta_i}{\partial u_i} = -\left(\frac{\partial \theta_i}{\partial u_j} + \frac{\partial \theta_i}{\partial u_k}\right)$$

4. Solve linear system: $H\delta \mathbf{u} = \overline{K} - K$

5. Update conformal factor: $\mathbf{u} \leftarrow \mathbf{u} + \delta \mathbf{u}$

6. Calculate Gaussian curvature K_i for every v_i: $K_i = \begin{cases} 2\pi - \sum_{jk} \theta_i^{jk}, & v_i \notin \partial M \\ \pi - \sum_{jk} \theta_i^{jk}, & v_i \in \partial M \end{cases}$

until $\max_{v_i \in M} |\overline{K}_i - K_i| < \varepsilon \ (= 0.000001)$

Algorithm 3 – Embedding

1. Slice M along cut graph

2. Embed randomly selected seed face $f_{012}: [\tau(v_0), \tau(v_1), \tau(v_2)] \equiv [(0,0), (0, l_{01}), l_{02}(cos\theta_0^{12}, sin\theta_0^{12})]$

3. Put all neighbouring faces in queue
   while queue $\neq$ [] **do**

4. select first face from queue

5. find intersection of circles: $\{\tau_1(v_k), \tau_2(v_k)\} = (\tau(v_i), l_{ik}) \cap (\tau(v_j), l_{jk})$, where v_i, v_j are pre-embedded

6. $\tau(v_k)$ chosen to keep face orientation consistent

7. remove current face from queue and append new non-queued neighbouring faces
   end while

Triangle 1 {i,j,k}

Triangle 2 {i,j,m}

Hessian Matrix:

	i	j	k	m
i	$\dfrac{\partial\theta_i}{\partial u_i}$	$\dfrac{\partial\theta_i}{\partial u_j}$	$\dfrac{\partial\theta_i}{\partial u_k}$	$\dfrac{\partial\theta_i}{\partial u_m}$
j	$\dfrac{\partial\theta_j}{\partial u_i}$	$\dfrac{\partial\theta_j}{\partial u_j}$	$\dfrac{\partial\theta_j}{\partial u_k}$	$\dfrac{\partial\theta_j}{\partial u_m}$
k	$\dfrac{\partial\theta_k}{\partial u_i}$	$\dfrac{\partial\theta_k}{\partial u_j}$	$\dfrac{\partial\theta_k}{\partial u_k}$	$\dfrac{\partial\theta_k}{\partial u_m}$
m	$\dfrac{\partial\theta_m}{\partial u_i}$	$\dfrac{\partial\theta_m}{\partial u_j}$	$\dfrac{\partial\theta_m}{\partial u_k}$	$\dfrac{\partial\theta_m}{\partial u_m}$

	i	j	k	m
i	$\left(\dfrac{h_j}{l_j}+\dfrac{h_k}{l_k}\right)+\left(\dfrac{h_j}{l_j}+\dfrac{h_m}{l_m}\right)$	$-\left(\dfrac{h_k}{l_k}+\dfrac{h_m}{l_m}\right)$	$-\dfrac{h_j}{l_j}$	$-\dfrac{h_j}{l_j}$
j	$-\left(\dfrac{h_k}{l_k}+\dfrac{h_m}{l_m}\right)$	$\left(\dfrac{h_i}{l_i}+\dfrac{h_k}{l_k}\right)+\left(\dfrac{h_i}{l_i}+\dfrac{h_m}{l_m}\right)$	$-\dfrac{h_i}{l_i}$	$-\dfrac{h_i}{l_i}$
k	$-\dfrac{h_j}{l_j}$	$-\dfrac{h_i}{l_i}$	$\left(\dfrac{h_i}{l_i}+\dfrac{h_j}{l_j}\right)$	0
m	$-\dfrac{h_j}{l_j}$	$-\dfrac{h_i}{l_i}$	0	$\left(\dfrac{h_i}{l_i}+\dfrac{h_j}{l_j}\right)$

Figure 15 An illustration of the construction of the Hessian matrix from triangular meshes (here, 2 faces and 4 vertices). O_1 and O_2 are the power centres of the respective faces.

4 Results

The proximal femur morphology of the athletes was studied through distribution of different mechanically relevant features. Acting as proxies of bone strength, they are extracted either in 2 or 3 dimensions (i.e. cross-sections or volumes). The analyses included cross-sectional studies at 5 anatomical locations, 3D feature distribution and 3D finite element simulation. The general trend in the results is that the impact loading groups consistently show significantly greater feature magnitudes. However, the moderate to low impact group (endurance runners) do show significant differences in shape parameters, which is most clearly seen in the response under fall related loading simulations.

4.1 Methodological

The major methodological result is the procedural development for establishing correspondence between the proximal femur surfaces. The implemented MATLAB script accepts a stack of proximal femur surfaces and outputs the parameterisations in a common coordinate frame. The implemented script is made available at GitHub (https://github.com/NathanielNarra/Femur-RicciFlow). In its current form, it handles surfaces with a single boundary at the shaft end. It only requires the presence of epiphysis in the data, with the shaft-end boundary distal to the lesser trochanter process. The extraction of the cortical surface from the segmented image volume resulted in a genus 0 topology with one boundary. Thus, it is a simply connected open surface, where the mesh boundary is in the sub-trochanteric region of the proximal shaft. This boundary is designated as an inconsistent boundary, as it does not correspond anatomically across the subjects. The introduction of a consistent boundary along the 2 features in the dataset (FH-GT path) enabled comparison across all 111 parametric planes embedded in the complex plane. The method employed to detect each of the representative feature points, based on the conformal factor of the disk parameterization, was able to detect the features correctly in most cases. Exceptions were observed when there was pronounced concavity of the trochanteric fossa (proximal to the GT) and were handled manually. The conformal method automatically removed all scale and isometric variations between the femur instances. However, non-isometric variations were most clearly observed as differences in the relative positions of the major features in the embedded parametric plane. The correspondence between the template mesh and each parameterized subject mesh was locally tuned.

4.2 Physiological

The group-wise distribution of the unadjusted cortical thickness calculated over the 3D surface is illustrated in Figure 16. The surface on which the parameters are mapped represents the mean shape obtained from the conformal mapping based registration of the 111 surface meshes. The differences in the mean thickness at each node are calculated with respect to the control group. Details of the statistical significance of these differences and their spatial distribution can be found in publication 4.

The anatomically significant femoral neck region was studied under unphysiological loading conditions that simulate a sideways fall. The distribution of the stresses in this region was studied in two ways: volume aggregates within anatomically defined octants and surface stress distribution. Figure 17, summarising the results of Publication 3, illustrates the octants with significantly lower von Mises stresses when compared to the control group. The RI group shows the most extensive coverage of significantly lower octant stresses in all octants, except the superior octant in the distal site. The percentage differences in these octants were within the range of 12.3% - 22.6%. Significantly, in the supero-posterior and posterior regions the differences were ~20%. The HI group shows a comparatively limited span, a majority of which is consistent across the three sites. The percentage differences in these octants were within the range of 9% - 32.2%. The largest differences were observed in the inferior neck region >16.6%. The OI group exhibits varying spans across the three sites with all octants in the middle site except infero-posterior showing significance. The percentage differences in these octants were within the range of 11.5% - 17.2%. The HM group showed significance in only a couple of octants in the proximal and middle sites with no significance observed in the distal site. The percentage differences in these octants were within the range of 11.7% - 15.7%. The results of the surface mapping of the surface von Mises stresses revealed patterns over the entire proximal femur surface. Detailed graphs of statistical tests on octant stresses and illustrations of statistically significant surface regions of cortical thickness can be found in Publications 3 & 4 respectively.

The group-wise descriptive statistics of cross-sectional parameters at the 5 specific anatomical sites are presented in Table 3. The table entries are compiled from the results of Publications 1 and 2. The statistical inferences for area ratio (cortical/total) parameter are summarised in Figure 18. Results of statistical analyses for other parameters can be found in the respective publications.
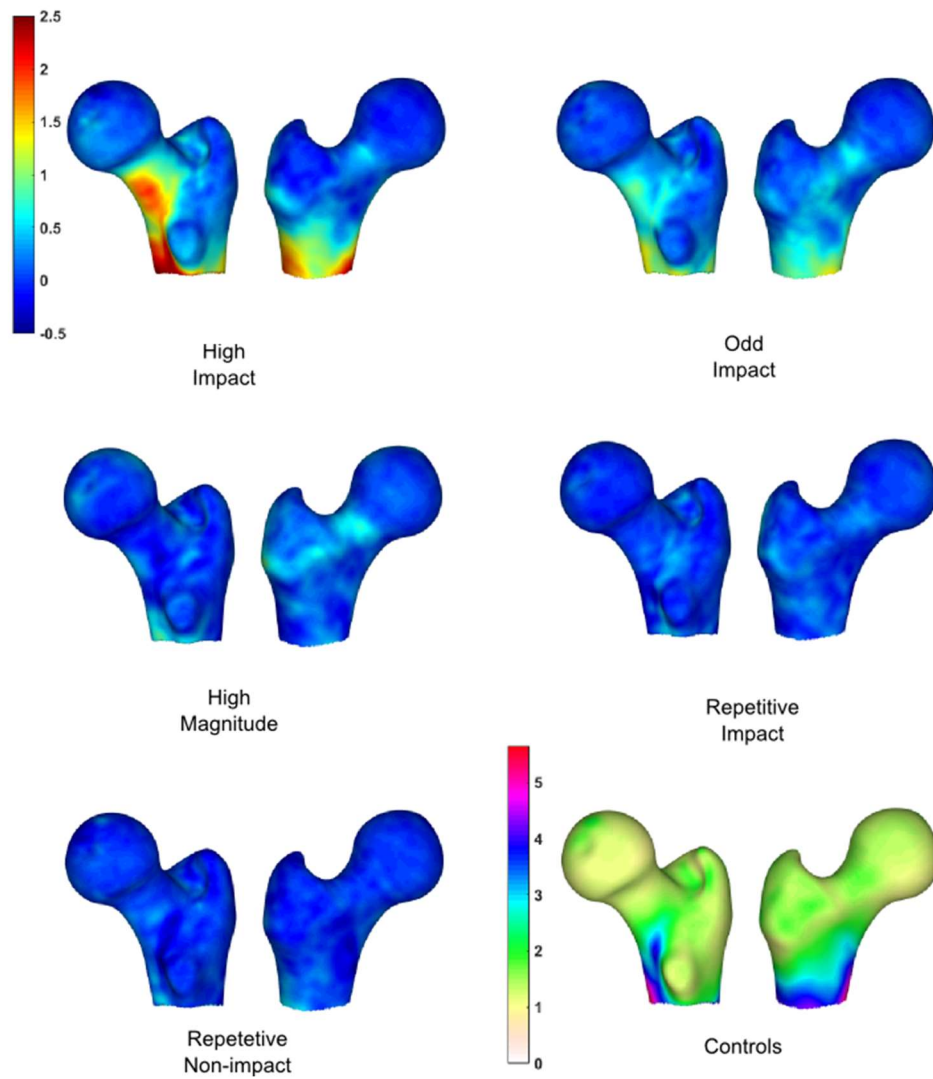
Figure 16Cortical thickness maps for every exercise loading group illustrated on the average shape of all 111 proximal femur surfaces. The displayed values for every athlete group (HI, OI, HM, RI and RNI) are the differences in the mean cortical thickness at every node from the control group. Consequently, they share the same colour-map as displayed for the High Impact group. The mean cortical thickness for the control group is displayed in a different colour-map. All values are in millimetres (mm).
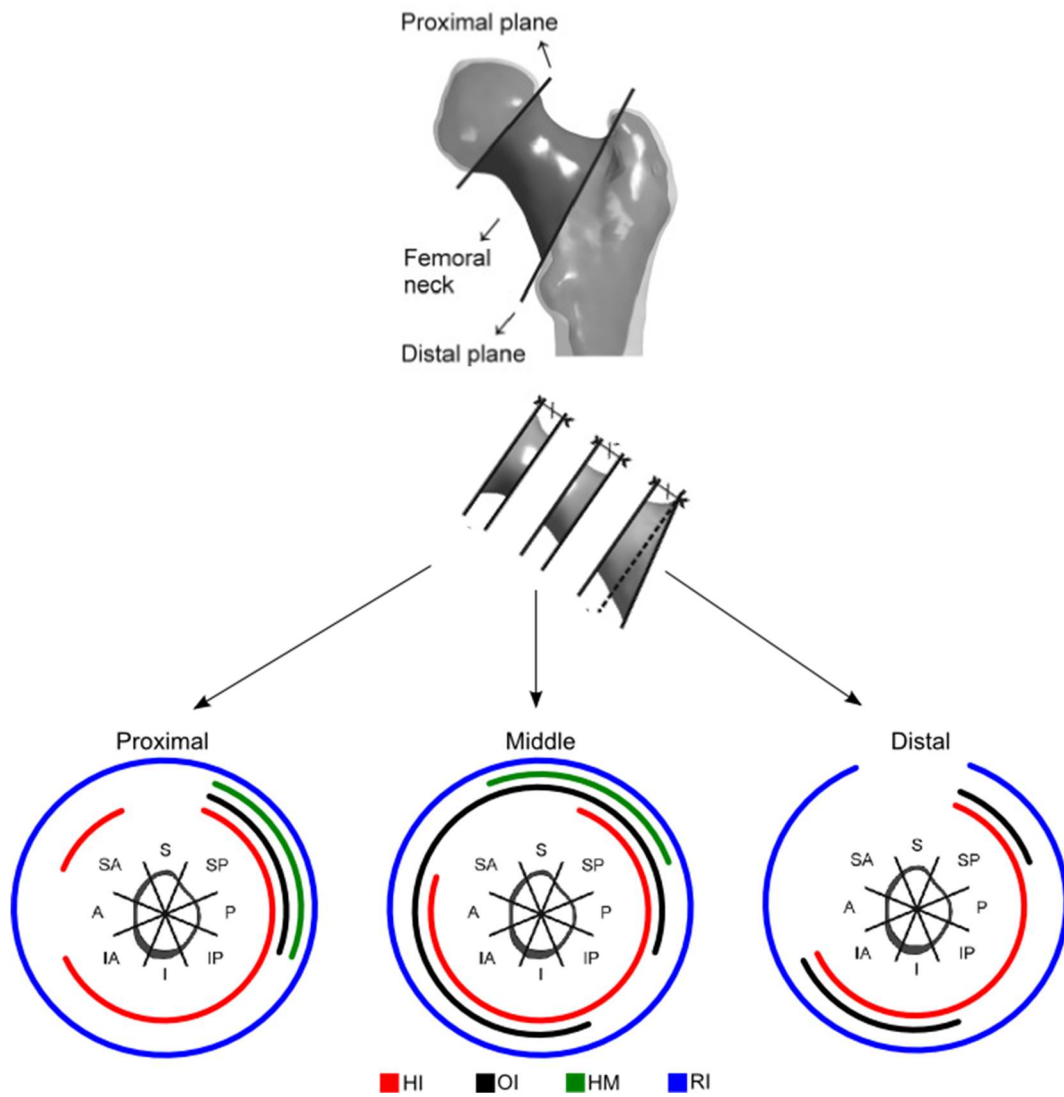
Figure 17 Illustration summarising the results of Publication, 3 showing octants with a significant reduction in induced stresses in each exercise loading group in comparison to the control group. Adapted from the results of Publication 3.

Table 3 Bulk properties at 5 anatomically significant cross-sectional locations (Area's in mm^2, J in mm^4, Theta in degrees)

|		High-impact (HI)		Odd-impact (OI)		High-magnitude (HM)	Repetitive low impact (RI)	Repetitive non-impact (RNI)	Non-athletic Controls
		High jump	Triple jump	Football	Squash	Powerlifting	Endurance running	Swimming	Non-athletes
Narrow femoral neck	Total area	696 ± 120		670 ± 95		623 ± 130	668 ± 102	709 ± 110	640 ± 103
	Cortical Area	181 ± 38		191 ± 31		159 ± 38	172 ± 38	174 ± 37	158 ± 31
	Ratio (CA/TA)	0.26 ± 0.05		0.29 ± 0.06		0.26 ± 0.05	0.26 ± 0.04	0.25 ± 0.04	0.25 ± 0.03
	Circularity	0.93 ± 0.02		0.93 ± 0.02		0.92 ± 0.02	0.94 ± 0.02	0.91 ± 0.03	0.92 ± 0.02
Distal femoral neck	Total area	720 ± 106		665 ± 101		622 ± 124	690 ± 83	731 ± 121	661 ± 95
	Cortical Area	188 ± 24		170 ± 23		138 ± 15	146 ± 17	159 ± 31	149 ± 29
	Ratio (CA/TA)	0.27 ± 0.05		0.26 ± 0.06		0.23 ± 0.03	0.21 ± 0.03	0.22 ± 0.03	0.23 ± 0.03
	Circularity	0.88 ± 0.04		0.89 ± 0.03		0.90 ± 0.03	0.88 ± 0.04	0.88 ± 0.04	0.88 ± 0.03
Lesser trochanter	Cortical area	360 ± 49	395 ± 45	341 ± 66	346 ± 47	295 ± 39	301 ± 40	301 ± 37	281 ± 42
	J	94015 ± 22039	93161 ± 9897	80978 ± 13618	90038 ± 24252	72257 ± 16642	79115 ± 17563	76665 ± 14130	68990 ± 18064
	Theta	0.5 ± 24.6	4.2 ± 23.3	4.2 ± 14.7	7.0 ± 13.9	2.4 ± 16.6	1.9 ± 16.6	2.7 ± 14.6	-2.6 ± 17.4
	Ratio	0.7 ± 0.3	0.7 ± 0.2	0.7 ± 0.1	0.7 ± 0.1	0.7 ± 0.1	0.7 ± 0.1	0.7 ± 0.1	0.7 ± 0.1
Sub-trochanter	Cortical area	384 ± 60	457 ± 43	382 ± 53	413 ± 50	356 ± 53	352 ± 41	353 ± 43	341 ± 47
	J	59657 ± 10676	57029 ± 9049	49945 ± 8625	56109 ± 15124	13551 ± 3084	14934 ± 3571	14371 ± 3041	13036 ± 2982
	Theta	-11.0 ± 44.6	7.0 ± 47.3	26.3 ± 56.1	26.4 ± 52.6	48.4 ± 28.3	41.0 ± 34.8	22.6 ± 57.1	44.4 ± 32.8
	Ratio	1.0 ± 0.2	1.0 ± 0.2	1.1 ± 0.3	1.1 ± 0.2	1.1 ± 0.2	1.1 ± 0.2	1.1 ± 0.1	1.1 ± 0.2
Mid-shaft	Cortical area	452 ± 50	486 ± 47	420 ± 49	437 ± 59	360 ± 52	380 ± 40	357 ± 38	343 ± 41
	J	57256 ± 12682	55825 ± 10207	45756 ± 9206	48515 ± 12357	33624 ± 8845	41017 ± 8416	36687 ± 6072	33537 ± 8164
	Theta	-54.1 ± 19.2	-31.3 ± 66.3	-52.0 ± 53.7	-66.9 ± 12.8	-51.1 ± 46.2	-66.7 ± 35.6	-33.9 ± 65.3	-33.9 ± 67.4
	Ratio	1.2 ± 0.3	1.3 ± 0.1	1.5 ± 0.3	1.3 ± 0.2	1.3 ± 0.2	1.5 ± 0.2	1.4 ± 0.3	1.5 ± 0.3
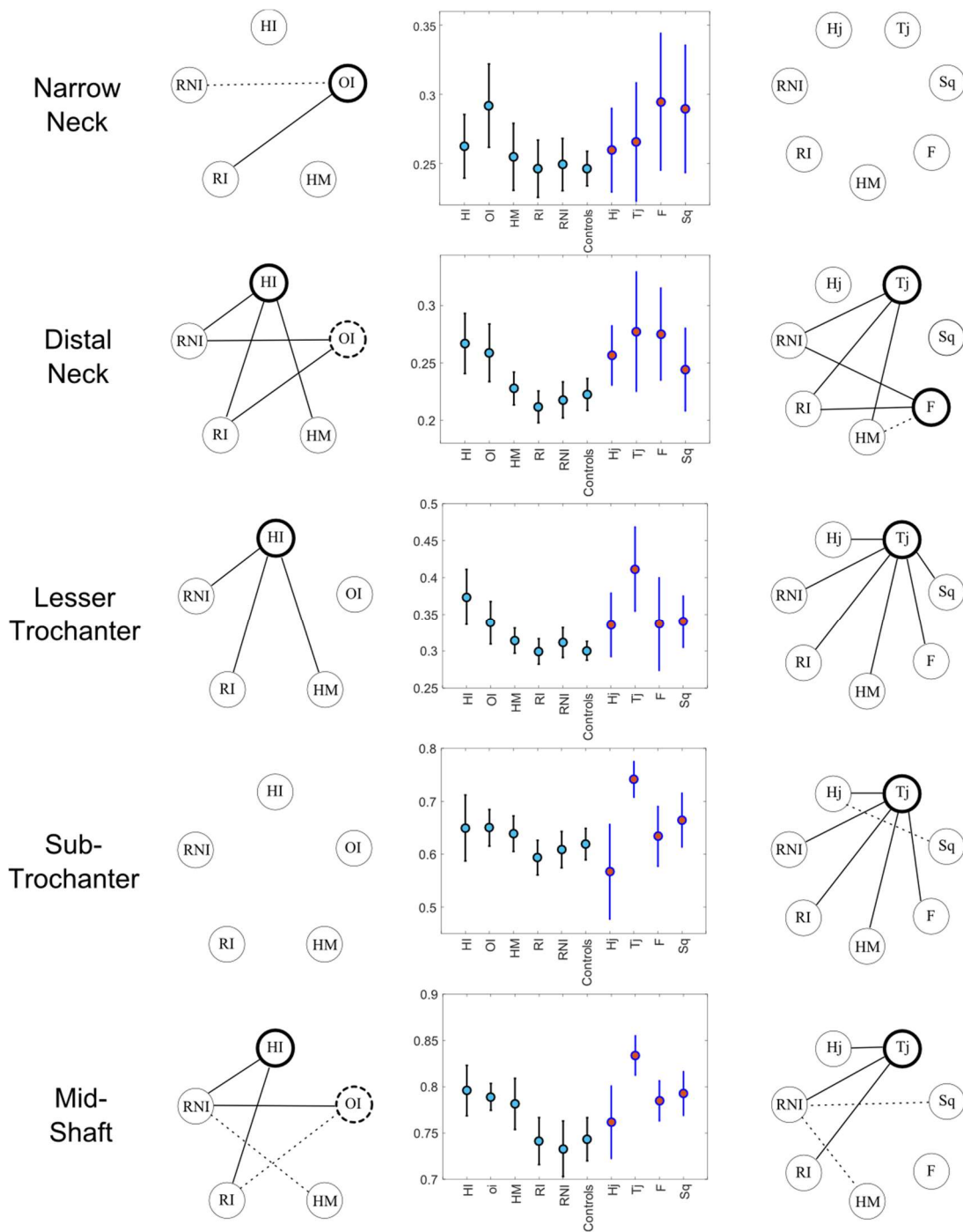
Figure 18 A summary of the statistical tests on area (cortical/total) ratios at all 5 cross-section locations studied in Publications 1 & 2. The plots show mean and 95% confidence intervals. Both loading groups (as in Publication 1) and sport groups (as in Publication 2) were analysed. Two loading groups consisted of combined sport groups: High impact: High jump (Hj) and Triple jump (Tj); Odd impact: Football (F) and Squash (Sq). The relational node graphs illustrate the result of post-hoc tests for exercise loading groups (left) and sports groups (right). Solid lines in the node-graphs indicate statistical significance ($p<0.05$) and dotted lines indicate a trend ($p<0.08$) between the groups. Bold node circles indicate significance with respect to controls ($p<0.05$) and dotted circles indicate a trend ($p<0.08$).

5   Discussion

The work compiled in this thesis seeks to develop methods to identify and localise the effects of habitual loading on proximal femur morphology. The core data upon which the hypotheses are tested and relationships explored are collected from tomographic images of professional female athletes. The sports that the young healthy female subjects are involved in represent established habitual loading patterns they are exposed to during their training and performance. The contrast is provided by age matched healthy females, who indulge in recreational exercise. Thus, the selected sports exhibit loading patterns either distinct from recreational activities (such as in high jump and triple jump), or accentuated loading characteristics (in terms of number of repetitions, intensity or duration). Studies included in this compilation have investigated the association between loading groups and morphological parameters. These parameters are biomechanically relevant features (e.g. thickness, area, buckling ratio) extracted from the data, which act as proxies for evaluating the strength of the bone. The publications can be broadly categorized as cross-sectional studies (Publications 1 & 2), FE simulation and analysis study (Publication 3) and 3D surface analysis study (Publication 4). They describe the bone at different levels of detail with the objective of increasing the spatial accuracy in the process of identifying significant focal regions in the proximal femur.

5.1   Methodological

In the quest to understand the cause and effect relationship at the proximal femur, methods strive to distinguish between study groups based on the distribution of biomechanical parameters. Classical cross-sectional parameters have served an important role in quantifying the femoral bone characteristics by identifying anatomically significant cross-sections and extracting parameters. Some, such as area moments and buckling ratio, apply mechanical engineering concepts to gauge the mechanical competence. In the proximal femur, these cross-sections are aligned in a plane perpendicular to either the shaft or femoral neck axes. In some regions of the anatomy however, defining a consistent cross-sectional plane is highly subjective, such as the inter-trochanteric region. Thus traditionally, the femoral neck and the shaft (proximal diaphysis) have been the target regions for cross-sectional analyses (Publication 2). Studies have identified fracture susceptible regions in the proximal femur (Brunner et al., 2003; Poole et al., 2017), which help focus on areas for analysis. The femoral neck especially is important as it at the greatest risk of fall related fractures (Mayhew et al., 2005; de Bakker et al., 2009; Reeve, 2017). Consequently, even cross-sectional studies have been extended where identifying spatial

heterogeneity along the 2D contour is pursued (Bailey et al., 2010). Thus, through polar representation (Publication 1) of the distribution of cross-sectional features, it becomes possible to localise the sub-regions of significance and also identify their angular spans.

With increasing data quality, the pursuit has naturally evolved towards higher resolution analyses. In such analyses, whether 2D or 3D, the foremost issue is that of anatomical correspondence. If parameters have to be compared across multiple femur instances, then it essential to ensure that the parameters are taken from similar locations. This involves mutually matching the femurs spatially, commonly referred to as registration. The popular method to study 3D morphology of the femur has been based on statistical shape (Cootes et al., 1995) and appearance (Edwards et al., 1998) models. These methods have been used extensively in understanding the major modes of shape variation between study groups. When combined with grayscales and image textures, SAM's have been used to perform segmentation from image data. Such models have been used to also extrapolate 3D geometry/morphology based on sparse data such as 2D radiographs (Zheng and Schumann, 2009; Schumann et al., 2010; Väänänen et al., 2012; Blanc et al., 2012; Lindner et al., 2013). The femur shape models are commonly trained after establishing correspondence based on landmarks introduced either manually or automatically. When not done manually, placing landmarks requires the detection of salient features and their support or through similarity measures (especially image data). The overall shape of the proximal femur is comparatively regular with a simple topology and consistent in the relative locations of most of the significant features. These similarities in shape make general registration of their pose a relatively simple task. This is in contrast to more complex and variable (inter-subject) anatomies such as the brain. However, unlike the brain which is feature rich, the femur is relatively sparse in features and thus achieving well founded anatomical correspondence can be challenging. The significant dissimilarities between femurs can exist either locally (shape variations) or globally (size of femur). The local variations can be observed as deviations between subjects in the length of the femoral neck, size of the femoral head, location of the lesser trochanter, prominence of the trochanteric processes, angulation of the neck and shaft axis.

By using Ricci flow based conformal mapping which is invariant to rigid motion, scaling, isometric and conformal deformation, the surfaces were transformed into planar (2D) domains. The method is applicable to any arbitrary topology, though this work focuses on its application to genus 0 simply connected open surface. By converting the registration domain from 3D to 2D, the problem of handling anisotropic deformations is simplified. The advantages of conformal parameterisation accorded by the Ricci flow based curvature flow method are the following (adapted from Zeng et al., 2010):

Generality: it can be implemented for arbitrary and complex topologies and produce one-to-one maps between surfaces. While topologically the femur data in this work are simple surfaces (genus 0, single boundary), the ability to produce one-to-one maps results in reliable and repeatable parameterizations.

Dimension reduction: depending on the topology of the surface, it can be used to transform it into one of 3 canonical domains ($\mathbb{R}^2, \mathbb{S}^2, \mathbb{H}^2$). Such a reduction of dimension can simplify the registration processes. As with most long bones of the body, the femur is a genus 0 surface. Thus, any femur surface can be parameterized to the Euclidean plane. Skull and vertebrae of the spinal column are examples of high genus surfaces (> 1).

Flexibility: it can used to design the final map with user defined curvatures without losing stability as long as Gauss-Bonnet theorem is satisfied. Thus, it gives flexibility to assign different target curvature schemes and can result in convenient parametrizations of the surfaces. Due to the partial extent of the femur in the surface data, topologically they are equivalent to disks. However, by introducing artificial boundaries along geodesics (e.g. inter-feature path); the resulting parameterization can be computed to suit operator convenience.

Discriminative power: conformal geometric invariants can be calculated to classify shapes. Methods calculating coordinates in the Teichmüller space have been used in the classification and registration of shapes (Zeng et al., 2010; Lam et al., 2014; Lam et al., 2015). With the femur data, by increasing the connectedness of the surfaces (i.e. increasing mesh boundaries), the conformal module (in Teichmüller space) can potentially be used for shape indexing.

Invariance: after parametrization to the canonical domains, elastic deformations that represent variations in the shape instances of the femur will be more proximal than evident in the 3D shapes. Certain anisotropic deformations such as the neck angle (if other axis lengths are kept constant) will be accounted for and the parametrization will result in a close registration. This greatly simplifies the algorithmic procedure for finding correspondence. In Publication 4, this is observed as small local variations in position of the lesser trochanter and the head-neck junction.

Robustness: importantly, Ricci flow is robust to resolution changes in the surface meshes. Thus, regardless of the triangulation (node number or connectivity), or in the presence of noise, the resulting parameterization is largely similar.

Rigor: the mathematical foundation for both the smooth (Hamilton, 1988; Chow, 1991) and discrete (Chow and Luo, 2003) Ricci flow and convexity of Ricci energy has been established.

5.2 Physiological

In Publication 1, the geometry at two significant cross-sections – at the narrowest neck and site of articular capsule attachment (distal neck) was studied. The geometry was studied as a function of the shape, buckling ratio and curvature. These parameters were used to recreate a group-wise mean cross-sectional geometry. The buckling ratio in HI group shows a significant decrease in the inferior region in both the locations. Combined with the mean periosteal contour, it is manifested as a significant increase in thickness in comparison to the controls. In the superior region of the narrow neck, an additional span of significant difference indicates an increase in the buckling ratio. This indicates that the increase in the thickness of the inferior cortex is coupled with a slight decrease in the supero-posterior thickness. The OI group also shows a significant decrease in the buckling ratio in the inferior region of the narrow neck and in the important superior region in the distal neck location. In addition, the distal neck cross-sectional shape differs significantly from the controls resulting in a more circular contour. Similarly, the RI group shows significant differences in the shape signal, resulting in a more circular shape at the narrow neck. This significant change in the shape does not seem to result in a significant improvement in the buckling ratio however. Interestingly, the buckling ratio signal in the superior region of the narrow neck reveals that most of the exercise groups have their values in the vicinity of the control group. It seems that in the superior quadrant the control subjects display a more beneficial buckling ratio though not sufficient to establish statistical significance. This trend is not observed in the distal neck location. The curvature parameter was found to be unreliable due to its sensitivity to the calculation method and the resolution of the data. The method of representing the cross-sectional parameters as distributed polar signals, aided in the localization of significances. Thus, spans of varying degrees could be identified without losing minor spans to predefined anatomical sectors (quadrants or octants). This assumes significance when considering that the proximal femur functions in a complex loading environment, which can induce regionally varying loading patterns (Aamodt et al. 1997; Kalmey & Lovejoy, 2002), where different regions within a cross-section can be under different loading regimes (tension, compression or shear).

The study presented in Publication 2 studies the athlete data from the perspective of activity reconstruction. Thus, no a priori grouping was performed on the study subjects based on perceived loading similarities of the different sports activities. Instead, every sport activity was treated as a group, thereby ungrouping the HI (triple jump and high jump) and OI (squash and soccer) groups. Three locations –trochanter, sub-trochanter and mid shaft – were identified and the associated response in cross-sectional parameters (CA, J, shape ratio and Theta) analysed. The parameter CA is a proxy for the axial

resistance of bone to tensile or compressive loads and torsional rigidity is described by J. Shape ratio describes the circularity of the cross-section and the theta angle describes the orientation of the greatest bending rigidity axis with respect to the medio-lateral axis. The parameters were additionally adjusted for size through a multi-factor size parameter vector. The results indicate a strong response in the triple jumpers. In terms of CA, they are significantly different from the powerlifters, endurance runners, swimmers and controls at all 3 locations. For J, they consistently maintain significant difference from the swimmers and controls. Interestingly, at the sub-trochanter level, the triple jumpers also exhibit a significant difference in CA from the high jumpers. When following the trends within the CA and J parameters of the HI group, the triple jumpers and high jumpers consistently exhibited a noticeable separation (in residual values). This may indicate a justification for making a distinction between extreme impact (triple jump) and high impact loading (high jump). In contrast, the OI group sports' (soccer and squash) residual values were closer to each other, indicating a possible similarity in loading patterns relevant for the studied cross-sections. The role of ground impact loading as a superior geometric adaptation stimulant was corroborated where the triple jumpers, squash and soccer players together accounted for the top response groups for CA and J at all 3 sites. Additionally, the insufficiency of swimming as a stimulus is confirmed at these 3 sites. Thus, CA and J can be viewed as relevant parameters in distinguishing between certain activities. However, shape ratio and theta angle were found to be unsuitable parameters for distinguishing between the various activities at these 3 sites.

The cross-sectional analyses in studies of Publication 1 and 2 were by design limited to designated cross-sections. The anatomical sites were manually chosen to reflect anatomical consistency across subjects. Analyses at these locations are useful for interpreting site-specific significant differences in parameters and perhaps even indicative of regional trends. Thus, regional (3D) analyses are invaluable in gathering a more complete understanding. In the study of the femoral neck region of this data, the work presented by Nikander et al. (2009) and Publication 1, was extended to evaluate the cortical bone distribution in terms of fracture risk. Publication 3 presents a comprehensive FE simulation study to analyse the behaviour of the bone under fall induced loading. The central theme was to understand if and how the various habitual loading regimes alter the simulated stress patterns in the adapted bone. Spatial resolution was defined within 3 sectors of the neck (proximal, middle and distal) and the corresponding 3D octants in each of them. The results showed a large reduction in octant stresses in the exercise groups (except RNI) in the range of ~10-30%, in the octants where statistical significance could be inferred. The RI group presented the most interesting result as it exhibited consistently lower octant stresses in nearly all octants, at all sites. In the HI group, the thicker inferior cortex results in significantly large reductions in stresses at all 3 sites in the inferior,

infero-anterior and infero-posterior octants. The HI group however, is outperformed by the OI, HM and RI group in the superior and supero-posterior octants of the middle site. Importantly, all impact exercise groups showed significantly reduced stresses in the fracture prone supero-posterior octant (Mayhew et al., 2005). Only the HM group did not return significance at the distal site, though a trend could be observed (p=0.07). Equally significantly, the superior octant at the distal site of all exercise groups was not statistically significant, with only the RI group showing a slight trend (p=0.08). In drawing parallels with the results of Publication 1, it should be noted that the middle site corresponds to the narrow neck cross-section in Publication 1. The significantly improved buckling ratio of the inferior cortex region in the HI group, and to a lesser extent OI group, coincides with the observed octants. The significant shape deviation (circular cross-section) in the RI group buttresses the claim for its robustness based on curvature, as indicated by the large reduction of octant stresses at all sites. Thus, the method of regional division of 3D point data and analysis enhances the ability to observe local effects in the femoral neck sub-anatomy. Though the analysis is based on the regional aggregation (octants) of features, it does present an incremental increase in resolution when compared to cross-sectional analyses. To further increase the spatial resolution of the analyses, a recently developed conformal mapping method was applied to the surface data (periosteal) extracted from the mesh model. In Publication 4, 3D distribution of the surface strains and cortical thickness was analysed. For each parameter, a composite was constructed to visualise results where significant response regions are labelled to indicate responsible loading groups (either unique or combinations thereof). Thus, locations apart from femoral neck and the proximal diaphysis can be studied to identify focal regions that can be used to discriminate between loading groups. By avoiding predefined anatomical sectors, the distribution patterns of significant parameters of varying spans can be identified. These patterns visualised as patches on the surface are thus not limited by the aggregating volume dimensions. Potentially the spatial resolution can be increased to match native data resolution. The method implemented shows the utility of extending FE based cohort studies in analysing simulation results. A natural extension would be studying the simulation results not merely at the surface nodes but to represent the underlying volume. Additionally, any volume feature can be aggregated towards the surface nodes and analysed through statistical parametric mapping (Carballido-Gamio et al., 2017).

5.3 Limitations

The results presented in this thesis are derived from a single base image data. The native image resolution enforces limitations on the subsequent segmentation and mesh accuracy in delineating the cortical interfaces (Sievänen et al., 2007). While in the thicker cortices this is largely mitigated, it is possible that the subtle variations in the thinner cortices (e.g. femoral head, greater trochanter) may have been averaged out. The physiological implications of the results should be inferred within the context of these limitations – of data and methods. The specific limitations of the methods employed are discussed in their respective publications. In brief, some particular ones to note are the possible errors in aligning the cross-sections within their planes. Alignment is further complicated by the fact that the loading of the femur is entirely subjective, depending on the inbuilt kinetics of the person and developed preferences in stance and gait. Thus, misalignment is an inherent source of error. Another consideration is the physical relevance of centroid referenced parameters, since they are influenced by the contour geometry. While this is a standardized practice and repeatable, perhaps calculations based on neutral axis are more relevant when considering mechanical function. It has been shown that the neutral axis does not necessarily pass through the centroid (Lieberman et al., 2004). Thus, estimating realistic neutral axes for cross-sections may help increase the physical relevance of derived parameters (Verner et al., 2016). An improvement in the reliability in the calculation of cortical thickness could be effected by implementing Laplace's equation based calculations (Jones et al., 2000). However, the actual effect on the results in this work will somewhat be balanced by the resolution limits of the data itself. In terms of correspondence, evaluating the performance of Ricci flow based conformal mapping parameterizes surfaces in the complex plane thereby accounting for all isometric deformations between the surfaces. However, certain anisotropic deformations persist, that are perceptible with respect to discernible features. In this work, only the femoral head neck junction and lesser trochanter features are used to locally perform elastic registration. The use of RBF's for this purpose was straightforward with empirically chosen parameters. This could potentially lead to residual mis-registration in regions away from these 2 features (e.g. the trochanteric fossa). Schemes to improve the alignment of the parameterized planes would further enhance the establishment of correspondence between the surfaces. The methods described in this thesis can help isolate and characterise regions that show statistically significant adaptive responses. The potential has been demonstrated with respect to cortical thickness and simulated stresses at the surface.

Conclusions

Assessing the strength of bone and its relationship to inbuilt adaptive mechanisms, in context of physical activity, requires a multimodal approach. Broadly, this can be said to involve the material and morphological aspects of strength. The analyses in this thesis have explored the morphological variations made apparent by habitual loading in the proximal femora of young women. The assumption being that the observed morphological patterns reflect specific geometric adaptation necessitated by the loading environment experienced during such activities (when contrasted with active controls). This thesis aims to provide tools and data for the systemic study and analyses of the proximal femur. Consequently, based on the results presented, and keeping the study parameters and limitations in mind, the following conclusions can be drawn:

Methodological: the results show the utility of parameters calculated at each scale in discerning between habitual loading patterns. Importantly, the results demonstrate that the classical cross-sectional bulk parameters can be insufficient in assessing robustness. This is illustrated by the lack of any significant results for bulk parameters in the endurance runners. However, their significant shape parameter hints towards the robustness evidenced in simulations under a lateral fall. In keeping with recent trends in computational anatomy, performing 3D analyses provided focal regions of significance of varying spans. Unlike current methods in computational anatomy, the central task of anatomical correspondence is achieved by treating the femur as a 2-manifold in the topological space and computing conformal maps. This culminated in the development of a novel application of Ricci flow based surface parameterisation of the 3D surfaces into 2D planar surfaces. The inherent invariance of this method to large global and local deformations can be used effectively in automating the correspondence procedure. It also shows promise in performing statistical parametric mapping of simulation results from FE studies, where the utility of the available mesh topology can be extended to multi sample analysis.

Physiological: Activities that load the proximal femur through vigorous weight bearing (or ground impacts) either at high repetitions or high loading rates, seem to show the greatest strength response. In terms of strength proxy parameters, high and extreme impact activities (HI: triple jump and high jump; OI: squash and soccer) show the largest response. When comparing moderately loading activities, the loading rate can result in distinct distributions of morphological parameters. This is demonstrated by the differences observed between the powerlifters (HM) and endurance runners (RI). While powerlifters indicated significantly increased cortical thickness in the superior neck region, the runners did not. However, under loads during a lateral fall the runners indicated a

comprehensively robust femoral neck, while in the powerlifters robustness was direction-
ally limited. In this regard, the runners seem to have even outperformed the high impact
activities. Non-impact activities (RNI: swimming) did not indicate any geometric adapta-
tion to significantly differentiate from active controls. An interesting observation is that in
certain cross-sections, there is a clear distinction between the high jumpers and triple
jumpers, both of which are high impact activities. This illustrates that impact characteris-
tics in combination with differences in the pose of the femur during load incidence can
locally alter the distribution of mechanical parameters.

References

Aamodt A, Lund-Larsen J, Eine J, Andersen E, Benum P, Husby OS. In vivo measurements show tensile axial strain in the proximal lateral aspect of the human femur. J Orthop Res. **1997** Nov;15(6):927-31.

Al Nazer R, Lanovaz J, Kawalilak C, Johnston JD, Kontulainen S. Direct in vivo strain measurements in human bone-a systematic literature review. J Biomech. **2012** Jan 3;45(1):27-40. Review

Allison SJ, Poole KE, Treece GM, Gee AH, Tonkin C, Rennie WJ, Folland JP, Summers GD, Brooke-Wavell K. The Influence of High-Impact Exercise on Cortical and Trabecular Bone Mineral Content and 3D Distribution Across the Proximal Femur in Older Men: A Randomized Controlled Unilateral Intervention. J Bone Miner Res. **2015** Sep;30(9):1709-16.

Angenent S, Haker S, Tannenbaum A, Kikinis R. On the laplace-beltrami operator and brain surface flattening. IEEE Trans. Medical Imaging. **1999** Aug; vol. 18, no. 4, pp. 700-711.

Arezoomand S, Lee WS, Rakhra KS, Beaulé PE. A 3D active model framework for segmentation of proximal femur in MR images. Int J Comput Assist Radiol Surg. **2015** Jan;10(1):55-66.

Aslan MS, Ali A, Farag AA, Arnold B, Chen D, Xiang P. 3D vertebrae segmentation in CT images with random noises. In Proceedings of the 2010 20th International Conference on Pattern Recognition, IEEE Computer Society. **2010**; p. 2290–3.

Bailey CA, Kukuljan S, Daly RM. Effects of lifetime loading history on cortical bone density and its distribution in middle-aged and older men. Bone. **2010** Sep;47(3):673-80.

Bartel DL, Davy DT, Keaveny TM. Orthopaedic biomechanics: Mechanics and design in musculoskeletal systems. New Jersey, Pearson Education. **2006**

Bassey EJ, Ramsdale SJ. Weight-bearing exercise and ground reaction forces: a 12-month randomized controlled trial of effects on bone mineral density in healthy postmenopausal women. Bone. **1995** Apr;16(4):469-76.

Beck TJ, Looker AC, Ruff CB, Sievanen H, Wahner HW. Structural trends in the aging femoral neck and proximal shaft: analysis of the Third National Health and Nutrition

Examination Survey dual-energy X-ray absorptiometry data. J Bone Miner Res. **2000** Dec;15(12):2297-304.

Beck TJ. Extending DXA beyond bone mineral density: understanding hip structure analysis. Curr Osteoporos Rep. **2007** Jun;5(2):49-55. Review

Beck TJ, Broy SB. Measurement of Hip Geometry-Technical Background. J Clin Densitom. **2015** Jul-Sep;18(3):331-7.

Blanc R, Seiler C, Székely G, Nolte LP, Reyes M. Statistical model based shape prediction from a combination of direct observations and various surrogates: application to orthopaedic research. Med Image Anal. **2012** Aug;16(6):1156-66.

Bookstein FL. In: Morphometric tools for landmark data. Cambridge University Press, Cambridge, **1991**.

Bonaretti S, Seiler C, Boichon C, Reyes M, Büchler P. Image-based vs. mesh-based statistical appearance models of the human femur: implications for finite element simulations. Med Eng Phys. **2014** Dec; 36(12): 1626-35.

Bonnick SL. HSA: beyond BMD with DXA. Bone. **2007** Jul;41(1 Suppl 1):S9-12.

Boskey AL. Mineral-matrix interactions in bone and cartilage. Clin Orthop Relat Res. **1992**; 244-274.

Bouxsein ML, Szulc P, Munoz F, Thrall E, Sornay-Rendu E, Delmas PD. Contributionof trochanteric soft tissues to fall force estimates, the factor of risk, and predictionof hip fracture risk. J. Bone Miner. Res. **2007;** 22:825–831.

Bouxsein ML, Seeman E. Quantifying the material and structural determinants of bone strength. Best Practice & Research Clinical Rheumatology. **2009**; 23:741-753.

Brown RP, Ubelaker DH, Schanfield MS. Evaluation of Purkait's triangle method for determining sexual dimorphism. J Forensic Sci. **2007** May;52(3):553-6.

Brownbill RA, Ilich JZ. Hip geometry and its role in fracture: what do we know so far? Curr Osteoporos Rep. **2003** Jun;1(1):25-31. Review

Brunner LC, Eshilian-Oates L, Kuo TY. Hip fractures in adults. Am Fam Physician. **2003** Feb 1;67(3):537-42.

Bryan R, Nair PB, Taylor M. Use of a statistical model of the whole femur in a large scale, multi-model study of femoral neck fracture risk. J Biomech. **2009** Sep 18;42(13):2171-6.

Carballido-Gamio J, Nicolella DP. Computational anatomy in the study of bone structure. Curr Osteoporos Rep. **2013** Sep;11(3):237-45. Review

Carballido-Gamio J, Bonaretti S, Kazakia GJ, Khosla S, Majumdar S, Lang TF, Burghardt AJ. Statistical Parametric Mapping of HR-pQCT Images: A Tool for Population-Based Local Comparisons of Micro-Scale Bone Features. Ann Biomed Eng. **2017** Apr;45(4):949-962.

Carballido-Gamio J, Bonaretti S, Saeed I, Harnish R, Recker R, Burghardt AJ, Keyak JH, Harris T, Khosla S, Lang TF. Automatic multi-parametric quantification of the proximal femur with quantitative computed tomography. Quant Imaging Med Surg. **2015** Aug;5(4):552-68.

Carballido-Gamio J, Harnish R, Saeed I, Streeper T, Sigurdsson S, Amin S, Atkinson EJ, Therneau TM, Siggeirsdottir K, Cheng X, Melton LJ 3rd, Keyak J, Gudnason V, Khosla S, Harris TB, Lang TF. Proximal femoral density distribution and structure in relation to age and hip fracture risk in women. J Bone Miner Res. **2013** Mar;28(3):537-46.

Castro-Mateos I, Pozo JM, Cootes TF, Wilkinson JM, Eastell R, Frangi AF. Statistical shape and appearance models in osteoporosis. Curr Osteoporos Rep. **2014** Jun;12(2):163-73. Review.

Chan DD, Neu CP. Transient and microscale deformations and strains measured under exogenous loading by noninvasive magnetic resonance. PLoS One. **2012**;7(3):e33463.

Chan DD, Cai L, Butz KD, Trippel SB, Nauman EA, Neu CP. In vivo articular cartilage deformation: noninvasive quantification of intratissue strain during joint contact in the human knee. Sci Rep. **2016**;Jan 11;6:19220.

Chow B. The Ricci flow on the 2-Sphere. Journal of Differential Geometry. **1991**; vol. 33, no. 2, pp. 325-334.

Chow B, Knopf D. The Ricci flow: An introduction. Mathematical Surveys and Monographs, AMS, Providence, RI, **2004**.

Chow B, Luo F. Combinatorial RICCI flows on surfaces. Journal of Differential Geometry. **1991**; vol. 63, no. 1, pp. 97-129.

Cole JH, van der Meulen MCH. Whole Bone Mechanics and Bone Quality. Clinical Orthopaedics and Related Research. **2011**;469(8):2139-2149.

Collins DL, Neelin P, Peters TM, Evans AC. Automatic 3D intersubject registration of MR volumetric data in standardized Talairach space. J Comput Assist Tomogr. **1994** Mar-Apr;18(2):192-205.

Comfort P, Allen M, Graham-Smith P. Comparisons of peak ground reaction force and rate of force development during variations of the power clean. J Strength Cond Res. **2011** May;25(5):1235-9.

Cootes TF, Taylor CJ, Graham J. Active shape models - their training and applications. Comput Vis Image Underst. **1995**; 61:38–59.

Corsini M, Scopigno R, Cignoni P. Efficient and flexible sampling with blue noise properties of triangular meshes. IEEE Transactions on Visualization & Computer Graphics. **2012** June; vol. 18, pp. 914-924.

Cowgill LW, Warrener A, Pontzer H, Ocobock C. Waddling and toddling: the biomechanical effects of an immature gait. Am J Phys Anthropol. **2010** Sep;143(1):52-61.

Crabtree N, Loveridge N, Parker M, Rushton N, Power J, Bell KL, Beck TJ, Reeve J. Intracapsular hip fracture and the region-specific loss of cortical bone: analysis by peripheral quantitative computed tomography. J Bone Miner Res. **2001**; 16:1318–1328.

Cristofolini L, Juszczyk M, Taddei F, Viceconti M. Strain distribution in the proximal human femoral metaphysis. Proc Inst Mech Eng H. **2009** Apr;223(3):273-88.

Currey J. Physical characteristics affecting the tensile failure properties of compact bone. J Biomech. **1990**; 24: 837-844.

Currey JD. Bones: Structure and Mechanics. Princeton, NJ: Princeton University Press. **2002**.

Currey JD. Role of collagen and other organics in the mechanical properties of bone. Osteoporos Int. **2003** Sep;14 Suppl 5:S29-36. Review

Daly RM, Rich PA, Klein R, Bass S. Effects of high-impact exercise on ultrasonic and biochemical indices of skeletal status: A prospective study in young male gymnasts. J Bone Miner Res. **1999** Jul;14(7):1222-30.

Davies RH, Twining CJ, Cootes TF, Waterton JC, Taylor CJ. A minimum description length approach to statistical shape modeling. IEEE Trans Med Imaging. **2002** May;21(5):525-37.

de Bakker PM, Manske SL, Ebacher V, Oxland TR, Cripton PA, Guy P. During sideways falls proximal femur fractures initiate in the superolateral cortex: evidence from high-speed video of simulated fractures. J Biomech. **2009** Aug 25;42(12):1917-25.

Djurić M, Milovanović P, Djonić D, Minić A, Hahn M. Morphological characteristics of the developing proximal femur: a biomechanical perspective. Srp Arh Celok Lek. **2012** Nov-Dec;140(11-12):738-45.

Dowthwaite JN, Rosenbaum PF, Scerpella TA. Site-specific advantages in skeletal geometry and strength at the proximal femur and forearm in young female gymnasts. Bone. **2012** May;50(5):1173-83.

Dowthwaite JN, Scerpella TA. Skeletal geometry and indices of bone strength in artistic gymnasts. J Musculoskelet Neuronal Interact. **2009** Oct-Dec;9(4):198-214. Review

Ebben WP, Fauth ML, Kaufmann CE, Petushek EJ. Magnitude and rate of mechanical loading of a variety of exercise modes. J Strength Cond Res. **2010** Jan;24(1):213-7.

Edwards GJ, Taylor CJ, Cootes TF. Interpreting face images using active appearance models. Proceedings Third IEEE International Conference on Automatic Face and Gesture Recognition. **1998**; p. 300-305.

Ehrlich PJ, Lanyon LE. Mechanical strain and bone cell function: a review. Osteoporos Int. **2002**; 13:688-700.

Elson RA, Aspinall GR. Measurement of hip range of flexion-extension and straight-leg raising. Clin Orthop Relat Res. **2008** Feb;466(2):281-6.

Fauth ML, Garceau L, Lutsch B, Gray A, Szalkowski C, Wurm B, Ebben, P. Kinetic analysis of lower body resistance training exercises. XXVII Congree of the International Society of Biomechanics in Sports. **2010**

Feldesman MR, Kleckner JG, Lundy JK. Femur/stature ratio and estimates of stature in mid- and late-Pleistocene fossil hominids. Am J Phys Anthropol. **1990** Nov;83(3):359-72.

Feros S. The determinants and development of fast bowling performance in cricket. **2015**:http://researchonline.federation.edu.au/vital/access/HandleResolver/1959.17/976 47

Filiault M. Digitization protocols and applications for laser scanning human bone in forensic anthropology (Thesis). **2012**. HIM 1990-2015. 1354. http://stars.library.ucf.edu/honorstheses1990-2015/1354

Friston KJ, Holmes AP, Worsley KJ, Poline J-P, Frith CD, et al. Statistical parametric maps in functional imaging: A general linear approach. Human Brain Mapping. **1994**; 2: 189–210.

Fritscher KD, Grunerbl A, Schubert R. 3D image segmentation using combined shape-intensity prior models. Int J Comp Assist Radiol Surg. **2007**; 1:341–50.

Fritz J, Duckham RL, Rantalainen T, Rosengren BE, Karlsson MK, Daly RM. Influence of a School-based Physical Activity Intervention on Cortical Bone Mass Distribution: A 7-year Intervention Study. Calcif Tissue Int. **2016** Nov;99(5):443-453.

Frome A, Huber D, Kolluri R, Bulow T, Malik J. Recognizing objects in range data using regional point descriptors. Proc. European Conf. Computer Vision. **2004**; vol. 3, pp. 224-237.

Frost HM. Bone "mass" and the "mechanostat": a proposal. Anat Rec. **1987** Sep;219(1):1-9.

Fuchs RK, Kersh ME, Carballido-Gamio J, Thompson WR, Keyak JH, Warden SJ. Physical Activity for Strengthening Fracture Prone Regions of the Proximal Femur. Curr Osteoporos Rep. **2017** Feb;15(1):43-52. Review

Fuchs RK, Bauer JJ, Snow CM. Jumping improves hip and lumbar spine bone mass in prepubescent children: a randomized controlled trial. J Bone Miner Res. **2001** Jan;16(1):148-56.

Funkhouser T, Min P, Kazhdan M, Chen J, Halderman A, Dobkin D, Jacobs D. A search engine for 3D models. ACM Trans. Graphics. **2003**; vol. 22, no. 1, pp. 83-105.

Garland M, Heckbert PS. Surface simplification using quadric error metrics. In Proceedings of SIGGRAPH. **1997** August; 97, p.209–216.

Gee AH, Treece GM, Tonkin CJ, Black DM, Poole KE. Association between femur size and a focal defect of the superior femoral neck. Bone. **2015** Dec;81:60-6.

Gower JC. Generalized procrustes analysis. Psychometrika. **1975**; 40:33–51.

Grabowski P. Physiology of Bone. Endocr Dev. **2015**;28:33-55. Review

Grassi L, Väänänen SP, Yavari SA, Jurvelin JS, Weinans H, Ristinmaa M, Zadpoor AA, Isaksson H. Full-field strain measurement during mechanical testing of the human femur at physiologically relevant strain rates. J Biomech Eng. **2014** Nov;136(11).

Grassi L, Väänänen SP, Ristinmaa M, Jurvelin JS, Isaksson H. Prediction of femoral strength using 3D finite element models reconstructed from DXA images: validation against experiments. Biomech Model Mechanobiol. **2017** Jun;16(3):989-1000.

Grassi L, Schileo E, Boichon C, Viceconti M, Taddei F. Comprehensive evaluation of PCA-based finite element modelling of the human femur. Med Eng Phys. **2014** Oct;36(10):1246-52.

Grassi L, Hraiech N, Schileo E, Ansaloni M, Rochette M, Viceconti M. Evaluation of the generality and accuracy of a new mesh morphing procedure for the human femur. Med Eng Phys. **2011** Jan;33(1):112-20.

Greene WB, Heckman JD, American Academy of Orthopaedic Surgeons. The clinical measurement of joint motion (1st ed). American Academy of Orthopaedic Surgeons, Rosemont, Ill. **1994**

Gu X, Wang Y, Chan TF, Thompson PM, Yau S-T. Genus zero surface conformal mapping and Its application to brain surface mapping. IEEE Trans. Medical Imaging. **2004** Aug; vol. 23, no. 7, pp. 949-958.

Haker S, Angenent S, Tannenbaum A, Kikinis R, Sapiro G, Halle M. Conformal surface parameterization for texture mapping. IEEE Trans. Visualization and Computer Graphics. **2000** April-June; no. 2, pp. 181-189.

Hamilton CJ, Swan VJ, Jamal SA. The effects of exercise and physical activity participation on bone mass and geometry in postmenopausal women: a systematic review of pQCT studies. Osteoporos Int. **2010** Jan;21(1):11-23. Review

Hamilton RS. The RICCI Flow on Surfaces. Math. and General Relativity. **1988**; vol. 71, pp. 237-262.

Harmon EH. The shape of the hominoid proximal femur: a geometric morphometric analysis. J Anat. **2007** Feb;210(2):170-85.

Hege H-C, Seebass M, Stalling D, Zockler M. A generalized marching cubes algorithm based on non-binary classifications. ZIB Preprint SC-97-05. **1997**

Heikkinen R, Vihriälä E, Vainionpää A, Korpelainen R, Jämsä T. Acceleration slope of exercise-induced impacts is a determinant of changes in bone density. J Biomech. **2007**;40(13):2967-74.

Heinonen A, Kannus P, Sievänen H, Oja P, Pasanen M, Rinne M, Uusi-Rasi K, Vuori I. Randomised controlled trial of effect of high-impact exercise on selected risk factors for osteoporotic fractures. Lancet. **1996** Nov 16;348(9038):1343-7.

Heinonen A, Sievänen H, Kyröläinen H, Perttunen J, Kannus P. Mineral mass, size, and estimated mechanical strength of triple jumpers' lower limb. Bone. **2001** Sep;29(3):279-85.

Hernandez CJ, Beaupre GS, Keller TS, Carter DR. The influence of bone volume fraction and ash fraction on bone strength and modulus. Bone. **2001**; 29: 74-78.

Holliday TW, Hutchinson VT, Morrow MMB, Livesay GA. Geometric morphometric analyses of hominid proximal femora: Taxonomic and phylogenetic considerations. HOMO - Journal of Comparative Human Biology. **2010**;61(1):3-15,

Huang X, Paragios N, Metaxas D. Establishing local correspondences towards compact representations of anatomical structures. Proc. Int'l Conf. Medical Image Computing and Computer-Assisted Intervention. **2003**; vol. 2, pp. 926-934.

Isaac B, Vettivel S, Prasad R, Jeyaseelan L, Chandi G. Prediction of the femoral neck-shaft angle from the length of the femoral neck. Clin Anat. **1997**;10(5):318-23.

Ito K, Minka MA 2nd, Leunig M, Werlen S, Ganz R. Femoroacetabular impingement and the cam-effect. A MRI-based quantitative anatomical study of the femoral head-neck offset. J Bone Joint Surg Br. **2001** Mar;83(2):171-6.

Jackowski SA, Kontulainen SA, Cooper DM, Lanovaz JL, Baxter-Jones AD. The timing of BMD and geometric adaptation at the proximal femur from childhood to early adulthood in males and females: a longitudinal study. J Bone Miner Res. **2011** Nov;26(11):2753-61.

Järvinen TL, Kannus P, Sievänen H. Have the DXA-based exercise studies seriously underestimated the effects of mechanical loading on bone? J Bone Miner Res. **1999** Sep;14(9):1634-5.

Jepsen KJ, Silva MJ, Vashishth D, Guo XE, van der Meulen MC. Establishing biomechanical mechanisms in mouse models: practical guidelines for systematically

evaluating phenotypic changes in the diaphyses of long bones. J Bone Miner Res. **2015** Jun;30(6):951-66.

Jin M, Kim J, Luo F, Gu X. Discrete surface Ricci flow. IEEE Trans Vis Comput Graph. **2008** Sep-Oct;14(5):1030-43.

Johannesdottir F, Aspelund T, Reeve J, Poole KE, Sigurdsson S, Harris TB, Gudnason VG, Sigurdsson G. Similarities and differences between sexes in regional loss of cortical and trabecular bone in the mid-femoral neck: the AGES-Reykjavik longitudinal study. J Bone Miner Res. **2013** Oct;28(10):2165-76.

Johannesdottir F, Turmezei T, Poole KE. Cortical bone assessed with clinical computed tomography at the proximal femur. J Bone Miner Res. **2014** Apr;29(4):771-83. Review

Johnson TP, Socrate S, Boyce MC. A viscoelastic, viscoplastic model of cortical bone valid at low and high strain rates. Acta Biomater. **2010** Oct;6(10):4073-80.

Jones SE, Buchbinder BR, Aharon I. Three-dimensional mapping of cortical thickness using Laplace's equation. Hum Brain Mapp. **2000** Sep;11(1):12-32.

Kalmey JK, Lovejoy CO. Collagen fiber orientation in the femoral necks of apes and humans: do their histological structures reflect differences in locomotor loading? Bone. **2002** Aug;31(2):327-32.

Kaptoge S, Jakes RW, Dalzell N, Wareham N, Khaw KT, Loveridge N, Beck TJ, Reeve J. Effects of physical activity on evolution of proximal femur structure in a younger elderly population. Bone. **2007** Feb;40(2):506-15.

Kaptoge S, Dalzell N, Jakes RW, Wareham N, Day NE, Khaw KT, Beck TJ, Loveridge N, Reeve J. Hip section modulus, a measure of bending resistance, is more strongly related to reported physical activity than BMD. Osteoporos Int. **2003** Nov;14(11):941-9.

Kazemi SM, Qoreishy M, Keipourfard A, Sajjadi MM, Shokraneh S. Effects of Hip Geometry on Fracture Patterns of Proximal Femur. Arch Bone Jt Surg. **2016** Jun;4(3):248-52.

Keaveny TM, Hayes WC. A 20-year perspective on the mechanical properties of trabecular bone. J Biomech Eng. **1993**; 115: 534 – 542.

Kersh ME, Pandy MG, Bui QM, Jones AC, Arns CH, Knackstedt MA, Seeman E, Zebaze RM. The heterogeneity in femoral neck structure and strength. J Bone Miner Res. **2013** May;28(5):1022-8.

Kim KM, Brown JK, Kim KJ, Choi HS, Kim HN, Rhee Y, Lim SK. Differences in femoral neck geometry associated with age and ethnicity. Osteoporos Int. **2011** Jul;22(7):2165-74.

Kipp S, Taboga P, Kram R. Ground reaction forces during steeplechase hurdling and waterjumps. Sports Biomech. **2017** Jun;16(2):152-165.

Lam KC, Gu X, Lui LM. Landmark constrained genus-one surface Teichmüller map applied to surface registration in medical imaging. Med Image Anal. **2015** Oct;25(1):45-55.

Lam KC, Gu X, Lui LM. Genus-one surface registration via teichmüller extremal mapping. Med Image Comput Comput Assist Interv. **2014**;17(Pt 3):25-32.

Lanyon LE. Functional strain in bone tissue as an objective, and controlling stimulus for adaptive bone remodelling. J Biomech. **1987**;20(11-12):1083-93. Review

Launey ME, Buehler MJ, Ritchie RO. On the mechanistic origins of toughness in bone. Annual Review of Materials Research. **2010**; 40(1): 25-53.

Lees S, Hanson D, Page E, Mook HA. Comparison of dosage-dependent effects of beta-aminopropionitrile, sodium fluoride, and hydrocortisone on selected physical properties of cortical bone. J Bone Miner Res. **1994**; 9:1377-1389.

Lektrakul N, Ratarasarn O. Geometry of proximal femur in the prediction of femoral neck fracture in the elderly female Thai population. J Med Assoc Thai. **2009** Sep;92 Suppl5:S60-6.

Levy B, Petitjean S, Ray N, Maillot J. Least squares conformal maps for automatic texture atlas generation. Proc. ACM SIGGRAPH '02. **2002**; pp. 362-371.

Li W, Kezele I, Collins DL, Zijdenbos A, Keyak J, Kornak J, Koyama A, Saeed I, Leblanc A, Harris T, Lu Y, Lang T. Voxel-based modeling and quantification of the proximal femur using inter-subject registration of quantitative CT images. Bone. **2007** Nov;41(5):888-95.

Li W, Kornak J, Harris T, Keyak J, Li C, Lu Y, Cheng X, Lang T. Identify fracture-critical regions inside the proximal femur using statistical parametric mapping. Bone. **2009** Apr;44(4):596-602.

Li W, Kornak J, Harris T, Lu Y, Cheng X, Lang T. Hip fracture risk estimation based on principal component analysis of QCT atlas: a preliminary study. SPIE Med Imaging. **2009**; 72621M.

Li W, Sode M, Saeed I, Lang T. Automated registration of hip and spine for longitudinal QCT studies: integration with 3D densitometric and structural analysis. Bone. **2006** Feb;38(2):273-9.

Lieberman DE, Polk JD, Demes B. Predicting long bone loading from cross-sectional geometry. Am J Phys Anthropol. **2004** Feb;123(2):156-71.

Lindner C, Thiagarajah S, Wilkinson JM; arcOGEN Consortium., Wallis GA, Cootes TF. Development of a fully automatic shape model matching (FASMM) system to derive statistical shape models from radiographs: application to the accurate capture and global representation of proximal femur shape. Osteoarthritis Cartilage. **2013** Oct;21(10):1537-44.

Lorenzi M, Ayache N, Frisoni GB, Pennec X; Alzheimer's Disease Neuroimaging Initiative (ADNI). LCC-Demons: a robust and accurate symmetric diffeomorphic registration algorithm. Neuroimage. **2013** Nov 1;81:470-83.

Lui LM, Wong TW, Thompson P, Chan T, Gu X, Yau ST. Shape-based diffeomorphic registration on hippocampal surfaces using Beltrami holomorphic flow. Med Image Comput Comput Assist Interv. **2010**;13(Pt 2):323-30.

Macdonald HM, Kontulainen SA, Petit MA, Beck TJ, Khan KM, McKay HA. Does a novel school-based physical activity model benefit femoral neck bone strength in pre- and early pubertal children? Osteoporos Int. **2008** Oct;19(10):1445-56.

Macintyre NJ, Lorbergs AL. Imaging-Based Methods for Non-invasive Assessment of Bone Properties Influenced by Mechanical Loading. Physiother Can. **2012** Spring;64(2):202-15.

MacKelvie KJ, Petit MA, Khan KM, Beck TJ, McKay HA. Bone mass and structure are enhanced following a 2-year randomized controlled trial of exercise in prepubertal boys. Bone. **2004** Apr;34(4):755-64.

Malladi R, Sethian JA, Vemuri BC. A fast level set based algorithm for topology independent shape modelling. J. Math. Imaging and Vision. **1996**; pp. 269-290.

Manolagas SC, Jilka RL. Bone marrow, cytokines, and bone remodeling. Emerging insights into the pathophysiology of osteoporosis. N Engl J Med. **1995**; 332:305-311.

Marshall LM, Zmuda JM, Chan BK, Barrett-Connor E, Cauley JA, Ensrud KE, Lang TF, Orwoll ES; Osteoporotic Fractures in Men (MrOS) Research Group.. Race and ethnic

variation in proximal femur structure and BMD among older men. J Bone Miner Res. **2008** Jan;23(1):121-30.

Martin R. Aging and strength of bone as a structural material. Calcif Tissue Int. **1993**; 53 (Suppl 1) S34 – S40.

Mayhew PM, Thomas CD, Clement JG, Loveridge N, Beck TJ, Bonfield W, Burgoyne CJ, Reeve J. Relation between age, femoral neck cortical stability, and hip fracture risk. Lancet. **2005** Jul 9-15;366(9480):129-35.

McLeod KJ, Rubin CT. The effect of low-frequency electrical fields on osteogenesis. J Bone Joint Surg Am. 1992 Jul;74(6):920-9. Erratum in: J Bone Joint Surg Am **1992** Sep;74(8):1274.

Miller SC, de Saint-Georges L, Bowman BM, Jee WS. Bone lining cells: structure and function. Scanning Microsc. **1989** Sep;3(3):953-60; discussion 960-1. Review

Moghaddam KK, Taheri T, Ayubian M. Bone structure investigation using X-ray and neutron radiography techniques. Appl Radiat Isot. 2008 Jan;66(1):39-43. Epub **2007** Jul 25.

Morgan E, Bouxsein M. Biomechanics of bone and age-related fractures. In the book: Principles of bone biology, Two-Volume Set, 1-2. Edited: Bilezikian J, Raisz L and Martin TJ. The Uniteted States of America, Academic Press, **2008**: pp: 29-51.

Naoki M. Thesis title: Comparative morphometric analysis of long bone ontogeny in hominoid primates. Faculty of science, University of Zurich. Retrieved from: https://doi.org/10.5167/uzh-75807. **2012**.

Neubert A, Wilson KJ, Engstrom C, Surowiec RK, Paproki A, Johnson N, Crozier S, Fripp J, Ho CP. Comparison of 3D bone models of the knee joint derived from CT and 3T MR imaging. Eur J Radiol. **2017** Aug;93:178-184.

Niinimäki S, Narra N, Härkönen L, Abe S, Nikander R, Hyttinen J, Knüsel C, Sievänen H. The relationship between loading history and proximal femoral diaphysis cross-sectional geometry. Am J Hum Biol. **2017** Jul 8;29(4).

Nikander R, Sievänen H, Heinonen A, Kannus P. Femoral neck structure in adult female athletes subjected to differentloading modalities. J. Bone Miner. Res. **2005**; 20:520–528.

Nikander R. Thesis title: Exercise loading and bone structure. Faculty of sport and health sciences, University of Jyväskylä. ISBN:978-951-39-3597-9. Retrieved from: https://jyx.jyu.fi/dspace/handle/123456789/20275 **2009**.

Nikander R, Kannus P, Dastidar P, Hannula M, Harrison L, Cervinka T, Narra NG, Aktour R, Arola T, Eskola H, Soimakallio S, Heinonen A, Hyttinen J, Sievänen H. Targeted exercises against hip fragility. Osteoporos Int. **2009** Aug;20(8):1321-8.

Nin DZ, Lam WK, Kong PW. Effect of body mass and midsole hardness on kinetic and perceptual variables during basketball landing manoeuvres. J Sports Sci. **2016**;34(8):756-65.

OpenStax College, Anatomy and Physiology. OpenStax CNX. http://cnx.org/contents/14fb4ad7-39a1-4eee-ab6e-3ef2482e3e22@8.108

Osada R, Funkhouser T, Chazelle B, Dobkin D. Shape distributions. ACM Trans. Graphics. **2002**; vol. 21, pp. 807-832.

Pennec X. Statistical computing on manifolds: from Riemannian geometry to computational anatomy. In: Emerging Trends in Visual Computing, Frank Nielsen (Ed.). Lecture notes in computer science, Springer-Verlag, Berlin. **2009**; Vol. 5416, 347-386.

Pennec X, Fillard P. Statistical computing on non-linear spaces for computational anatomy. In: Handbook of Biomedical Imaging, Springer, New York. **2015**; pp. 147-168.

Poole KE, Treece GM, Mayhew PM, Vaculík J, Dungl P, Horák M, Štěpán JJ, Gee AH. Cortical thickness mapping to identify focal osteoporosis in patients with hip fracture. PLoS One. **2012**;7(6):e38466.

Poole KE, Treece GM, Ridgway GR, Mayhew PM, Borggrefe J, Gee AH. Targeted regeneration of bone in the osteoporotic human femur. PLoS One. **2011** Jan 14;6(1):e16190.

Poole KE, Skingle L, Gee AH, Turmezei TD, Johannesdottir F, Blesic K, Rose C, Vindlacheruvu M, Donell S, Vaculik J, Dungl P, Horak M, Stepan JJ, Reeve J, Treece GM. Focal osteoporosis defects play a key role in hip fracture. Bone. **2017** Jan;94:124-134.

Puddle DL, Maulder PS. Ground reaction forces and loading rates associated with parkour and traditional drop landing techniques. J Sports Sci Med. **2013** Mar 1;12(1):122-9.

Pujol A, Rissech C, Ventura J, Badosa J, Turbón D. Ontogeny of the female femur: geometric morphometric analysis applied on current living individuals of a Spanish population. J Anat. **2014** Sep;225(3):346-57.

Pujol A, Rissech C, Ventura J, Turbón D. Ontogeny of the male femur: Geometric morphometric analysis applied to a contemporary Spanish population. Am J Phys Anthropol. **2016** Jan;159(1):146-63.

Purkait R. Triangle identified at the proximal end of femur: a new sex determinant. Forensic Sci Int. **2005** Jan 29;147(2-3):135-9.

Qian JG, Li Z, Zhang H, Bian R, Zhang S. Effectiveness of Selected Fitness Exercises on Stress of Femoral Neck using Musculoskeletal Dynamics Simulations and Finite Element Model. J Hum Kinet. **2014** Jul 8;41:59-70.

Reeve J. Role of cortical bone in hip fracture. Bonekey Rep. **2017** Jan 13;6:867. Review

Rein TR, Harvati K. Geometric morphometrics and virtual anthropology: advances in human evolutionary studies. Anthropol Anz. **2014**;71(1-2):41-55.

Rho JY, Kuhn-Spearing L, Zioupos P. Mechanical properties and the hierarchical structure of bone. Med Eng Phys. **1998**; 20(2):92-102.

Richtsmeier JT, DeLeon VB, Lele SR. The promise of geometric morphometrics. Am J Phys Anthropol. **2002**;Suppl 35:63-91. Review

Rubin C, Turner AS, Mallinckrodt C, Jerome C, McLeod K, Bain S. Mechanical strain, induced noninvasively in the high-frequency domain, is anabolic to cancellous bone, but not cortical bone. Bone. **2002** Mar;30(3):445-52.

Rubin CT, McLeod KJ. Promotion of bony ingrowth by frequency-specific, low-amplitude mechanical strain. Clin Orthop Relat Res. **1994** Jan;(298):165-74.

Rudman KE, Aspden RM, Meakin JR. Compression or tension? The stress distribution in the proximal femur. Biomed Eng Online. **2006** Feb 20;5:12.

Ruiz-Correa S, Shapiro L, Meila M. A new paradigm for recognizing 3D object shapes from range data. Proc. IEEE Int'l Conf. Computer Vision. **2003**; vol. 2, pp. 1126-1133.

Ruff CB, Larsen CS. Long bone structural analyses and the reconstruction of past mobility: A historical review. In Reconstructing Mobility: Environmental, Behavioral, and Morphological Determinants, Springer. **2014**; pp. 13-29.

Sartoris DJ, Resnick D. Innovative approaches to noninvasive bone densitometry. Crit Rev Diagn Imaging. **1990**;30(1):19-39. Review

Scerpella TA, Bernardoni B, Wang S, Rathouz PJ, Li Q, Dowthwaite JN. Site-specific, adult bone benefits attributed to loading during youth: A preliminary longitudinal analysis. Bone. **2016** Apr;85:148-59.

Schumann S, Tannast M, Nolte LP, Zheng G. Validation of statistical shape model based reconstruction of the proximal femur--A morphology study. Med Eng Phys. **2010** Jul;32(6):638-44.

Sharon E, Mumford D. 2D-shape analysis using conformal mapping. Proc. IEEE Conf. Computer Vision and Pattern Recognition. **2004**; pp. 350-357.

Sievänen H. Hormonal influences on the muscle-bone feedback system: a perspective. J Musculoskelet Neuronal Interact. **2005** Jul-Sep;5(3):255-61. Review

Sievänen H, Karstila T, Apuli P, Kannus P. Magnetic resonance imaging of the femoral neck cortex. Acta Radiol. **2007** Apr;48(3):308-14.

Skedros JG, Mason MW, Bloebaum RD. Modeling and remodeling in a developing artiodactyl calcaneus: a model for evaluating Frost's Mechanostat hypothesis and its corollaries. Anat Rec. **2001** Jun 1;263(2):167-85.

Skedros JG, Baucom SL. Mathematical analysis of trabecular 'trajectories' in apparent trajectorial structures: the unfortunate historical emphasis on the human proximal femur. J Theor Biol. **2007** Jan 7;244(1):15-45.

Slizewski A, Semal P. Experiences with low and high cost 3D surface scanner. Quartär Yearbook for Ice Age and Stone Age Research. **2009**; 56:131-138.

Stacoff A, Diezi C, Luder G, Stüssi E, Kramers-de Quervain IA. Ground reaction forces on stairs: effects of stair inclination and age. Gait Posture. **2005** Jan;21(1):24-38.

Styner MA, Rajamani KT, Nolte LP, Zsemlye G, Székely G, Taylor CJ, Davies RH. Evaluation of 3D correspondence methods for model building. Inf Process Med Imaging. **2003** Jul;18:63-75.

Styner M, Oguz I, Xu S, Brechbühler C, Pantazis D, Levitt JJ, Shenton ME, Gerig G. Framework for the statistical shape analysis of brain structures using SPHARM-PDM. In: Proceedings of insight journal-ISC/NA-MIC workshop on open science at MICCAI 2006, Copenhagen, Denmark. **2006**.

78

Sun Y, Abidi M. Surface matching by 3D point's fingerprint. Proc. IEEE Int'l Conf. Computer Vision. **2001**; vol. 2, pp. 263-269.

Tang ZH, Yeoh CS, Tan GM. Radiographic study of the proximal femur morphology of elderly patients with femoral neck fractures: is there a difference among ethnic groups? Singapore Med J. **2016** Aug 29.

Taubin G. A signal processing approach to fair surface design. In Proceedings of SIGGRAPH 97. **1995**; p. 351-358.

Terzopoulos D, Witkin A, Kass M. Constraints on deformable models: recovering 3D shape and nonrigid motion. Artificial Intelligence. **1988**; vol. 35, pp. 91-123.

Thompson WR, Scott A, Loghmani MT, Ward SR, Warden SJ. Understanding Mechanobiology: Physical Therapists as a Force in Mechanotherapy and Musculoskeletal Regenerative Rehabilitation. Phys Ther. **2016** Apr;96(4):560-9.

Thompson WR, Rubin CT, Rubin J. Mechanical regulation of signaling pathways in bone. Gene. **2012** Jul 25;503(2):179-93. Review

Thurston WP. Geometry and topology of three-manifolds. Lecture notes at Princeton university. **1980**.

Tolly B, Chumanov E, Brooks A. Ground reaction forces and osteogenic index of the sport of cyclocross. J Sports Sci. **2014**;32(14):1365-73.

Travison TG, Beck TJ, Esche GR, Araujo AB, McKinlay JB. Age trends in proximal femur geometry in men: variation by race and ethnicity. Osteoporos Int. **2008** Mar;19(3):277-87.

Treece GM, Gee AH, Mayhew PM, Poole KE. High resolution cortical bone thickness measurement from clinical CT data. Med Image Anal. **2010** Jun;14(3):276-90.

Treece GM, Gee AH. Independent measurement of femoral cortical thickness and cortical bone density using clinical CT. Med Image Anal. **2015** Feb;20(1):249-64.

Turner CH, Robling AG. Designing exercise regimens to increase bone strength. Exerc Sport Sci Rev. **2003** Jan;31(1):45-50. Review

Turner CH, Robling AG. Mechanisms by which exercise improves bone strength. J Bone Miner Metab. **2005**;23 Suppl:16-22. Review

Väänänen SP, Grassi L, Flivik G, Jurvelin JS, Isaksson H. Generation of 3D shape, density, cortical thickness and finite element mesh of proximal femur from a DXA image. Med Image Anal. **2015** Aug;24(1):125-34.

Väänänen SP, Jurvelin JS, Isaksson H. Estimation of 3D shape, internal density and mechanics of proximal femur by combining bone mineral density images with shape and density templates. Biomech Model Mechanobiol. **2012** Jul;11(6):791-800.

Vainionpää A, Korpelainen R, Vihriälä E, Rinta-Paavola A, Leppäluoto J, Jämsä T. Intensity of exercise is associated with bone density change in premenopausal women. Osteoporos Int. **2006**;17(3):455-63.

van den Bogert AJ, Read L, Nigg BM. An analysis of hip joint loading during walking, running, and skiing. Med Sci Sports Exerc. **1999** Jan;31(1):131-42.

Vemuri B, Mitiche A, Aggarwal J. Curvature-based representation of objects from range data. Image and Vision Computing. **1986**; vol. 4, pp. 107-114.

Vercauteren T, Pennec X, Perchant A, Ayache N. Diffeomorphic demons: efficient non-parametric image registration. Neuroimage. **2009** Mar;45(1 Suppl):S61-72.

Verim Ö, Taşgetiren S, Er MS, Timur M, Yuran AF. Anatomical comparison and evaluation of human proximal femurs modeling via different devices and FEM analysis. Int J Med Robot. **2013** Jun;9(2):e19-24.

Verner KA, Lehner M, Lamas LP, Main RP. Experimental tests of planar strain theory for predicting bone cross-sectional longitudinal and shear strains. J Exp Biol. **2016** Oct 1;219(Pt 19):3082-3090.

Wang H, Frame J, Ozimek E, Leib D, Dugan EL. Influence of fatigue and load carriage on mechanical loading during walking. Mil Med. **2012** Feb;177(2):152-6.

Wang J, Shi C. Automatic construction of statistical shape models using deformable simplex meshes with vector field convolution energy. Biomed Eng Online. **2017** Apr 24;16(1):49.

Wang S, Wang Y, Jin M, Gu XD, Samaras D. Conformal geometry and its applications on 3D shape matching recognition and stitching. IEEE Trans. Pattern Analysis and Machine Intelligence. **2007** July; vol. 29, no. 7, pp. 1209-1220.

Wang Y, Gupta M, Zhang S, Wang S, Gu X, Samaras D, Huang P. High resolution tracking of non-rigid 3D motion of densely sampled data using harmonic maps. Proc. IEEE Int'l Conf. Computer Vision. **2005a**; vol. 1, pp. 388-395.

Wang Y, Chiang MC, Thompson PM. Mutual information-based 3D surface matching with applications to face recognition and brain mapping. Proc. IEEE Int'l Conf. Computer Vision. **2005b**; vol. 1, pp. 527-534.

Weeks BK, Beck BR. The BPAQ: a bone-specific physical activity assessment instrument. Osteoporos Int. **2008** Nov;19(11):1567-77.

Weeks BK, Young CM, Beck BR. Eight months of regular in-school jumping improves indices of bone strength in adolescent boys and Girls: the POWER PE study. J Bone Miner Res. **2008** Jul;23(7):1002-11.

White S. Virtual archaeology - the NextEngine desktop laser scanner. Archaeology International. **2015**; 18, pp.41–44.

Whitmarsh T, Humbert L, De Craene M, Del Rio Barquero LM, Frangi AF. Reconstructing the 3D shape and bone mineral density distribution of the proximal femur from dual-energy X-ray absorptiometry. IEEE Trans Med Imaging. **2011** Dec;30(12):2101-14.

Worsley K, Taylor J, Carbonell F, Chung M, Duerden E, et al. SurfStat: A Matlab toolbox for the statistical analysis of univariate and multivariate surface and volumetric data using linear mixed effects models and random field theory. NeuroImage Organization for Human Brain Mapping Annual Meeting **2009**; 47: S102.

Yang Y-L, Guo R, Luo F, Hu S-M, Gu X. Generalized Discrete Ricci Flow. Computer Graphics Forum. **2009**; 28: 2005–2014.

Yang L, Burton AC, Bradburn M, Nielson CM, Orwoll ES, Eastell R; Osteoporotic Fractures in Men (MrOS) Study Group.. Distribution of bone density in the proximal femur and its association with hip fracture risk in older men: the osteoporotic fractures in men (MrOS) study. J Bone Miner Res. **2012** Nov;27(11):2314-24.

Yeo BT, Sabuncu MR, Vercauteren T, Ayache N, Fischl B, Golland P. Spherical demons: fast diffeomorphic landmark-free surface registration. IEEE Trans Med Imaging. **2010** Mar;29(3):650-68.

Zeng W, Zeng Y, Wang Y, Gu X, Samaras D. Non-rigid surface matching and registration based on holomorphic differentials. Proc. European Conf. Computer Vision, **2008**.

Zeng W, Samaras D, Gu X. Ricci flow for 3D shape analysis. IEEE Transactions on Pattern Analysis and Machine Intelligence. **2010**; 32(4): 662-677.

Zeng W, Gu XD. Ricci flow for shape analysis and surface registration: theories, algorithms and applications, Springer Briefs in Mathematics, Springer, New York. **2013**; xii+139 pp., ISBN 978-1-4614-8781-4

Zhang D, Hebert M. Harmonic maps and their applications in surface matching. Proc. IEEE Conf. Computer Vision and Pattern Recognition. **1999**; pp. 524-530.

Zheng G, Schumann S. 3D reconstruction of a patient-specific surface model of the proximal femur from calibrated x-ray radiographs: a validation study. Med Phys. **2009** Apr;36(4):1155-66.

Zilske M, Lamecker H, Zachow S. Adaptive remeshing of non-manifold surfaces. Eurographics 2008 Annex to the Conf. Proc. **2008**; pp. 207-211.

ORIGINAL PAPERS

1

FEMORAL NECK CROSS-SECTIONAL GEOMETRY AND EXER-CISE LOADING

by

Narra N, Nikander R, Viik J, Hyttinen J & Sievänen H, Jul 2013

Femoral neck cross-sectional geometry and exercise loading

Nathaniel Narra[1,2], Riku Nikander[3], Jari Viik[1,2], Jari Hyttinen[1,2] and Harri Sievänen[4]

[1]*Department of Biomedical Engineering, Tampere University of Technology,* [2]*BioMediTech, Institute of Biosciences and Medical Technology,* [3]*Department of Welfare and Human Functioning, Helsinki Metropolia University of Applied Sciences,Helsinki, and* [4]*Bone Research Group, UKK Institute for Health Promotion Research, Tampere, Finland*

Summary

Correspondence

Nathaniel Narra, Department of Biomedical Engineering, Tampere University of Technology, Finn-Medi 1 L 4, Biokatu 6, FI − 33520, Tampere, Finland

E-mail: nathaniel.narragirish@tut.fi

The aim of this study was to examine the association between different types of exercise loading and femoral neck cross-sectional geometry. Our data comprised proximal femur magnetic resonance (MR) images obtained from 91 female athletes and their 20 age-matched controls. The athletes were categorized according to typical training activity − high impact (high and triple jumping), odd impact (racket and soccer playing), high magnitude (power lifting), repetitive low impact (endurance running) and repetitive non-impact (swimming). Segmented MR images at two locations, narrowest cross-section of the femoral neck (narrowFN) and the cross-section at insertion of articular capsule (distalFN), were investigated to detect between group differences in shape, curvature and buckling ratio derived using image and signal analysis tools. The narrowFN results indicated that the high-impact group had weaker antero-superior (33% larger buckling ratio than controls) but stronger inferior weight-bearing region (32% smaller than controls), while the odd-impact group had stronger superior, posterior and anterior region (21% smaller buckling ratio than controls). The distalFN results indicated that the high-impact group had stronger inferior region (37% smaller buckling ratio), but the odd-impact group had stronger superior region (22% smaller buckling ratio) than the controls. Overall, the results point towards odd-impact exercise loading, with inherently varying directions of impact, associated with more robust cross-sectional geometry along the femoral neck. In conclusion, our one-dimensional polar treatment for geometrical traits and intuitive presentation of differences in trends between exercise groups and controls provides a basis for analysis with high angular accuracy.

Introduction

Bone adapts to habitual loading. In his seminal work, Frost discussed the relationship between externally applied load and bone strengthening by postulating the Mechanostat theory (Frost, 1987). Over the years, our understanding of this crucial process of various stress features and consequent bone adaptation has increased greatly (Duncan, 1995; Turner, 1998; Turner & Pavalko, 1998; Robling *et al.*, 2006; Klein-Nulend & Bakker, 2008). Concepts of structural mechanics from engineering have been successfully applied to hypothesize and explain the phenomena related to bone adaptation. Galileo's work in developing flexural theory along with later formulization by Euler-Bernoulli is some of the earliest studies in this field. Recently, Mayhew *et al.*(2005) stated that changes in the

geometrical structure of femoral neck, independent of osteoporosis, contribute significantly to bone fragility. By employing the beam theory, they contended that with normal ageing, the loss of bending resistance is minimal, while the risk of local buckling in the thinned cortices, particularly at the superior region, increases manifold. This finding implies that purely geometric parameters of the bone, such as asymmetry, and their structural-mechanical implications have a significant bearing on femoral neck integrity.

The effect of exercise in countering the influence of natural ageing or endocrine changes on bone loss and deterioration of bone structure is well established (Nikander *et al.*, 2010b). Recently, the association of different exercise-loading conditions with cortical thickness in the femoral neck cross-section (Nikander *et al.*, 2009) and diaphyseal geometry of the

weight-bearing tibia (Nikander *et al.*, 2010a) have been investigated. These studies, among others (Bass *et al.*, 2002; Daly & Bass, 2006), illustrate that specific exercise loading can modulate the spatial distribution of cortical bone within the bone cross-section.

Computed tomography (CT) and magnetic resonance (MR) imaging, in various scales from macro to micro, are common methods to assess different bone structural traits (Kazakia & Majumdar, 2006; Manske *et al.*, 2010; Griffith & Genant, 2011). Image processing and analysis, in turn, play an integral role in these assessments. Model-based image analysis procedures have been applied to study various anatomies as they are particularly suited for handling the natural variation in shape and structure (Barratt *et al.*, 2008; Heimann & Meinzer, 2009; van de Giessen *et al.*, 2010). Further, statistical models can be used in representing a distribution of features in a compact form and consequently used to observe any prevalent patterns across categorized groups.

In this study, we investigated the cortical bone distribution at two locations of the femoral neck cross-section by extracting geometric parameters that have apparent biomechanical bearing in terms of bone fragility, by combining various image analysis tools and measures. Our goal was to present a novel way to analyse bone cross-sections and the association between specific exercise loading and the actual femoral neck cross-sectional geometry using low resolution proximal femur MR images from various groups of athletes. In particular, we analysed the periosteal shape, cortical bone curvature and buckling ratio of the femoral neck to reveal any distinct differences between the exercise-loading groups and their controls.

Material and methods

Participants

This study material consisted of proximal femur MR images of 91 female athletes and their 20 controls obtained from our previous study (Nikander *et al.*, 2009). The athletes were recruited through their respective associations and clubs. The age-matched controls were students and were recruited from nearby medical and nursing schools. The controls did not practice any sport at competitive level and were mostly involved in recreational physical activity two to three times a week. All the participants of the study were inquired of potential factors affecting bone metabolism such as medications, diseases, menstrual status, use of hormonal contraceptives, calcium intake, alcohol, tobacco and coffee consumption, as well as their history of previous injuries and fractures. The study protocol was approved by the Ethics Committee of Pirkanmaa Hospital District, and each participant gave their written informed consent prior to the measurements.

The athletes were nine triple jumpers, ten high jumpers, nine soccer players, ten squash players, 17 powerlifters, 18 endurance runners and 18 swimmers. According to the classi-

fication scheme proposed recently by Nikander *et al.* (2005; Nikander *et al.*, 2006), these sports were broken down into five different exercise-loading types: high-impact; odd-impact; high-magnitude; repetitive, low-impact and repetitive, non-impact loading. The high-impact group comprised the triple jumpers and high jumpers; the odd-impact group the soccer and squash players; the high-magnitude group the powerlifters; the repetitive, low-impact group the endurance runners; and the repetitive, non-impact group the swimmers.

The proximal femur cortical geometry, covering the whole proximal femur from the femoral caput to the subtrochanteric level of the femoral diaphysis, was imaged with a 1·5-T MRI system (Siemens, Avanto Syngo MR B15, Erlangen, Germany). Two haste localization series were used as scout images to specify the correct orientation of the imaging plane such that the plane of the femoral neck cross-sections was perpendicular to the oblique femoral neck axis. The used imaging sequence was a standardized axial T1-weighted gradient echo volumetric interpolated breath-hold (VIBE) examination [Field of view 35×26, TR 15·3 ms, TE 3·32 ms, slice thickness 1 mm without gaps, echo train length=1, flip angle=10°, matrix 384×288, the in-plane resolution (pixel size) 0·9 mm×0·9 mm].

Data extraction

The data used in this study consisted of segmented MR image slices scanned at two anatomical locations along the femoral neck. The first location corresponded to the insertion of the articulation capsule at the femoral neck, hence referred to as 'distalFN'. The second location was the narrowest femoral neck cross-section from the data volume for each subject, hence referred to as the 'narrowFN' (Fig. 1).

For the segmentation of cortical bone at distalFN and narrowFN sites, we first used manual procedures supplied by ITK-snap.(Yushkevich *et al.*, 2006) All procedures for performing analysis on the segmented data were then implemented in MATLAB. For the distalFN location, three slices per subject were segmented, and their average taken. For the narrowFN location, the region including the smallest femoral neck cross-section was first located visually by choosing 5 adjacent slices for the segmentation. The bone area of each five slices was calculated to determine the smallest cross-section. The two adjacent slices in addition to the smallest cross-section were used to calculate the mean thinnest femoral neck slice for that subject. Of note, the continuity of the cortical wall was guaranteed by forcing a minimum of one pixel representing the cortex over the endosteal layer. This was necessary as the in-plane resolution of the MR images was not sufficient to detect the actual (sub-pixel level) cortical thickness at some parts of the femoral neck cross-section.

As the next step, the information in the segmented two-dimensional cross-sections was transformed into one-dimensional shape signal, which presented the cortical thickness and periosteal shape as a function of angle around the given
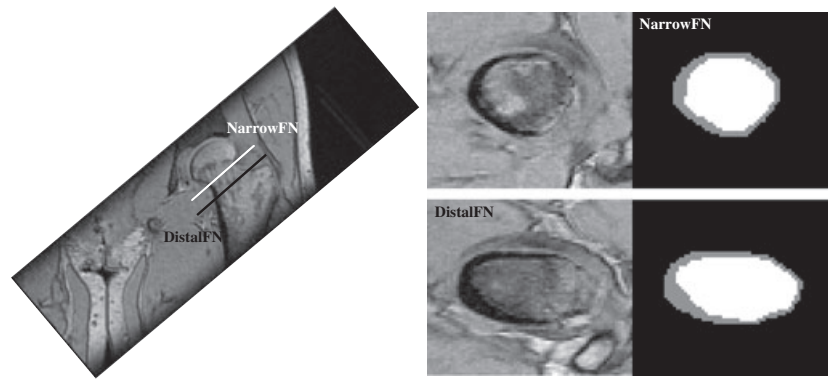
Figure 1 Coronal scout image of the proximal femur showing the two locations under study – the narrowest femoral neck cross-section (narrowFN) and the site of insertion of the articular capsule at the femoral neck (distalFN). The corresponding axial cross-sectional images and their segmentations are also presented.

cross-section. Presenting the shape information as a curve provides a new perspective to observing differences in geometric traits along the periosteal boundary. The curve was generated by calculating the centroid of the cross-section and tracing the polar coordinates of the periosteal cortical boundary with respect to it (see Fig. 2).

Before further analysis, inconsistencies in image orientation caused by potential between subject differences in lower limb rotation and consequent femoral anteversion during imaging were corrected. Specifically, the tip of the lesser trochanter from the segmented bone volume was used as an anatomical landmark to obtain the angle it makes with respect to the centroid. Using this angle, the signals for each subject were aligned accordingly to provide appropriately aligned curves and anatomically consistent results.

Data analysis

To properly analyse the femoral neck geometry across subjects, the shape signals were normalized by removing all scale information. A common approach to centre and scale the image shape is to normalize the concatenated list of coordinates (s) of the 2D shape points (perimeter), so that $|s|$ corresponds to unity. For each subject, the scaling was performed

by setting the square root of the sum of the squared distances of each perimeter point from the mean, to unity.

For the calculation of buckling ratio, the absolute cortical thickness was first calculated by determining the distance between the segmented periosteal and endosteal boundary along radial lines starting from the centroid of the cross-section around the periosteal envelope. Then, the buckling ratio was calculated as a ratio of the periosteal radius to cortical thickness at every point along the periosteum.

For estimating the curvature of the femoral neck cross-section, a contour representing the midline between the segmented periosteum, and the endosteum was first determined. Subsequently, the curvature at every point on this contour was calculated based on an angular span of 30 degrees centred at the point in consideration. Using quadratic polynomial fitting for the coordinates in this span, the curvature through its second derivative was calculated as follows

$$K = \frac{|x\prime y\prime\prime - y\prime x\prime\prime|}{(x\prime^2 + y\prime^2)^{\frac{3}{2}}}$$

where x and y are parametric representation of the planar curve in Cartesian coordinates. For reference, the above curvature formula for a straight line reduces to zero, while for a
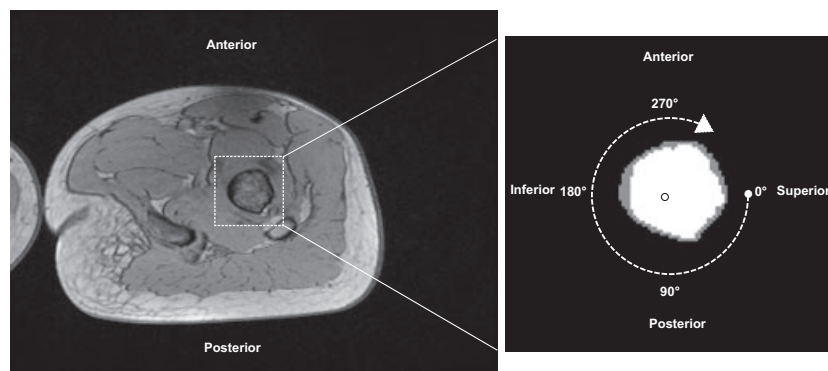

Figure 2 Segmentation of the MR image of femoral neck cross-section into two regions – cortical and trabecular. The dot in trabecular region indicates the position of the centroid. The clockwise arrow indicates direction of travel for generating the shape signal along the periosteal boundary.

circle of radius R, it reduces to 1/R. Of note, we treated the curvature here as a local property defined at a point on the peripheral curve dependant only on its neighbours within a span of 30 degrees. We experimented with a range of span angles between 10 and 60 degrees and considered 30 as adequate for the data at hand. It is a compromise between gaining a smooth curvature signal and keeping the span size modest.

The above described three-one-dimensional signals – shape, buckling ratio and curvature – determined for each subject were used for the comparisons of cortical geometry between the exercise-loading groups.

In addition, a simple measure of circularity of the whole cross-section at both locations was calculated for each subject as follows

$$C = \frac{4\pi A}{P^2}$$

where A is the area of cross-section, and P is the perimeter.

To get the mean representations of shape, buckling ratio and curvature for each exercise-loading group, the dimensions of these signals were first reduced by principal component analysis (PCA). The number of eigen-modes deemed to sufficiently represent the data was based on the criteria that they accounted for 95% of the variation in the given signal. For all athletic groups, the number of modes mostly varied between 6 and 10, whereas for the control group, consistently, fewer modes were required reflecting a more compact distribution in geometric traits. These PCA modes were then used to reconstruct the individual signals, which in turn were used to determine the mean model for each exercise-loading group.

The mean group signals were examined as themselves as well converted back to 2D contours. In the 2D contoured form, the endosteal and periosteal contours were plotted to reflect the normalized shape and cortical thickness information based on the buckling ratio.

Statistical analysis

All exercise groups were compared with the control group. To illustrate potential between group differences in 1D shape signals and 2D contours, we used the simple unpaired t-test (95% confidence interval). A level of significance of $P \leq 0.05$ was chosen with no assumptions of equal variances as per the Behrens–Fisher problem. For all signals, the test was performed for every point over the entire angular span, from 0 to 359 degrees, and those indicating difference were plotted on the signals and contours.

Results

Table 1 shows the basic cross-sectional geometric characteristics of the study groups at the two locations. As expected, the narrowFN site, across groups, returns a higher circularity measure than the distalFN site. Within a site, groups tend to be indistinct in trends with the exception of repetitive, low-impact group showing a slightly greater value at the narrow-FN site. In the ratios of cortical to total area, at the distalFN site, the high- and odd-impact groups show higher values. While at the narrowFN site, only the odd-impact group has a distinctly higher ratio. It should be noted, however, that these higher values are accompanied with a greater spread, reflected by the slightly larger standard deviation values.

At the narrowFN location (see Fig. 3 and Fig. 4), differences compared with the control data were observed in the high-and odd-impact groups. In the high-impact group, there were two distinct sectors: the antero-superior sector with a span of 77 degrees showed an average 33% increase in buckling ratio (indicating more susceptibility to buckling failure) and the inferior sector with a span of 98 degrees showed an average 32% decrease in buckling ratio (indicating less susceptibility to buckling failure). The odd-impact group showed a wide 149 degree sector with an average 21% decrease in buckling ratio (indicating less susceptibility to buckling

Table 1 Geometric traits (mean (SD)) at the narrow neck and distal neck locations in different exercise-loading groups.

| Femoral neck location	High impact	Odd impact	High magnitude	Repetitive, low impact	Repetitive, non-impact	Non-athletic Reference
distalFN						
Total area (ToA) (mm^2)	720 (106)	665 (101)	622 (124)	690 (83)	731 (121)	661 (95)
Cortical area (CoA) (mm^2)	188 (24)	170 (23)	138 (15)	146 (17)	159 (31)	149 (29)
Ratio (CoA/ToA)	0·27 (0·05)	0·26 (0·06)	0·23 (0·03)	0·21 (0·03)	0·22 (0·03)	0·23 (0·03)
Circularity	0·88 (0·04)	0·89 (0·03)	0·90 (0·03)	0·88 (0·04)	0·88 (0·04)	0·88 (0·03)
narrowFN						
Total area (ToA) (mm^2)	696 (120)	670 (95)	623 (130)	668 (102)	709 (110)	640 (103)
Cortical area (CoA) (mm^2)	181 (38)	191 (31)	159 (38)	172 (38)	174 (37)	158 (31)
Ratio (CoA/ToA)	0·26 (0·05)	0·29 (0·06)	0·26 (0·05)	0·26 (0·04)	0·25 (0·04)	0·25 (0·03)
Circularity	0·93 (0·02)	0·93 (0·02)	0·92 (0·02)	0·94 (0·02)	0·91 (0·03)	0·92 (0·02)
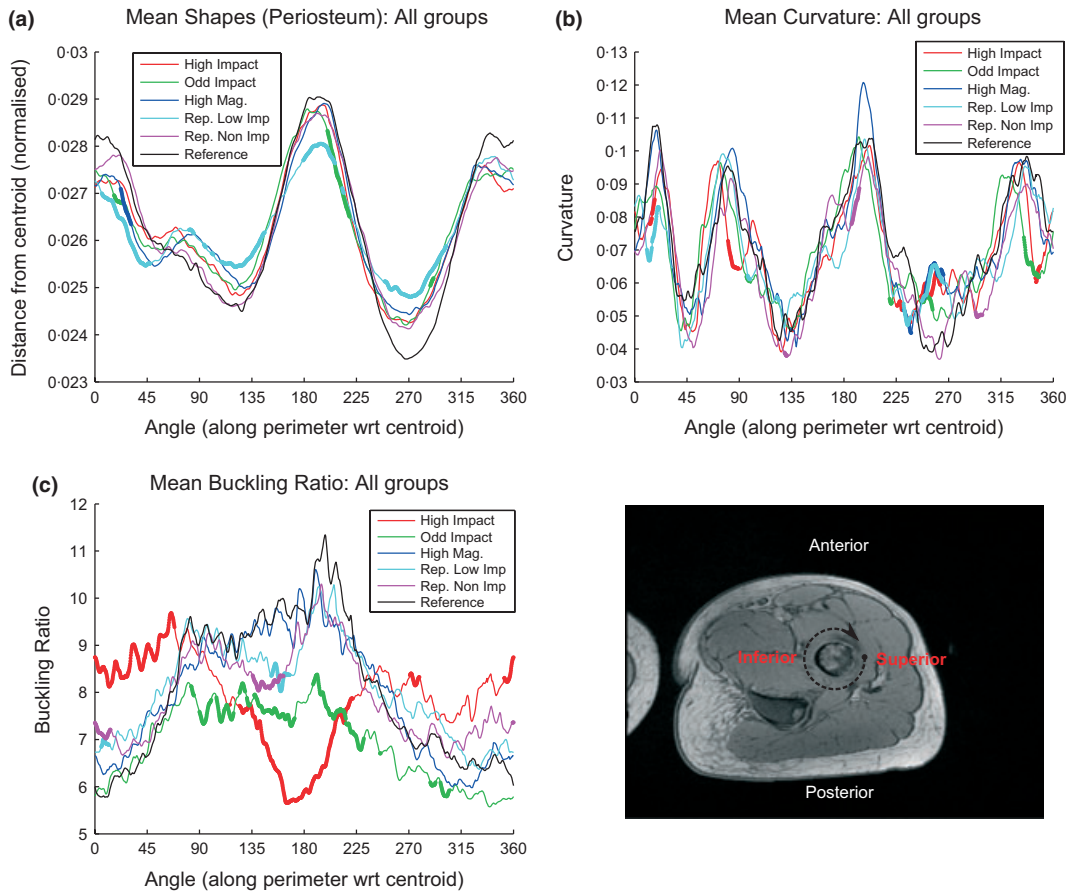
Figure 3 Shape signal of the periosteal contour (a) curvature of the cortical bone (b) and buckling ratio (c) at the narrow femoral neck location. Bold lines indicate group differences as suggested by the simple t-test. Angle: 0 − superior, 90 − posterior, 180 − inferior, 270 − anterior.
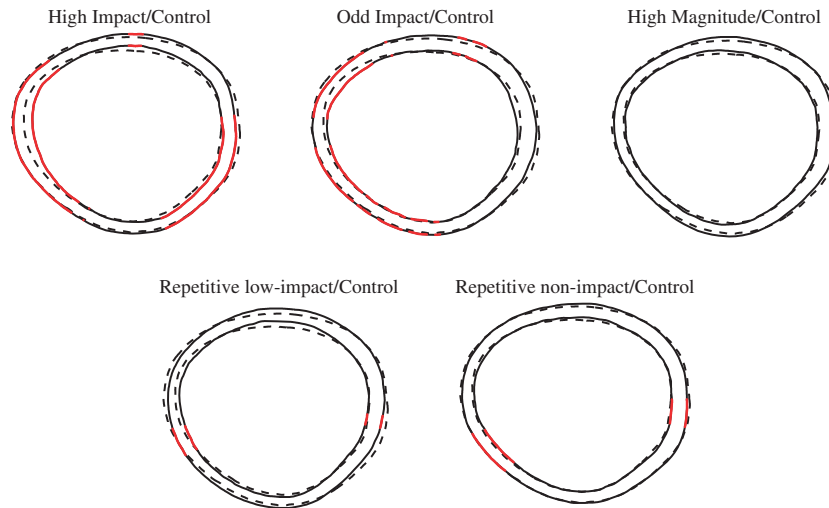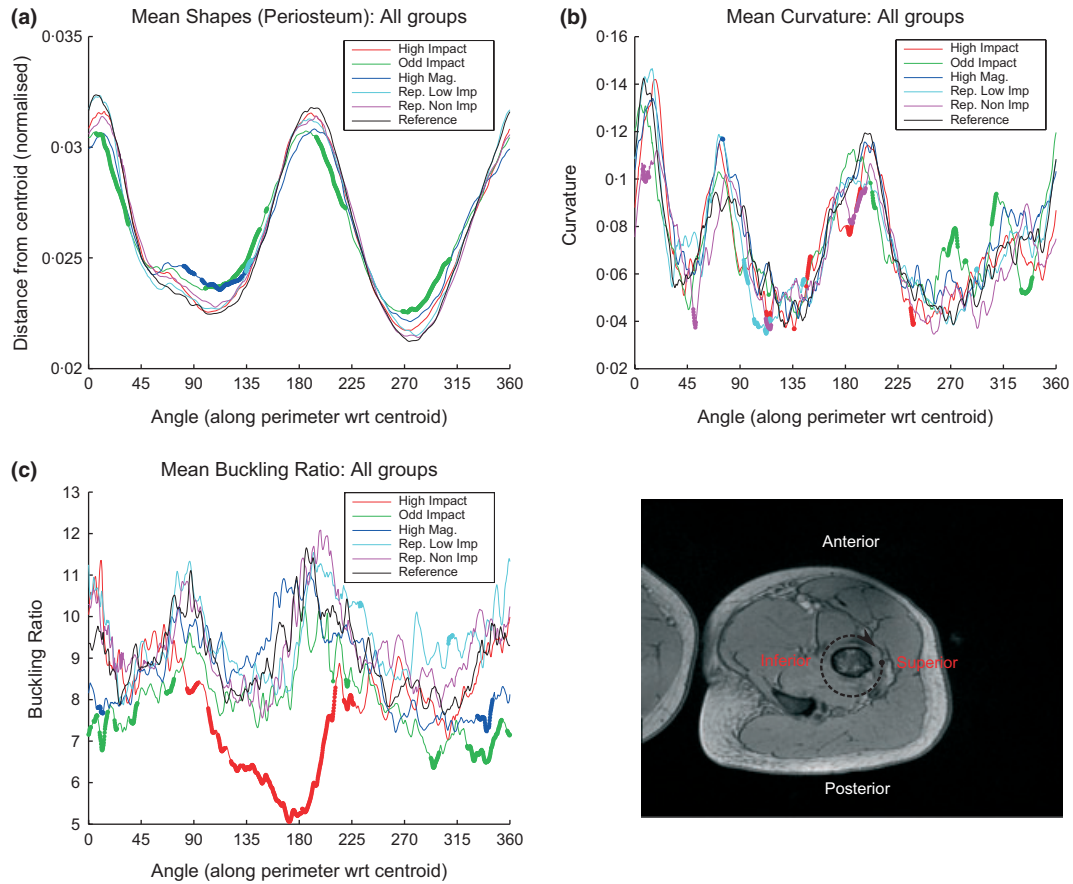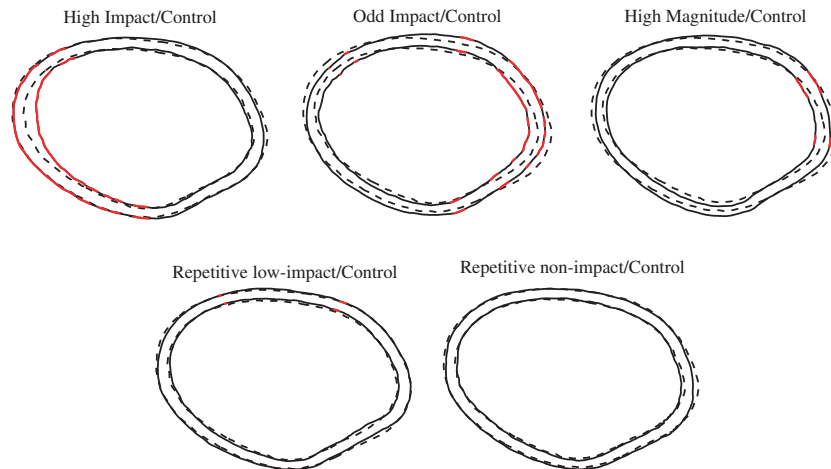

Figure 4 Reconstructed mean outer and inner cortical contours in the exercise-loading groups at the narrowest femoral neck location. For reference, contours as obtained from the control group are drawn in dashed line. Red plots indicate locations where the difference in buckling ratio differed from the control values.

failure). Concerning the shape of the outer cortical surface, the repetitive, low-impact loading indicated a more circular shape. In the other exercise groups, no consistent patterns in shape traits were observed.

At the distal femoral neck (see Fig. 5 and Fig. 6), differences compared with the control data were again observed only in the high-and odd-impact groups. The high-impact group showed an average 37% decrease in the buckling ratio

(a) Mean Shapes (Periosteum): All groups

(b) Mean Curvature: All groups

(c) Mean Buckling Ratio: All groups

Figure 5 Shape signal of the periosteal contour (a) curvature of the cortical bone (b) and buckling ratio (c) at the distal femoral neck location. Bold lines indicate group differences as suggested by the simple t-test. Angle: 0 − superior, 90 − posterior, 180 − inferior, 270 − anterior.

High Impact/Control   Odd Impact/Control   High Magnitude/Control

Repetitive low-impact/Control   Repetitive non-impact/Control

Figure 6 Reconstructed mean outer and inner cortical contours in the exercise-loading groups at the distal femoral neck location. For reference, contours as obtained from the control group are drawn in dashed line. Red plots indicate locations where the difference in buckling ratio differed from the control values.

in the inferior region over a span of 79 degrees, and the odd-impact group showed an average 22% decrease in the buckling ratio in the superior region over a span of approximately 61 degrees. This mostly results from a more circular shape of the distal femoral neck of the odd-impact group.

Similar to the results at the narrow femoral neck, the shape and curvature signals indicated marginal differences. The odd-impact group tended to show a more circular shape, as reflected by the somewhat lower amplitude of the shape signal.

Discussion

In the present paper, we showed new information about the association of exercise loading with shape, curvature and buckling ratio at two biomechanically relevant cross-sections at the femoral neck (narrowest neck and insertion of the articular capsule). We paid particular attention to a rigorous treatment in the extraction and sound analysis of these geometrical traits by employing statistical models of the individual exercise-loading groups based on principal component analysis of the cortical geometry derived from segmented MR images. Instead of limiting the analysis to predetermined wide anatomical sectors (e.g. quadrants or octants (Mayhew *et al.*, 2005; Nikander *et al.*, 2009; Johannesdottir *et al.*, 2011)), we achieved a higher degree of angular accuracy through the polar presentation of the three geometrical traits – shape, buckling ratio and cortical curvature. These parameters, and the differences between exercise categories and controls, were determined for every periosteal surface point and presented both as 1D shape signals and reconstructed 2D cross-sections. It is stressed that the main purpose of this study was to illustrate the influence of specific exercise loading on femoral neck geometry and reveal consistent patterns using novel ways to present and generate relevant information.

Obviously, the present detailed analysis confirmed our previous observations (Nikander *et al.*, 2009) but now with a higher specificity particularly illustrating the exact anatomic directions where the exercise-loading groups showed differences in these geometrical traits compared with the control group. Of all groups, the high-impact group showed clearly the thickest cortical bone at the inferior weight-bearing region at both the distal and the narrowest neck locations. Biomechanically, a strong cortical bone is necessary given the extreme ground reaction forces (up to 20 times of body weight on a single leg), and a triple jumper may experience during an athletic performance (Heinonen *et al.*, 2001). In contrast, the odd-impact group showed a relatively thicker cortical bone throughout the femoral neck in quite a consistent fashion and slightly more circular bone at the distal femoral neck. Also, the repetitive, low impact represented by endurance runners seemed to have a more circular cross-section at the narrow femoral neck. The latter findings are relevant in terms of secular and clinical perspective. It was recently found that the people living in mediaeval times, apparently loading their proximal femora in a more varying ways than nowadays, had more circular femoral neck cross-sections (Sievänen *et al.*, 2007). A more circular bone, particularly with relatively thicker cortical bone in all directions, is more robust in all loading circumstances than a mechanically more specialized bone. When assessing the quality of bone through its quantitative measurement (as obtained from clinical Dual-energy X-ray absorptiometry scanning), it should be noted that bone geometry has a direct influence on areal bone mineral density (BMD) values. Areal BMD depends not only on the bone mineral apparent density but also on cross-sectional size of given bone (Sievänen, 2000). Thus, subjects with larger, high-density cortical bone (lower buckling ratio) and/or larger bone cross-sections will return higher values for BMD (Nikander *et al.*, 2005). In this respect, the present geometry analyses add substantive information to common BMD analyses and provide a tangible picture in understanding cortical bone structure.

However, due to the limited spatial resolution of the MR image data, our findings need to be interpreted with caution. Considering pixel size of 0.9×0.9 mm, we therefore restricted our commentary to locations which showed differences greater than the image resolution itself. Moreover, we had to enforce one pixel thick layer next to the inner trabecular region to maintain the anatomical continuity of cortical bone in regions where the cortical bone was not distinct in our segmentation procedure. The resolution of the present study meant that the thinnest cortical bone possible was 0.9 mm, which is in the middle of the range (0.6–1.2 mm) reported by Mayhew *et al.* (2005). Evidently, the actual cortical thickness can be even smaller at some locations approaching to the thickness of a single trabecular column (Verhulp *et al.*, 2008).

As regards to data extraction, there seems to be certain unresolved issues related to definitions and applications of geometrical parameters of cortical bone that could be discussed more thoroughly in literature. Firstly, when dealing with an analysis of 2D cross-sections, the definition of cortical thickness is tied strongly to the reference point. The norm is to take the centre of mass as a reference to calculate the thickness parameters, approximated by the geometrical centroid in this work due to the lack of mass information. However, this method in the thickness estimation in radial direction is not necessarily accurate in terms of mechanical forces imposed on that location during different physical activities. This is due to the fact that realistic 3D loading of the bone might differ from the assumed axial loading. Essentially, the plane of imaging during the image acquisition affects the 2D geometrical parameters extracted. Secondly, the method of estimating cortical thickness in the direction of the periosteal surface normal is also not a straightforward method, as the high curvature regions will give wildly varying values. Ultimately, the long axis of femoral neck might be the most reasonable reference for calculating the basic and derived geometrical parameters such as thickness, curvature, buckling ratio, etc., which would involve 3D data analysis extending the 2D work of Mourtada *et al.* (1996). Thirdly, the calculation of actual curvature of the bone surface proved to be non-trivial as well. As the curvatures graphs in Figs 3b and 5b illustrate, it is very hard to distinguish a pattern or get stable values for images at this resolution. The calculation of local curvature itself is not straightforward as it involves approximating the scattered boundary points with an *n*th degree polynomial (usually 3 or 4). Tests with a synthetic circle with a similar area and resolution as the cross-sections observed in our data showed that

even an addition of 10 dB white Gaussian noise warranted smoothing, through wider spans and filtering of the resulting curvature signal. 10 dB of noise for a circle of radius 20 is roughly the quantization error when converted into grid coordinates similar to our data. In this study, we smoothed the local curvature values calculated using a neighbourhood span. Thus, while it is agreed upon that the curvature dictates an important mechanical aspect (Mayhew *et al.*, 2005), it should be carefully balanced in interpretation keeping in mind the assumptions and approximations employed in its calculation. Indeed, a future perspective would be a whole 3D model of the proximal femur, with a more thorough analysis of the geometrical traits complemented by density data whenever ethically possible.

In conclusion, one-dimensional polar analysis of the geometrical traits coupled with an intuitive presentation of the comparative results, provides a basis for analysis with a high degree of angular accuracy than prevalent in current literature. In this work, our approach indicates that the odd-impact exercise loading, which imposes impacts on the proximal femur from varying directions, is associated with generally more robust cross-sectional geometry along the femoral neck.

Acknowledgments

Conflict of interest

All authors state that they have no conflicts of interest. Nathaniel Narra takes responsibility for the integrity of the data analysis.

References

Barratt DC, Chan CSK, Edwards PJ, Penney GP, Slomczykowski M, Carter TJ, Hawkes DJ. Instantiation and registration of statistical shape models of the femur and pelvis using 3D ultrasound imaging. *Med Image Anal* (2008); **12**: 358–374.

Bass SL, Saxon L, Daly RM, Turner CH, Robling AG, Seeman E, Stuckey S. The effect of mechanical loading on the size and shape of bone in pre-, peri-, and postpubertal girls: a study in tennis players. *J Bone Miner Res* (2002); **17**: 2274–2280.

Daly RM, Bass SL. Lifetime sport and leisure activity participation is associated with greater bone size, quality and strength in older men. *Osteoporos Int* (2006); **17**: 1258–1267.

Duncan RL. Mechanotransduction and the functional response of bone to mechanical strain. *Calcif Tissue Int* (1995); **57**: 344–358.

Frost HM. Bone 'mass' and the 'mechanostat': a proposal. *The Anatomical record* (1987); **219**: 1–9.

van de Giessen M, Foumani M, Streekstra GJ, Strackee SD, Maas M, Van Vliet LJ, Grimbergen K, Vos FM. Statistical descriptions of scaphoid and lunate bone shapes. *J Biomech* (2010); **43**: 1463–1469.

Griffith JF, Genant HK. New imaging modalities in bone. *Curr Rheumatol Rep* (2011); **13**: 241–250.

Heimann T, Meinzer H-P. Statistical shape models for 3D medical image segmentation: a review. *Med Image Anal* (2009); **13**: 543–563.

Heinonen A, Sievänen H, Kyröläinen H, Perttunen J, Kannus P. Mineral mass, size, and estimated mechanical strength of triple jumpers' lower limb. *Bone* (2001); **29**: 279–285.

Johannesdottir F, Poole KES, Reeve J, Siggeirsdottir K, Aspelund T, Mogensen B, Jonsson BY, Sigurdsson S, Harris TB, Gudnason VG, Sigurdsson G. Distribution of cortical bone in the femoral neck and hip fracture: a prospective case-control analysis of 143 incident hip fractures; the AGES-REYKJAVIK Study. *Bone* (2011); **48**: 1268–1276.

Kazakia GJ, Majumdar S. New imaging technologies in the diagnosis of osteoporosis. *Rev Endocr Metab Disord* (2006); **7**: 67–74.

Klein-Nulend J, Bakker AD. Osteocytes: mechanosensors of Bone and Orchestrators of Mechanical Adaptation. *Clin Rev Bone Miner Metab* (2008); **5**: 195–209.

Manske SL, Macdonald HM, Nishiyama KK, Boyd SK, McKay HA. Clinical Tools to Evaluate Bone Strength. *Clin Rev Bone Miner Metab* (2010); **8**: 122–134.

Mayhew PM, Thomas CD, Clement JG, Loveridge N, Beck TJ, Bonfield W, Burgoyne CJ, Reeve J. Relation between age, femoral neck cortical stability, and hip fracture risk. *Lancet* (2005); **366**: 129–135.

Mourtada FA, Beck TJ, Hauser DL, Ruff CB, Bao G. Curved beam model of the proximal femur for estimating stress using dual-energy X-ray absorptiometry derived structural geometry. *J Orthop Res* (1996); **14**: 483–492.

Nikander R, Sievänen H, Heinonen A, Kannus P. Femoral neck structure in adult female athletes subjected to different loading modalities. *J Bone Miner Res* (2005); **20**: 520–528.

Nikander R, Sievänen H, Uusi-Rasi K, Heinonen A, Kannus P. Loading modalities and bone structures at nonweightbearing upper extremity and weight-bearing lower extremity: a pQCT study of adult female athletes. *Bone* (2006); **39**: 886–894.

Nikander R, Kannus P, Dastidar P, Hannula M, Harrison L, Cervinka T, Narra NG, Aktour R, Arola T, Eskola H, Soimakallio S, Heinonen A, Hyttinen J, Sievänen H. Targeted exercises against hip fragility. *Osteoporos Int* (2009); **20**: 1321–1328.

Nikander R, Kannus P, Rantalainen T, Uusi-Rasi K, Heinonen A, Sievänen H. Cross-sectional geometry of weight-bearing tibia in female athletes subjected to different exercise loadings. *Osteoporos Int* (2010a); **21**: 1687–1694.

Nikander R, Sievänen H, Heinonen A, Daly RM, Uusi-Rasi K, Kannus P. Targeted exercise against osteoporosis: a systematic review and meta-analysis for optimising bone strength throughout life. *BMC Medicine* (2010b); **8**: 47.

Robling AG, Castillo AB, Turner CH. Biomechanical and molecular regulation of bone remodeling. *Annu Rev Biomed Eng* (2006); **8**: 455–498.

Sievänen H. A physical model for dual-energy X-ray absorptiometry-derived bone mineral density. *Invest Radiol* (2000); **35**: 325–330.

Sievänen H, Józsa L, Pap I, Järvinen M, Järvinen TA, Kannus P, Järvinen TL. Fragile external phenotype of modern human proximal femur in comparison with medieval bone. *J Bone Miner Res* (2007); **22**: 537–543.

Turner CH. Three rules for bone adaptation to mechanical stimuli. *Bone* (1998); **23**: 399–407.

Turner CH, Pavalko FM. Mechanotransduction and functional response of the skeleton to physical stress: the mechanisms and mechanics of bone adaptation. *J Orthop Sci* (1998); **3**: 346–355.

Verhulp E, van Rietbergen B, Huiskes R. Load distribution in the healthy and osteoporotic human proximal femur during a fall to the side. *Bone* (2008); **42**: 30–35.

Yushkevich PA, Piven J, Hazlett HC, Smith RG, Ho S, Gee JC, Gerig G. User-guided 3D active contour segmentation of anatomical structures: significantly improved efficiency and reliability. *NeuroImage* (2006); **31**: 1116–1128.

2

THE RELATIONSHIP BETWEEN LOADING HISTORY AND PROXIMAL FEMORAL DIAPHYSIS CROSS-SECTIONAL GEOMETRY

by

Niinimäki S, Narra N, Härkönen L, Abe S, Nikander R, Hyttinen J, Knüsel C, Sievänen H, Feb 2017

WILEY American Journal of Human Biology

The relationship between loading history and proximal femoral diaphysis cross-sectional geometry

Sirpa Niinimäki[1] | Nathaniel Narra[2] | Laura Härkönen[3,4] | Shinya Abe[5] |
Riku Nikander[6,7,8] | Jari Hyttinen[2] | Christopher Knüsel[9] | Harri Sievänen[10]

[1] Archaeology, P.O. Box 1000, University of Oulu, Oulu 90014, Finland

[2] Department of Electronics and Communications Engineering, BioMediTech, Tampere University of Technology, Tampere, Finland

[3] Department of Ecology, P.O. Box 3000, University of Oulu, Oulu 90014, Finland

[4] Department of Environmental and Biological Sciences, P.O. 111, University of Eastern Finland, Joensuu 80101, Finland

[5] Department of Mechanical Engineering and Industrial Systems, P.O. Box 589, Tampere University of Technology, Tampere 33101, Finland

[6] Unit of Health Sciences, Faculty of Sport and Health Sciences, P.O. Box 35, (L328), 40014 University of Jyväskylä, Finland

[7] GeroCenter Foundation for Aging Research and Development, Rautpohjankatu 8, Jyväskylä 40700, Finland

[8] Unit of Research & Education, Central Hospital of Central Finland, Keskussairaalantie 19, Jyväskylä 40620, Finland

[9] UMR5199, De la Prehistoire a l'Actuel: Culture, Environnement, et Anthropologie (PACEA), Bâtiment B8, Allée Géoffroy Saint Hilaire, CS 50023, Pessac Cedex 33615, France

[10] The UKK Institute for Health Promotion Research, P.O. Box 30, Kaupinpuistonkatu 1, Tampere 33501, Finland

Correspondence
Sirpa Niinimäki, Archaeology, P.O.
Box 1000, 90014 University of
Oulu, Oulu, Finland. Email sirpa.
niinimaki@oulu.fi

Abstract

Objectives: We investigated the relationship between loading history and bone biomechanical properties used in physical activity reconstructions. These bone properties included bone bending and torsional strength (J), cortical area (CA), the direction of the major axis (theta angle), and element shape ratios determined from cross sections of standardized bone length. In addition, we explored the applicability of anatomically determined cross sections.

Methods: Our material consisted of hip and proximal thigh magnetic resonance images of Finnish female athletes ($N = 91$) engaged in high-jump, triple-jump, endurance running, swimming, power-lifting, soccer and squash; along with a group of active non-athlete individuals ($N = 20$). We used regression analysis for size-adjustment, and the extracted residuals were then used to compare differences in the bone properties between groups.

Results: We found that triple-jumpers, soccer players, and squash players had the greatest values in CA and J, swimmers and non-athletes had the smallest, whereas high-jumpers, power-lifters, and endurance runners exhibited interim values. No between-the-group differences in element shape ratios or theta angles were found. We found that influences of activity were similar regardless of whether standardized length or anatomically determined cross sections were used.

Conclusions: Extreme (triple-jump) and directionally inconsistent loading (soccer and squash) necessitate a more robust skeleton compared to directionally consistent loading (high-jump, power-lifting, and endurance running) or non-impact loading

(swimming and non-athletes). However, not all of these relationships were statistically significant. Thus, information gained about physical activity using bone properties is informative but limited. Accounting for the limitations, the method is applicable on fragmented skeletal material as anatomically determined cross sections can be used.

1 | INTRODUCTION

Loading is important for maintenance of bone mass and has a mechanically appropriate distribution within the bone cross section (Forwood & Burr, 1993; Ruff, Holt, & Trinkaus, 2006). Loading history is therefore considered to be reflected in bone biomechanical properties which are the very foundation of activity reconstructions. Biomechanical properties of bones are a result of loading history and cumulative effects of activity, as the bone is thought to strengthen in response to the most commonly experienced direction of stress by overall shape adaptation (Forwood & Burr, 1993; Ruff et al., 2006). This is explained by beam theory: bone is biomechanically stronger the further away the periosteal contour is from the neutral bending axis of the bone (Lieberman, Polk, & Demes, 2004; Ruff et al., 2006; Stock & Shaw, 2007). Functional adaptation of bone reflects its mechanical environment: physical activity, body mass and muscle moment arm (Parfitt, 2004; Petit et al., 2004; Ruff, 2000a,; Ruff, Walker, & Trinkaus, 1994; Seeman et al., 1996; Schiessl, Frost, & Jee, 1998; Schoenau & Frost, 2002; Schoenau, Neu, Mokov, Wassmer, & Manz, 2000; Trinkaus, Churchill, & Ruff, 1994).

Conversely, bone is affected by unusual strains rather than repetitive daily activities. Bone is adapted to normal levels of stress, and a response occurs at higher or lower stress levels than the equilibrium range (Frost, 1987; Lanyon, 1987, 1996). Bone mass is increased if the stimulus is consistently high (within physiological and material limits) while decreased loading leads to removal of bone (Martin, 2007; Schoenau & Frost, 2002). Furthermore, to maintain bone mass a continued, loading-related stimulus is required (Lanyon, 1987, 1996). Lanyon (1987) has proposed that loading from atypical directions is more osteogenic than predictable, directionally consistent loading. Furthermore, Turner (1998) suggests that loading involving high impacts is the most osteogenic.

As the most commonly experienced direction of stress magnitude is considered to be reflected in the shape of bone shafts, bone cross-sectional properties have been used to reconstruct activity of past populations, especially with regard to mobility (Holt, 2003; Macintosh, Pinhasi, & Stock, 2014; Pomeroy 2013; Ruff, 2008; Ruff et al., 2015; Stock & Pfeiffer, 2001; Weiss, 2003), the effects of unilateral versus bilateral activity (Shaw & Stock, 2009b), combatant weapon preference on upper limb use (Rhodes & Knüsel, 2005; Sparacello, Pearson, Coppa, & Marchi, 2011), and sexual divi-

sion of labor (Macintosh et al., 2014; Sparacello et al., 2011; Wescott & Cunningham, 2006). Loading patterns are usually established, and have the most influence on morphology, in childhood (Ruff et al., 2006).

Activity reconstructions utilize differences between groups in bending and torsional rigidity (J), or in the element shape ratio (I_x/I_y). Effectively, in the case of the femur, bone antero-posterior diameter is considered to be reinforced with higher levels of mobility (Holt, 2003; Macintosh et al., 2014; Pomeroy, 2013; Ruff, 2008; Ruff et al., 2015; Wescott & Cunningham, 2006) whereas medio-lateral widening of the shaft is influenced to a large extent by pelvic breadth (Davies & Stock, 2014; Ruff, 2000a,,; Weaver, 2003).

Furthermore, as bone properties and muscle cross-sectional area are correlated, it has been proposed that cortical area (CA) could be a better proxy for physical activity reconstructions than bone shape or entheseal changes (Schoenau, Shaw, & Harvati, 2013; Slizewski, Burger-Heinrich, Francken, Wahl, & Harvati, 2014). However, large prediction errors have been raised as an issue (Shaw, 2010). The orientation of greatest bending rigidity, or of the major axis of the section called the theta angle, has been briefly considered in the evaluation of activity differences (Burr, Piotrowski, & Miller, 1981; Ruff, 1992; Sumner, Mockbee, Morse, Cram, & Pitt, 1985). Comparison of bone properties between living subjects with known activity patterns and levels to those of archaeological and fossil individuals can give valuable information when evaluating the living conditions of prehistoric humans and human ancestors (Scherf, Wahl, Hublin, & Harvati, 2016; Shaw & Stock, 2009a,).

The aim of this study is to investigate the relationship between loading histories and the bone biomechanical properties commonly used in activity reconstructions. We utilize data comprised of magnetic resonance images (MRI) of modern female athletes and a group of active non-athlete individuals. The data are coupled with reliable and accurate information on training history, body size, and age. High-jumpers, triple-jumpers, soccer and squash players, power-lifters, endurance runners, swimmers, and active non-athlete women are represented in our sample. The biomechanical properties of the athletes and non-athletes are compared and these properties are elaborated in terms of apparent loading patterns of these sports. In previously published research, it has been hypothesized as well as empirically attested that bone biomechanical properties are adapted to principal loading

directions (Forwood & Burr, 1993; Ruff et al., 2006; Shaw & Stock, 2009a), and that atypical loading directions are considered more osteogenic (Lanyon, 1987; Shaw & Stock, 2009a). In addition, bone biomechanical properties are affected by intensity of loading through muscle contraction and ground reaction forces (Frost, 1987; Heinonen, Sievänen, Kannus, Oja, & Vuori, 2002; Lanyon, 1987, 1996), repetitiveness or high number of loading cycles (Nikander, Sievänen, Heinonen, & Kannus, 2005; Nikander et al., 2009; Ruff et al., 2006), and high ground impacts (Heinonen, Sievänen, Kyröläinen, Perttunen, & Kannus, 2001; Nikander et al., 2005, 2009).

Soccer and squash involve ground reaction forces and great torque exerted on a single limb from rapidly accelerating/decelerating movements and quick turns of the body that translate into inconsistent loading directions at the hip region (Nikander et al., 2005, 2009). Powerful unilateral hip extension resulting in great torque through intense muscle forces acting around the femur occurs in these sports. Soccer and squash can be considered to consist of repetitive, intense loading from atypical directions and involve high ground impacts coming from odd directions. Atypical loading is directionally inconsistent and not primarily encountered in the course of everyday life, that is, locomotion and squatting representing general typical loading patterns. In addition, triple-jump is a sport in which training and competition consists of repetitive, intense loading. There is also a requirement for powerful unilateral hip extension coupled with forward motion. However, in triple-jump the encountered extreme ground impacts come from the axial direction. Ground impacts encountered in triple-jump are up to 20 times body weight or more (Heinonen et al., 2001). High-jump includes axially directed high ground impacts and powerful bilateral hip extension during typical sport performance and training (Nikander et al., 2009). Sprinting and powerful bilateral hip extension involved in the sport results in directionally consistent, intense loading. Long-distance running is an endurance sport that includes a great number of repetitive weight-bearing impacts with the ground, resulting in directionally consistent loading (Nikander et al., 2009). Power-lifting involves precise co-ordination of movements coupled with intense muscle force production (Nikander et al., 2009). In addition to the high static and transient loading (at lower rates than high-impact sports) of the bones, intense muscle forces also act to affect the stress experienced at the proximal femur. Power-lifting would arguably result in high directional compressional forces acting on the bone due to muscle activity. Running and power-lifting load the bones in directions similar to what is encountered in the course of everyday life, that is, locomotion and squatting, albeit at much-higher magnitudes and rates. Swimming is a non-impact sport, where intensity consists of muscle contraction only, rather than combined effects of muscle contraction and ground reaction forces as in the sports described above (Nikander et al., 2009). Competition and training in swimming consists of repetitive and directionally consistent loading coming from muscle contraction only, that is, without ground impacts.

We studied three different cross-sectional locations of the femur: the mid-shaft, the lesser trochanter, and the sub-trochanteric levels. Bone cross-sectional properties are usually studied using standardized geometric cross sections of bone length, such as 50% or 80% of total length (Mongle, Wallace, & Grine, 2015). However, estimating mid-shaft location—especially for poorly preserved long bones—will introduce a source of error which can affect comparisons between individuals (Mongle et al., 2015; Sládek, Berner, Galeta, Friedl, & Kudrnová, 2010). Should anatomically determined cross sections be operable, they would greatly enhance the applicability of biomechanical properties for activity reconstructions, especially in the absence of bone length information when dealing with incomplete skeletal data. The results of this study are relevant to considering the applicability of specific bone biomechanical properties as the basis for activity reconstruction, and how different proximal femur cross sections reflect the loading history of this weight-bearing bone.

2 | MATERIALS AND METHODS

The study material consisted of proximal femur MR images (1.5T Avanto Syngo MR B15, Siemens, Erlangen, Germany) of 91 female athletes and 20 active non-athlete females obtained from previous studies of the hip-joint (Nikander et al., 2009) and proximal thigh (Sikiö et al., 2013). The athletes were recruited through their respective associations and clubs. The non-athletes were students recruited from nearby medical and nursing schools. The non-athletes did not practice any sport at a competitive level and were only involved in recreational physical activity two to three times a week. All the study participants were asked about potential factors affecting bone metabolism, such as medications, diseases, menstrual status, use of hormonal contraceptives, calcium intake, alcohol, tobacco, and coffee consumption, as well as their history of previous injuries and fractures. The study protocol was approved by the Ethics Committee of Pirkanmaa District Hospital, and each participant gave her written informed consent prior to the measurements.

Several sports with differing loading patterns were represented in the sample: 10 high-jumpers, 9 triple-jumpers, 9 soccer players, 10 squash players, 17 power-lifters, 18 endurance runners, and 18 swimmers. Loading history was established by considering both typical sport performance as well as the typical training form. The athletes' sports specific training hours per week and competing career in years are given in Table 1. Training hours of non-athletes are also

TABLE 1 Descriptive group statistics [mean (±SD)] and between-group differences in bone properties of the femur shaft

Variable	High-jump (N = 10)	Triple-jump (N = 9)	Soccer (N = 9)	Squash (N = 10)	Power-lifting (N = 17)	Endurance run (N = 18)	Swimming (N = 18)	Non-athletes (N = 20)	P
Age	22 (4)	23 (4)	21 (3)	29 (7)	28 (6)	29 (6)	20 (2)	24 (4)	
Height	178 (4)	170 (4)	162 (5)	168 (9)	158 (3)	168 (5)	173 (5)	164 (5)	
Weight	60 (5)	60 (6)	58 (7)	64 (9)	63 (13)	54 (3)	65 (6)	60 (7)	
Bi-iliac breadth	290 (15)	266 (22)	263 (12)	265 (15)	259 (21)	273 (16)	282 (16)	274 (12)	
Sports specific training	11 (3)	12 (2)	11 (1)	8 (3)	9 (3)	11 (3)	20 (4)	3 (1)	
Competitive career	11 (4)	10 (3)	9 (3)	10 (6)	8 (5)	12 (7)	9 (3)		
Femoral head height	46 (2)	43 (2)	42 (1)	42 (3)	41 (2)	43 (1)	44 (2)	42 (2)	
Femoral head-neck length	97 (3)	91 (4)	89 (5)	92 (6)	86 (4)	91 (4)	93 (5)	91 (4)	
Lesser trochanter									
CA	360 (49)	395 (45)	341 (66)	346 (47)	295 (39)	301 (40)	301 (37)	281 (42)	**.000**
J	94015 (22039)	93161 (9897)	80978 (13618)	90038 (24252)	72257 (16642)	79115 (17563)	76665 (14130)	68990 (18064)	**.000**
Theta	0.5 (24.6)	4.2 (23.3)	4.2 (14.7)	7.0 (13.9)	2.4 (16.6)	1.9 (16.6)	2.7 (14.6)	−2.6 (17.4)	.971
Ratio	0.7 (0.3)	0.7 (0.2)	0.7 (0.1)	0.7 (0.1)	0.7 (0.1)	0.7 (0.1)	0.7 (0.1)	0.7 (0.1)	.920
Sub-trochanter									
CA	384 (60)	457 (43)	382 (53)	413 (50)	356 (53)	352 (41)	353 (43)	341 (47)	**.000**
J	59657 (10676)	57029 (9049)	49945 (8625)	56109 (15124)	13551 (3084)	14934 (3571)	14371 (3041)	13036 (2982)	**.000**
Theta	−11.0 (44.6)	7.0 (47.3)	26.3 (56.1)	26.4 (52.6)	48.4 (28.3)	41.0 (34.8)	22.6 (57.1)	44.4 (32.8)	.423
Ratio	1.0 (0.2)	1.0 (0.2)	1.1 (0.3)	1.1 (0.2)	1.1 (0.2)	1.1 (0.2)	1.1 (0.1)	1.1 (0.2)	**.016**
Mid-shaft									
CA	452 (50)	486 (47)	420 (49)	437 (59)	360 (52)	380 (40)	357 (38)	343 (41)	**.000**
J	57256 (12682)	55825 (10207)	45756 (9206)	48515 (12357)	33624 (8845)	41017 (8416)	36687 (6072)	33537 (8164)	**.000**
Theta	−54.1 (19.2)	−31.3 (66.3)	−52.0 (53.7)	−66.9 (12.8)	−51.1 (46.2)	−66.7 (35.6)	−33.9 (65.3)	−33.9 (67.4)	**.015**
Ratio	1.2 (0.3)	1.3 (0.1)	1.5 (0.3)	1.3 (0.2)	1.3 (0.2)	1.5 (0.2)	1.4 (0.3)	1.5 (0.3)	.373

Age in years, height in cm, weight in kg, training in hours per week, competitive career in years, CA in mm^2, J in mm^4, theta in degrees. Significance for P values P < .05, boldfaced.
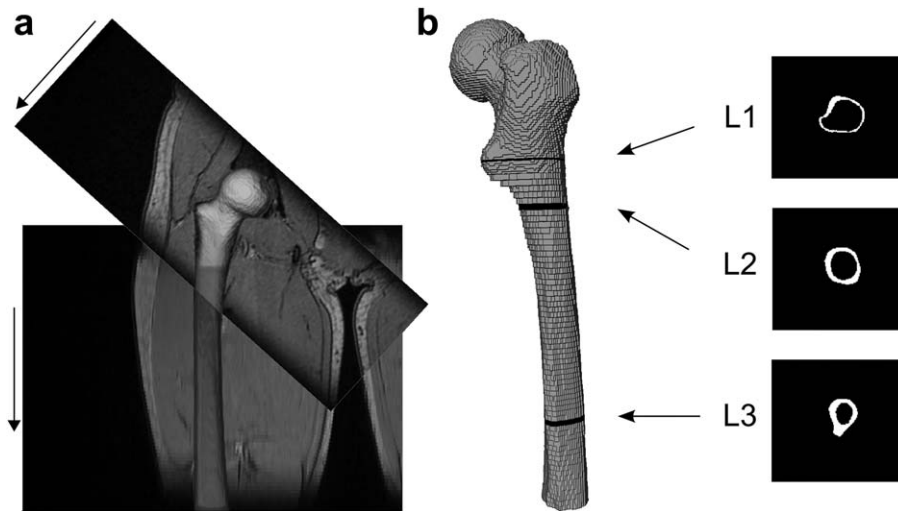
FIGURE 1 (a) Coronal images from the two MR image sub-volumes (hip and proximal thigh). The black arrows indicate the direction of tomographic scans and are perpendicular to the cross-sectional plane for the corresponding image volume. (b) Identified locations for performing cross-sectional analysis of the bone biomechanical properties.L1: at the level of lesser trochanter; L2: at the sub-trochanter level; L3: at 50% of estimated physiological femur shaft length

given. The dominant leg (ie, take-off and kicking leg) of each of the volunteers was scanned. The tomographic image data for every subject consist of a 3D stack of contiguous 2D cross-sectional images of a single thigh (left or right), henceforth referred to as an image volume. The 3D MR image acquisition protocols were such that the anatomy of the proximal half of the femur was scanned in two separate sections, or sub-volumes, of femoral head (pixel size: 0.9115×0.9115 mm; slice thickness: 1 mm) and shaft (pixel size: 0.8125×0.8125 mm; slice thickness: 3 mm). The femoral head image volume extends from the femoral caput to the sub-trochanteric region of the shaft, with the imaging plane oriented axially to the oblique femoral neck axis. The proximal shaft image volume extends distally 210–240 mms from the trochanteric region, with the imaging plane oriented perpendicularly to the length of the supine subject.

The cortical bone in these two anatomical sections was individually segmented from the respective image volumes. The segmentation was performed manually using ITK-snap (Yushkevich et al., 2006). The orientations of segmented volumes were aligned in Avizo (VSG/FEI, Mérignac Cedex, France) using the global coordinate system information in the DICOM files of the image datasets.

Subsequently, all 111 segmented femora were made anatomically consistent by mirroring the left femur (about the sagittal plane) to mimic the right. Three anatomical locations were identified for the cross-sectional analysis of the femur: lesser trochanter, sub-trochanter, and mid-shaft (Figure 1). The lesser trochanter region is located in the femoral head section of the image data, where the image slices are perpendicular to the oblique neck axis. This results in a very oblique cross-sectional slice at the level of the lesser trochan-

ter. Thus, it was necessary to transform the geometric orientation of the segmented femur by rotating it in the coronal plane such that the resulting cross-sectional planes were perpendicular to the shaft axis. To calculate the shaft axis, the solidity parameter for each cross section in the original orientation was calculated. The distal-end cross sections with a solidity parameter higher than 0.95 were deemed suitable for consideration. The solidity parameter is a measure of the circularity of a given shape −1 for a circle, and decreases with increasing eccentricity in shape. The shaft axis was calculated by collecting a contiguous set of cross sections (starting from the most distal), which have solidity above 0.95, and fitting a 3D line vector to their geometric centroids. The desired angle for rotating the volume was calculated based on the coronal projection of this vector.

Selection of the cross-sectional location was carried out as follows. The location of the lesser trochanter was defined by the maximal protrusion of the trochanteric process, selected from the above described re-oriented segmented femur. The sub-trochanter cross section was similarly manually determined by tracing the location commonly used for osteometric measurements of proximal femur shaft diameter (Wescott, 2005). The location was determined by identifying a site where the medial neck-shaft junction and lesser trochanter curvature were no longer visible, while in all subjects the locations should be within about 1–2 cm below the maximum lesser trochanter transverse width. This location is present in the shaft section of the image data, where the cross sections are axial to the long axis of the body. Thus, for selecting this cross section, the segmented femur was already oriented appropriately. Similarly, the mid-shaft cross section was determined from the shaft image data section. In

previous literature, standardized cross sections of the femur were observed at 50% of femur length for maximum length, physiological length, or biomechanical length (Davies & Stock, 2014; Mongle et al., 2015; Ruff & Hayes, 1983). In our material, due to the absence of the distal diaphysis in this dataset, it was necessary to estimate the femur length from the available physiological parameters for every subject. Maximum femur length or biomechanical femur length could not be obtained for the individuals in the MRI study, but physiological femur length (Martin & Saller, 1957) could be regressed from stature using its similarity to the anthropometric measurement of femur length (Montagu, 1960). It should be noted that cross sections standardized to physiological femur length are located more proximally compared to cross sections standardized to maximum length and biomechanical length (Mongle et al., 2015; Ruff & Hayes, 1983). The relationship between physiological femur length and stature was based on a sample of modern Finnish females (age 18–25, $N = 85$; unpublished data by SN) using the following formula:

$$\text{Stature} * 0.309 - 10.602 \;\left(\text{Adjusted } R^2 0.577; \; \text{SEE } 1,971\right).$$

The half-length measurement obtained, offset from the location of the greater trochanter, indicates the appropriate cross section. As the greater trochanter and the mid-shaft regions are in two separate image data sections, it was necessary to combine the two corresponding sections of the segmented femur in a common coordinate system. During the segmentation procedure, the 3D positional information for every pixel was retained and used to create a composite of the entire available segmented proximal femur. The 3D visualization of this composite was used in extracting the 50% location of the shaft with respect to the superior apex of the greater trochanter.

2.1 | Measurements of bone properties and data analyses

CA (unit mm^2) represents bone resistance to axial tensile or compression loads. Second moments of area (I, unit mm^4), also called area moments of inertia, represent bending rigidity at a given plane. For this study, four moments of inertia were measured, including those around the medio-lateral axis in the antero-posterior plane (I_x), the antero-posterior axis in the medio-lateral plane (I_y), and the maximum (I_{max}), and minimum (I_{min}) shaft diameter. Torsional rigidity is described by the value J, which measures torsional and average (twice) bending strength (O'Neill & Ruff, 2004; Ruff, 2003). It is derived from summing two perpendicular moment areas indicated by I. Therefore, $J = I_x + I_y$ or $I_{max} + I_{min}$ (unit mm^4; O'Neill & Ruff, 2004; Ruff, 2003). Bone shape can be assessed by dividing I_x by I_y, whereupon relative circularity of the cross section can be evaluated. Finally, the theta angle was acquired as the angle between I_x

and I_{max} axes, which represents the orientation of greatest bending rigidity or the major axis of the section.

Bone biomechanical properties scale to body size (Brianza et al., 2007; Parfitt, 2004; Petit et al., 2004; Ruff, 2000a,; Ruff et al., 1994; Schiessl et al., 1998; Schoenau et al., 2000; Schoenau & Frost, 2002; Seeman et al., 1996; Trinkaus et al., 1994). Before analyzing any external effects on bone properties, potential individual size effects contributing to the observed variation in measured properties should be accounted for. As we recognize that human size is multi-dimensional, we took several measurements of body size and dimensions from the MR images of the subjects. Body height was measured against the wall with a tape measure and body mass (as weight) with scales at the same time as the MR imaging was done (Nikander et al., 2009). Pelvic width was measured from the MR images as hemi-pelvic breadth from the outer edge of the iliac blade to the mid-line of the sacrum. This measurement, multiplied by two, will yield the bi-iliac breadth (BIB) measurement (Martin & Saller, 1957), commonly used in body weight reconstructions (Ruff, 2000b; Ruff, Niskanen, Junno, & Jamison, 2005). Femoral head supero-inferior height (FHSI) was measured at the middle of the femoral caput for maximum diameter in the para-sagittal plane (Martin & Saller, 1957). This measurement is considered to correlate with weight and indicates skeletal robustness at the end of growth period (Ruff, 2003). Femoral head-neck length (FHNL) was measured from the most lateral point of the greater trochanter to the superior surface of the femoral caput (Lovejoy, 1975; Martin & Saller, 1957). This measurement contributes to body breadth and thus influences the moment arms of the muscles crossing the hip-joint (Ruff, 2005).

The effects of the size variables (weight, height, BIB, FHNL, FHSI; Table 1) were removed from each of the response variables statistically. Owing to significant correlations between human size variables (eg, in this study; Table 2), it often becomes problematic to use different size variables in the models simultaneously. Therefore, a principal components analysis (PCA) was conducted for the five size variables. The main objective here was to obtain a principal component (PC) that would provide an accurate summary of the size variable relationships among the subjects. This procedure further helps to avoid problems with multicollinearity that may arise if two or more of the explanatory variables are highly correlated. The obtained component score includes the contribution of all-original variables. A regression model was fitted for the relevant response variables (CA and J at different levels) by entering the PC1 score as a linear predictor (Ceyhan & Goad, 2009; Corruccini, 1987; Smith, 1994). The residuals describe the variation among individuals that is left over once the regression model has been run to control for confounding variables, in this case the combined effect of

TABLE 2 Correlations between original size variables

Pairwise Pearson Correlations					
	Height	Weight	Femoral head-neck length	Bi-iliac breadth	Femoral head height
Height	1				
Weight	0.336[a]	1			
Femoral head-neck length	0.672[a]	0.274[a]	1		
Bi-iliac breadth	0.515[a]	0.196[b]	0.610[a]	1	
Femoral head height	0.645[a]	0.320[a]	0.599[a]	0.425[a]	1

[a]Correlation is significant at the 0.01 level (2-tailed).
[b]Correlation is significant at the 0.05 level (2-tailed).

size variables. The size-adjusted residual values for CA and J were further compared with respect to activity loading type. The residual values for CA and J followed a normal distribution. Second moment of inertia ratios and theta angles are size-free variables (see also Corruccini & Ciochon, 1976) and used as ratios or angles in activity reconstructions (eg, Macintosh et al., 2014; Ruff, 1992; Ruff et al., 2015; Sparacello et al., 2011; Wescott & Cunningham, 2006); therefore, it is not necessary to regress these variables against PC1.

Size-adjusted CA and J, second moment of inertia ratios (I_x/I_y), and theta angles were then compared between groups using one-way analysis of variance (ANOVA; Table 1). A relevant post hoc analysis was performed on those response variables found to differ between groups (Figure 2A–H). Tukey's post hoc analysis was performed when variances were equal and Games-Howell post hoc analysis was performed when variances were unequal. Equality of variances was checked with Levene's test. All the statistical analyses were executed using the statistical program SPSS 21.0 for Windows (IBM SPSS Statistics for Windows, Version 21.0. Armonk, NY: IBM Corp. released, 2012).

3 | RESULTS

Descriptive group statistics are presented in Table 1. The PCA yielded one component that had an eigenvalue higher than 1 and the component explained a total of 58.8% variance (Table 3). All body size variables (body height and weight, femoral head height, FHNL, and BIB), with body height in particular, loaded highly with this component, thus providing a satisfactory summary of the size variable relationships among the individuals (Table 3). Higher CA and J were associated with higher PC1 scores. PC1 contributed significantly to CA at the sub-trochanteric level ($F_{1, 106} = 18.325$, $P < .001$, $R^2 = 0.149$), at the level of lesser trochanter ($F_{1, 106} = 18.336$, $P < .001$, $R^2 = 0.149$) and at 50% of the physiological femur shaft ($F_{1, 106} = 25.407$, $P < .001$,

$R^2 = 0.195$). PC1 also affected J at the sub-trochanteric level ($F_{1, 106} = 60.460$, $P < .001$, $R^2 = 0.365$), at the level of the lesser trochanter ($F_{1, 106} = 41.351$, $P < .001$, $R^2 = 0.283$) and at 50% of the physiological femur shaft ($F_{1, 106} = 49.969$, $P < .001$, $R^2 = 0.322$). Thus, size as represented by PC1 affected CA and J significantly at each measured level. However, the contribution of size explaining variation in CA was lower (14.9–19.5%) than in J (28.3–36.5%). As predicted, the effect of size on theta angles and shape ratios at each level were statistically non-significant. To reveal activity-related differences in bone properties (without the confounding effect of size differences), the effect of size was removed using the PC1 scores in regression analyses for each CA and J (at different levels of the femur).

When the size effect on a bone property was significant, size-adjusted residuals from regressions were extracted to be used as response variables in ANOVA. Means and standard errors of the mean of the response variables are presented to illustrate variation between groups in those bone response variables found to differ according to one-way ANOVA analysis (Table 1, Figure 2A–H). Triple-jumpers had the greatest CA and J values whereas soccer and squash players had the second greatest values; high-jumpers, power-lifters and endurance runners exhibited interim values, and finally swimmers and non-athletes had the smallest values (Table 1, Figure 2A–F). These trends were similar for CA and J for all studied cross-sectional locations, although triple-jumpers were associated with soccer and squash players J values at sub-trochanteric and lesser trochanter levels, and high-jumpers with soccer and squash players in CA and J values at the 50% cross-sectional level and soccer and squash player CA values at the lesser trochanter level.

While there were differences between groups according to one-way ANOVA analysis, not all differences were statistically significant, as is evident visually from the overlapping standard errors (± 2) of means (Figure 2A–F). The following
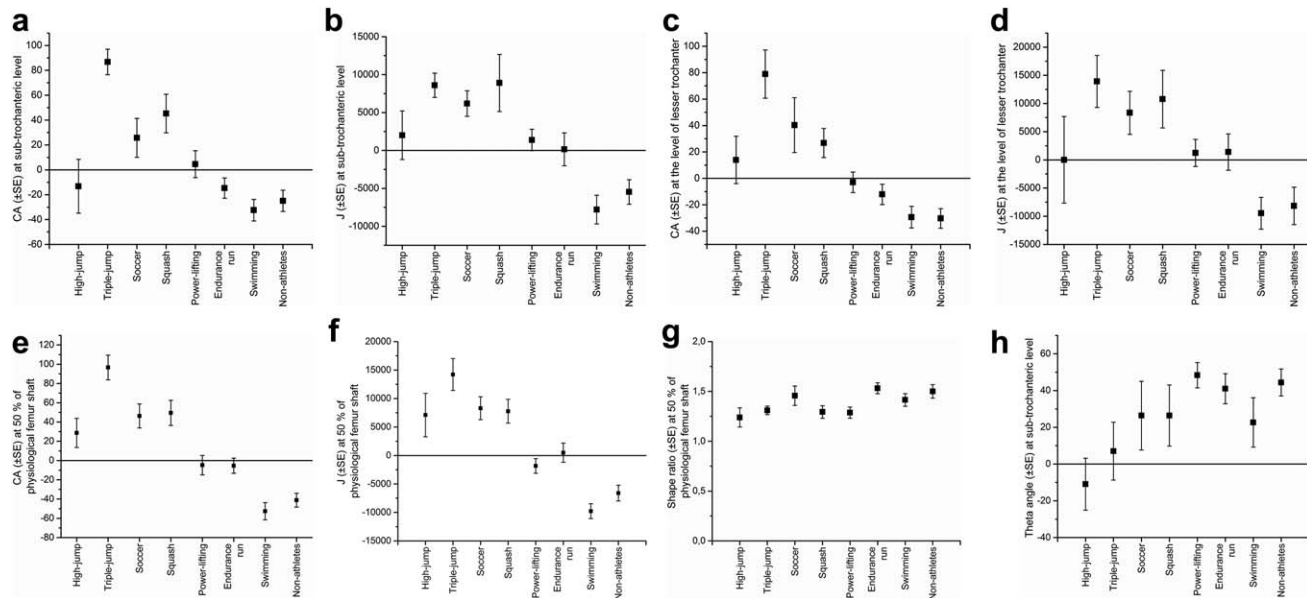
FIGURE 2 (a) Residual values of CA at the sub-trochanteric level, mean and standard errors. Differences are significant according to the post hoc test ($P < .05$) in triple-jumpers compared to high-jumpers, power-lifters, endurance runners, swimmers and non-athletes, and between squash players and swimmers and non-athletes. (b) Residual values of J at the sub-trochanteric level, mean and standard errors. Differences are significant according to the post hoc test ($P < .05$) in triple-jumpers, soccer and squash players, and power-lifters compared to swimmers and non-athletes. (c) Residual values of CA at the level of lesser trochanter, mean and standard errors. Differences are significant according to the post hoc test ($P < .05$) in triple-jumpers compared to power-lifters, endurance runners, swimmers, and non-athletes. In addition, significant differences were found in squash players compared to swimmers and non-athletes. (d) Residual values of J at the level of lesser trochanter, mean and standard errors. Differences are significant according to post hoc test ($P < .05$) in triple-jumpers compared to swimmers and non-athletes. In addition, a significant difference was found in squash players compared to swimmers. (e) Residual values of CA at the 50% level of physiological shaft length of the femur in swimmers, mean and standard errors. Differences are significant according to the post hoc test ($P < .05$) in triple-jumpers compared to power-lifters, endurance runners, swimmers, and non-athletes. In addition, significant differences were found in soccer players and squash players compared to swimmers and non-athletes. Finally, squash players were significantly different from endurance runners. (f) Residual values of J at the 50% level of physiological shaft length of the femur, mean and standard errors. Differences are significant according to the post hoc test ($P < .05$) in triple-jumpers compared to power-lifters, endurance runners, swimmers, and non-athletes. In addition, significant differences were found in soccer and squash players compared to power-lifters, swimmers and non-athletes. Finally, high jumpers were significantly different from swimmers. (g) Shape ratio at the 50% level of physiological length of the femur shaft, mean and standard errors. There were no significant group differences in shape ratios in post hoc analysis. (h) Theta angle at sub-trochanteric level, mean and standard errors. The only statistically significant difference was found between high-jumpers and power-lifters. Note that standard error margins are overlapping

between-groups differences were significant according to relevant post hoc tests. At the sub-trochanteric level triple-jumpers had the greatest CA values compared to all-other groups (Figure 2A). In addition, squash players had greater CA compared to swimmers and non-athletes at the sub-trochanteric level (Figure 2A). Triple-jumpers had the greatest CA values also at the lesser trochanter, and this was statistically significant compared to power-lifters, endurance runners, swimmers, and non-athletes (Figure 2C). At the lesser trochanter, statistically significant differences were found in squash players compared to swimmers and non-athletes (Figure 2C). Triple-jumpers had also the greatest CA values at the level of the 50% cross section of the femur length compared to power-lifters, endurance runners,

swimmers, and non-athletes (Figure 2E). Soccer players and squash players had greater CA compared to swimmers and non-athletes, and squash players compared to endurance runners at the level of 50% cross section (Figure 2E). At the sub-trochanteric level, significant differences in J values were found in triple-jumpers, soccer and squash players, and power-lifters compared to swimmers and non-athletes (Figure 2B). At the lesser trochanter level, significant differences in J values were found only when comparing triple-jumpers to swimmers and non-athletes, and squash players to swimmers (Figure 2D). At the 50% cross section of the femur length, triple-jumpers and soccer and squash players had greater J values compared to power-lifters and endurance runners as well as compared to swimmers and non-athletes

TABLE 3 Results of principal components analysis

Principal component Variable	CO	PC1 Loadings
Body height	0.753	0.868
Femoral head-neck length	0.732	0.855
Femoral head height	0.639	0.799
Bi-iliac breadth	0.551	0.742
Body weight	0.264	0.514
Eigenvalue		2.938
Percentage of variance explained		58.76

Communalities (CO), trait loadings, eigenvalues, and explanatory variances are given for PC1.

(Figure 2F). High-jumpers had greater *J* values compared to those of swimmers at the 50% cross section of the femur length (Figure 2F).

Ratios of second moment of area and theta angles were not significantly different between groups and exhibited no particular trends, apart from the theta angle at the sub-trochanteric level and ratios at the mid-shaft cross-sectional level (Table 1, Figure 2G,H). According to post hoc tests, the only significant difference was between high-jumpers and power-lifters in the sub-trochanteric theta angle (Figure 2H).

4 | DISCUSSION

We set out to investigate whether different loading histories are reflected in those specific bone biomechanical properties traditionally used to reconstruct physical activity. We also examined whether biomechanical properties gained from anatomically determined cross sections, when compared to properties gained from cross sections of standardized length, reflect loading history differently. We found that, in general, triple-jumpers and soccer and squash players had more robust proximal femoral shaft as indicated by CA and *J* values compared to those of swimmers and non-athletes, regardless of whether these properties were observed from standardized cross-sectional slices or from anatomically determined cross sections. It should be noted, however, that as mid-shaft is estimated from femoral length, it will introduce a small error source when comparing different individuals (Mongle et al., 2015; Sládek et al., 2010). The estimation produces generally low errors (Mongle et al., 2015; Sládek et al., 2010), and as the present material is a single population, the results should be fairly accurate.

Biomechanical behavior of bones scales allometrically with body mass: bones become proportionately shorter and

proportionally distribute bone tissue further from the cross-sectional centroid with increased mass (Brianza et al., 2007). Thus, biomechanical properties are intrinsically affected by body size and dimensions (Parfitt, 2004; Petit et al., 2004; Ruff, 2000a; Schiessl et al., 1998; Schoenau et al., 2000; Schoenau & Frost, 2002; Seeman et al., 1996). Before any between-group comparisons can be made, it is necessary to adjust for size effects. Body size, or lean body mass, is usually considered the main contributor to variation in bone biomechanical properties (Parfitt, 2004; Petit et al., 2004; Seeman et al., 1996; Schiessl et al., 1998; Schoenau et al., 2000; Schoenau & Frost, 2002). Biomechanical properties have therefore been scaled against weight (Parfitt, 2004; Petit et al., 2004; Ruff et al., 1994; Seeman et al., 1996; Schiessl et al., 1998; Schoenau et al., 2000; Schoenau & Frost, 2002), sometimes height (Feik, Thomas, & Clement, 1996), or a product of (reconstructed) body weight and muscle moment arm length (Ruff, 2000a,). Usually, the moment arm is represented by long bone length, although long bone length alone does not provide an accurate enough scale for body size and lever arm length (Ruff, 2000a). Lower limb medio-lateral diaphyseal cross sections, especially of the proximal femur, are influenced by body breadth (Davies & Stock, 2014; Shaw & Stock, 2011). We recognized that human size is rather multidimensional, and we took this into account by scaling for combined effects of different size parameters. Our material permitted inclusion of indicators of muscle levers and skeletal frame size (BIB, FHNL, FHSI), in addition to weight and height, which is not always the case when working on archaeological or anatomical skeletal material. Therefore, our results permitted controlling for size factors quite effectively.

We did not use any *a priori* grouping of the sports according to perceived loading similarities; rather we compared the biomechanical properties of the bones between each sports group to identify similarities among the groups. According to our results triple-jumpers possessed the highest CA and *J* values and soccer and squash players the second highest; endurance runners and power-lifters—and in some locations high-jumpers—exhibited interim values; and swimmers and non-athletes had the lowest values (Figure 2A–F). High CA values (Figure 2A,C,E) were to be expected in triple-jump considering the extreme magnitude of reaction force imposed axially on a single leg (Heinonen et al. 2001), but similar bending and torsion strength in triple-jump compared to soccer and squash was unexpected (Figure 2B,D). The extreme impact loading in triple-jumping is axial in direction, that is, its effect on bone mass is not directional in a transverse plane. Although there is more directionality (forward motion) in a transverse plane in triple-jumping compared with more varying loading patterns in soccer and squash, apparently these sports do share commonality in that

they involve powerful unilateral hip extension with great torque and a lot of force repetitively affecting a single leg at the level of the proximal femur. Thus, loading in these sports arises from repetitive muscle contraction and high ground impacts—in the case of triple-jumping, extreme impacts—but as they do not produce specific patterns in mediolateral or anteroposterior directions, the result is overall strengthening of the proximal femur. When compared to regular, mostly unidirectional loading from locomotion, activities with directionally inconsistent loading will necessitate a more robust shape adaptation. Thus, our results corroborate the hypothesis that loading from atypical directions results in a greater osteogenic response (Lanyon, 1987). Our results also support the results of previous studies (Nikander et al., 2005, 2009; Ruff et al., 2006) where repetitiveness or high number of loading cycles are needed for changes in bone bending and torsion resistance.

Individuals engaged in endurance running and power-lifting had less robust proximal femora compared to the above described athlete groups characterized by repetitive, directionally inconsistent loading, and, in the case of triple-jump, extreme impact loading. Power-lifting is characterized by slow, coordinated movements and it involves negligible ground impacts compared to high-jumping and endurance running. Conversely, endurance-running involves less intense muscle loading compared to power-lifting. While running and squatting—motions involved in endurance running and power-lifting—can be considered to represent loading to which the skeleton (proximal femur) is arguably adapted, these occur at higher magnitudes and rates than in non-athletes. High-jumpers provided a somewhat interesting group regarding the resultant bone biomechanical properties. High-jumpers were associated with power-lifters and endurance runners in J and CA values at the sub-trochanteric level and J values at lesser trochanter levels, but with soccer and squash players at CA and J values at the 50% femur shaft and CA values at the lesser trochanter level (Figure 2A–F). High-jumping consists of sprinting and bilateral hip extension coupled with high impact loading, although the impacts are not as extreme as in triple-jumping (Milan, 2010). Training and competition in high-jumping consists of less repetitive sports-specific (ie, high jumps) events compared to endurance running which has a huge number of successive repeated loadings. Apparently, high impacts contribute to higher CA at lesser trochanter and mid-shaft levels reflecting the high impacts involved, but bilateral jumping motion results in directionally consistent loading at sub-trochanteric and lesser trochanter levels. Therefore, although sports like high-jumping, endurance running and power-lifting are quite different as activities, they are common in producing directionally consistent loading patterns.

The importance of impact loading on bone strength was evident in the results; in our sample the highest ground reaction forces were produced among triple-jumpers (Heinonen et al., 2001) and these individuals possessed ultimately the highest CA values (Figure 2A,C,E). This corroborates Turner (1998), who suggested that high-impact loading results in greater osteogenic response. High impacts—although not as great in magnitude—are also produced in high-jumping and playing soccer and squash, which was evident in the high CA and J values also observed in these groups (Figure 2A–F). While impact loading in triple-jumping and high-jumping is applied axially, playing soccer and squash result in impacts coming from odd directions but in a transverse plane (Nikander et al., 2005, 2009; Nikander, Sievänen, Uusi-Rasi, Heinonen, & Kannus, 2006; Nikander, Sievänen, Heinonen, Karstila, & Kannus, 2008). Underlining the importance of impact loading, the swimmers and non-athletes of our sample—the individuals with least impact loading in their activity—possessed the smallest values in CA and J (Figure 2A–F). While swimming is also an endurance sport with a great number of repetitive movements, it lacks ground impact or weight-bearing in general (Nikander et al., 2009). In fact, swimmers in this sample had the smallest CA and J values, even compared to those of non-athletes, although this difference was not statistically significant (Figure 2A–F). It was shown in previous studies that biomechanical loading in swimming and cycling results in an insufficient stimulus for inducing a geometrically significant bone adaptation at the proximal femur (Duncan et al., 2002; Heinonen et al., 1993; Nikander et al., 2006). This was reflected in the results of this study as well (Figure 2A–F). While swimming does have a torsional effect on the humerus and produces a more circular bone element (Shaw & Stock, 2009b), with respect to the proximal femur our study results show no circularity or shape differences between swimmers and other groups. This may be due to the greater differences in range of motion and utilization of muscles between arms and legs during swimming.

In terms of geometric indicators of bone strength (ie, cross sectional properties), we found that vigorous weight-bearing loading is an important factor in buttressing bone robustness through geometric adaptation. Thus, involvement in sports *per se* is not necessarily evident as greater bone strength compared to that of non-athletes, as shown by the comparison of swimmers with the non-athlete group in this study. Power-lifters possessed interim values even though their sport-specific activities load their femurs against much-greater weight than their body weight. Rather, it seems that greater CA and J values are achieved when activity involves high single limb torque, that is, multidirectional loading and/or high to extreme ground impacts.

In our data, proximal femur shaft bone shape ratios are a poor variable for reconstructions of physical activity. Although CA and J values varied between the groups, no

significant differences in bone shape ratios were found (Table 1, Figure 2G). Shape ratios could not distinguish between sports loading the proximal femur with directional consistency and those where the loading was directionally inconsistent. Even when comparing power-lifters and endurance runners—with higher magnitudes and loads generated for locomotion and squatting than compared to those occurring in everyday life—to soccer and squash players with more varied loading directions, there were no differences in shape. The effects of *Psoas major* and *Iliacus* muscle pull on the shape and especially orientation of the lesser tubercle should have been most evident, directly at the lesser trochanter and indirectly at the sub-trochanteric cross sections. The more posteriorly oriented the tubercle, the greater the leverage for *Psoas major* and *Iliacus* muscles should be, resulting in a greater antero-posterior diameter of the cross section. However, this was not supported by our results. Apparently, changes in one moment of the inertia axis results in a proportional change in the perpendicular moment of the inertia axis, regardless of size (results were similar when analyses were repeated with size-scaled ratios, data not shown). This proportional change was similar across all-sports categories and when compared to those of non-athlete individuals. Similarly, theta angle was a poor variable for activity reconstruction as it could not discriminate between the sport groups in this study (Table 1). The lack of difference in the theta angle could indicate that regimented sports training and activity is not sufficient to significantly and consistently vary the orientation of the major axis. It is worth noting that the large standard deviations in the observed angles indicate that this parameter is not stable for single cross sections across subjects and thus not a reliable parameter.

Our results confirm previous studies (Holt, 2003; Macintosh et al., 2014; Pomeroy, 2013; Ruff, 2008; Ruff et al., 2015; Wescott & Cunningham, 2006) suggesting that activity can be reconstructed utilizing bending and torsional rigidity (J) of the proximal femur. We could distinguish four groups described by similar values of CA and J: extreme loading (triple-jumpers), directionally inconsistent loading (soccer and squash players), directionally consistent loading (high-jumpers, endurance runners, and power-lifters) and a non-loading group (swimmers and non-athletes). However, only extreme loading and directionally inconsistent loading were statistically significantly different from non-loading groups. It has also been suggested that, as CA and muscle cross-sectional area are correlated, CA could be used to approximate muscle size and therefore, indirectly, activity (Slizewski et al., 2013, 2014). In our sample CA and J showed similar responses to loading, that is, specific groups are described by similar CA and J values in their relation to CA and J values of other groups. Therefore, CA can also be considered to reflect activity, at least the impact loading component involved in the activity (Table 1, Figure 2A–F). Bone shape as element shape ratio (I_x/I_y) or orientation of theta angle did not vary with activity in our sample. In terms of physical activity reconstructions, these results mean that activities consisting of directionally inconsistent loading and/or high ground impacts are reflected in bone strength but not bone shape.

When considering these results one should bear in mind that modern-day sports have very distinctive patterns of activity compared to those of past societies. In addition, power-lifters begin their competitive training at a significantly later age compared to other sports. Swimmers included significantly more sport-specific training hours per week compared to other sports. Finally, the age at menarche relative to starting competitive training is not known. There are potential effects on responsiveness to bone loading should the starting age relative to menarche vary between the sports groups, and this may have influenced the results. However, these results underline the relevance of directionally inconsistent loading and high ground impacts for osteogenic responses. The effect of muscle loading may increase the potential to distinguish more varied loading patterns. Similarly, more detailed anatomically oriented shape analysis with regard to cortical bone distribution may provide additional parameters for separating loading patterns (Narra, Nikander, Viik, Hyttinen, & Sievänen, 2013).

We found that cross-sectional properties taken from standardized lengths were comparable to those from anatomical cross sections. As there are problems in estimating standardized bone lengths, especially when bones are fragmented (Mongle et al., 2015; Sládek et al., 2010), anatomical cross sections would reduce this source of error. However, the estimation error should also be studied for anatomically determined cross-sectional properties.

5 | CONCLUSIONS

Activity reconstructions are based on the notion that daily repetitive loading modifies bone cross-sectional shape and bone strength along the femoral shaft, and that those patterns are likely established in childhood (Ruff et al., 2006). Different loading histories are found to affect bone mass and its distribution (eg, Narra et al., 2013; Nikander et al., 2005, 2009; Rantalainen, Nikander, Daly, Heinonen, & Sievänen, 2011; Rantalainen, Nikander, Heinonen, Suominen, & Sievänen, 2010). According to our results, this loading history affects proximal femoral bone strength measures of CA and J more than shape ratios or theta angles indicative of shape. The results of this study based on female athletes and non-athletes suggest that bone biomechanical properties at the proximal femur diaphysis do reflect loading history, and the effects of loading are similar regardless of whether

standardized length, as the 50% femur shaft, or anatomically determined locations, as the lesser trochanter or subtrochanter locations, are used. These results make activity reconstructions possible for incomplete skeletal data from the proximal femur. However, due to great error variances, only those activities involving directionally inconsistent loading or extreme ground impacts can be separated reliably based on bone properties (J, CA) from those activities that consist of minimal ground impacts at the proximal femur diaphysis. Element shape ratios or theta angles do not allow any inferences to be made about activity history. It should be noted that these results are pertinent to the proximal femur diaphysis only. Analyses on other skeletal elements, such as the tibia, may show different responses to activity. Furthermore, while this limits the usefulness of bone properties for analyzing undocumented skeletal remains, it does mean that individuals engaged in multidirectional loading regimes can be distinguished from those who had not engaged, or do not engage, in such activities.

ACKNOWLEDGMENTS

AUTHOR CONTRIBUTIONS

SN, HS and RN designed the study, and directed implementation and data collection. SN, NN, LH, and SA analyzed the data. SN and NN drafted the manuscript. HS, CK, JH, RN, SA and LH edited the manuscript for intellectual content and provided critical comments on the manuscript.

REFERENCES

Brianza, S. Z. M., D'amelio, P., Pugno, N., Delise, M., Bignardi, C., & Isaia, G. (2007). Allometric scaling and biomechanical behaviour of the bone tissue: An experimental intraspecific investigation. *Bone*, *40*, 1635–1642.

Burr, D. B., Piotrowski, G., & Miller, G. J. (1981). Structural strength of the macaque femur. *American Journal of Physical Anthropology*, *54*(3), 305–319.

Ceyhan, E., & Goad, C. L. (2009). A comparison of analysis of covariate-adjusted residuals and analysis of covariance. *Communications in Statistics Simulation and Computation*, *38*, 2019–2038.

Corruccini, R. S. (1987). Shape in morphometrics: Comparative analyses. *American Journal of Physical Anthropology*, *73*, 289–230.

Corruccini, R. S., & Ciochon, R. L. (1976). Morphometric affinities of the human shoulder. *American Journal of Physical Anthropology*, *45*, 19–38.

Davies, T. G., & Stock, J. T. (2014). The influence of relative body breadth on the diaphyseal morphology of the human lower limb. *American Journal of Human Biology*, *26*, 822–835.

Duncan, G. S., Blimke, C. R. J., Cowell, C. T., Burke, S. T., Briody, J. N., & Howman-Giles, R. (2002). Bone mineral density in adolescent female athletes: Relationship to exercise type and muscle strength. *Medicine and Science in Sports Exercise*, *34*(2), 286–294.

Feik, S. A., Thomas, C. D. L., & Clement, J. G. (1996). Age trends in remodeling of the femoral midshaft differ between the sexes. *Journal of Orthopaedic Research*, *14*, 590–597.

Forwood, M. R., & Burr, D. B. (1993). Physical activity and bone mass: Exercises in futility? *Bone and Mineral*, *21*(2), 89–112.

Frost, H. M. (1987). Bone "mass" and the "mechanostat". A proposal. *The Anatomical Record*, *219*(1), 1–9.

Heinonen, A., Oja, P., Kannus, P., Sievänen, H., Mänttäri, A., & Vuori, I. (1993). Bone mineral density of female athletes in different sports. *Bone and Mineral*, *23*(1), 1–14.

Heinonen, A., Sievänen, H., Kannus, P., Oja, P., & Vuori, I. (2002). Site-specific skeletal response to long-term weight training seems to be attributable to principal loading modality: A pQCT study of female weightlifters. *Calcified Tissue International*, *70*(6), 469–474.

Heinonen, A., Sievänen, H., Kyröläinen, H., Perttunen, J., & Kannus, P. (2001). Mineral mass, size, and estimated mechanical strength of triple jumpers' lower limb. *Bone*, *29*(3), 279–285.

Holt, B. M. (2003). Mobility in Upper Paleolithic and Mesolithic Europe: Evidence from the lower limb. *American Journal of Physical Anthropology*, *122*, 200–215.

IBM Corp. (2012) IBM SPSS Statistics for Windows, Version 21.0. Armonk, NY: IBM Corp.

Lanyon, L. E. (1987). Functional strain in bone tissue as an objective and controlling stimulus for adaptive bone remodeling. *Journal of Biomechanics*, *20*, 1083–1093.

Lanyon, L. E. (1996). Using functional loading to influence bone mass and architecture: Objectives, mechanisms, and relationship with estrogen of the mechanically adaptive process in bone. *Bone*, *18(*1)*Suppl 1*, S37–S43.

Lieberman, D. E., Polk, J. D., & Demes, B. (2004). Predicting long bone loading from cross-sectional geometry. *American Journal of Physical Anthropology*, *123*, 156–171.

Lovejoy, C. O. (1975). Biomechanical perspective on the lower limb of early hominids. In R. H. Tuttle (Ed.), *Primate functional morphology and evolution* (pp. 291–326). The Hague: Mouton.

Macintosh, A. A., Pinhasi, R., & Stock, J. T. (2014). Lower limb skeletal biomechanics track long-term decline in mobility across ~6150 years of agriculture in Central Europe. *Journal of Archaeological Science*, *52*, 376–390.

Martin, R. B. (2007). The importance of mechanical loading in bone biology and medicine. *Journal of Musculoskeletal and Neuronal Interactions*, 7(1), 48–53.

Martin, R., & Saller, K. (1957). *Lehrbuch der anthropologie, band I*. Stuttgart: Fischer.

Milan, Č. (2010). Biomechanical characteristics of take-off action in high jump – a case study. *Serbian Journal of Sports Sciences*, 4(4), 127–135.

Mongle, C. S., Wallace, I. J., & Grine, F. E. (2015). Cross-sectional structural variation relative to midshaft along hominine diaphyses. II. The hind limb. *American Journal of Physical Anthropology*, 158(3), 398–407.

Montagu, M. F. A. (1960). *A handbook of anthropometry*. Springfield, Illinois: Charles C Thomas Publisher.

Narra, N., Nikander, R., Viik, J., Hyttinen, J., & Sievänen, H. (2013). Femoral neck cross-sectional geometry and exercise loading. *Clinical Physiology and Functional Imaging*, 33, 258–266.

Nikander, R., Kannus, P., Dastidar, P., Hannula, M., Harrison, L., Cervinka, T., ... Sievänen, H. (2009). Targeted exercises against hip fragility. *Osteoporosis Internaional*, 20, 1321–1328.

Nikander, N., Sievänen, H., Heinonen, A., & Kannus, P. (2005). Femoral neck structure in adult female athletes subjected to different loading modalities. *Journal of Bone and Mineral Research*, 20(3), 520–528.

Nikander, R., Sievänen, H., Heinonen, A., Karstila, T., & Kannus, P. (2008). Load-specific differences in the structure of femoral neck and tibia between world-class moguls skiers and slalom skiers. *Scandinavian Journal of Medicine and Science in Sports*, 18, 145–153.

Nikander, N., Sievänen, H., Uusi-Rasi, K., Heinonen, A., & Kannus, P. (2006). Loading modalities and bone structures at nonweight-bearing upper extremity and weight-bearing lower extremity: A pQCT study of adult female athletes. *Bone*, 39, 886–894.

O'Neill, M. C., & Ruff, C. B. (2004). Estimating human long bone cross-sectional geometric properties. A comparison of noninvasive methods. *Journal of Human Evolution*, 47, 221–233.

Parfitt, A. M. (2004). The attainment of peak bone mass: What is the relationship between muscle growth and bone growth? *Bone*, 34, 767–770.

Petit, M. A., Beck, T. J., Lin, H.-M., Bentley, C., Legro, R. S., & Lloyd, T. (2004). Femoral bone structural geometry adapts to mechanical loading and is influenced by sex steroids: The Penn State young women's health study. *Bone*, 35, 750–759.

Pomeroy, E. (2013). Biomechanical insights into activity and long distance trade in the south-central Andes (AD 500–1450). *Journal of Archaeological Science*, 40, 3129–3140.

Rantalainen, T., Nikander, R., Daly, R. M., Heinonen, A., & Sievänen, H. (2011). Exercise loading and cortical bone distribution at the tibial shaft. *Bone*, 48, 786–791.

Rantalainen, T., Nikander, R., Heinonen, A., Suominen, H., & Sievänen, H. (2010). Direction-specific diaphyseal geometry and mineral mass distribution of tibia and fibula: A pQCT study of female athletes representing different exercise loading types. *Calcified Tissue International*, 86, 447–454.

Rhodes, J. A., & Knüsel, C. J. (2005). Activity-related skeletal change in medieval humeri: Cross-sectional and architectural alterations. *American Journal of Physical Anthropology*, 128, 536–546.

Ruff, C. (1992). Biomechanical analyses of archaeological human skeletal samples. In S. R. Saunders & M. A. Katzenberg (Eds.), *Skeletal biology of past peoples: Research methods* (pp. 37–58). New York: Wiley-Liss.

Ruff, C. B. (2000a). Body size, body shape, and long bone strength in modern humans. *Journal of Human Evolution*, 38, 269–290.

Ruff, C. (2000b). Body mass prediction from skeletal frame size in elite athletes. *American Journal of Physical Anthropology*, 113, 507–517.

Ruff, C. (2003). Growth in bone strength, body size, and muscle size in a juvenile longitudinal sample. *Bone*, 33, 317–329.

Ruff, C. (2005). Mechanical determinants of bone form: Insights from skeletal remains. *Journal of Musculoskeletal and Neuronal Interactions*, 5(3), 202–212.

Ruff, C. B. (2008). Femoral/humeral strength in early African *Homo erectus*. *Journal of Human Evolution*, 54, 383–390.

Ruff, C. B., & Hayes, W. (1983). Cross-sectional geometry of Pecos Pueblo femora and tibiae – a biomechanical investigation. I. Method and general patterns of variation. *American Journal of Physical Anthropology*, 60(3), 359–381.

Ruff, C., Holt, B., Niskanen, M., Sladek, V., Berner, M., Garofalo, M., ... Whittey, E. (2015). Gradual decline in mobility with adoption of food production in Europe. *Proceedings of the National Academy of Sciences of the United States of America*, 112(23), 7147–7152.

Ruff, C., Holt, B., & Trinkaus, E. (2006). Who's afraid of the Big Bad Wolff? "Wolff's law" and bone functional adaptation. *American Journal of Physical Anthropology*, 129, 484–498.

Ruff, C., Niskanen, M., Junno, J.-A., & Jamison, P. (2005). Body mass prediction from stature and bi-iliac breadth in two high latitude populations, with applications to earlier higher latitude humans. *Journal of Human Evolution*, 48, 381–392.

Ruff, C. B., Walker, A., & Trinkaus, E. (1994). Postcranial robusticity in Homo. III: Ontogeny. *American Journal of Physical Anthropology*, 93, 35–54.

Scherf, H., Wahl, J., Hublin, J.-J., & Harvati, K. (2016). Patterns of activity adaptation in humeral trabecular bone in Neolithic humans and present-day people. *American Journal of Anthropology*, 159, 106–115.

Schiessl, H., Frost, H. M., & Jee, W. S. S. (1998). Estrogen and bone-muscle strength and mass relationships. *Bone*, 22(1), 1–6.

Schoenau, E., & Frost, H. M. (2002). The "muscle-bone unit" in children and adolescents. *Calcified Tissue International*, 70, 405–407.

Schoenau, E., Neu, C. M., Mokov, E., Wassmer, G., & Manz, F. (2000). Influence of puberty on muscle area and cortical area of the forearm in boys and girls. *Journal of Clinical Endocrinology Metabolism*, *85*(3), 1095–1098.

Seeman, E., Hopper, J. L., Young, N. R., Formica, C., Goss, P., & Tsalamandris, C. (1996). Do genetic factors explain associations between muscle strength, lean mass, and bone density? A twin study. *American Journal of Physiology Endocrinology and Metabolism*, *270*, E320–E327.

Shaw, C. N. (2010). 'Putting flesh back onto the bones?' Can we predict soft tissue properties from skeletal and fossil remains? *Journal of Human Evolution*, *59*, 484–492.

Shaw, C. N., & Stock, J. T. (2009a). Intensity, repetitiveness, and directionality of habitual adolescent mobility patterns influence the tibial diaphysis morphology of athletes. *American Journal of Physical Anthropology*, *140*, 149–159.

Shaw, C. N., & Stock, J. T. (2009b). Habitual throwing and swimming corresponds with upper limb diaphyseal strength and shape in modern human athletes. *American Journal of Physical Anthropology*, *140*, 160–172.

Shaw, C. N., & Stock, J. T. (2011). The influence of body proportions on femoral and tibial midshaft shape in hunter-gatherers. *American Journal of Physical Anthropology*, *144*(1), 22–29.

Shaw, C. N., & Stock, J. T. (2013). Extreme mobility in the Late Pleistocene? Comparing limb biomechanics among fossil *Homo*, varsity athletes and Holocene foragers. *Journal of Human Evolution*, *64*, 242–249.

Sikiö, M., Harrison, L. C. V., Nikander, R., Ryymin, P., Dastidar, P., Eskola, H. J., & Sievänen, H. (2013). Influence of exercise loading on magnetic resonance image texture of thigh soft tissues. *Clinical Physiology and Functional Imaging*, *34*(5), 370–376.

Sládek, V., Berner, M., Galeta, P., Friedl, L., & Kudrnová, Š. (2010). Technical note: The effect of midshaft location on the error ranges on femoral and tibial cross-sectional parameters. *American Journal of Physical Anthropology*, *141*, 325–332.

Slizewski, A., Burger-Heinrich, E., Francken, M., Wahl, J., & Harvati, K. (2014). Pilot study for reconstruction of soft tissues: Muscle cross-sectional area of the forearm estimated from cortical bone for a Neolithic sample. *The Anatomical Record*, *297*, 1103–1114.

Slizewski, A., Schoenau, E., Shaw, C., & Harvati, K. (2013). Muscle area estimation from cortical bone. *The Anatomical Record*, *296*, 1695–1707.

Smith, R. J. (1994). Degrees of freedom in interspecific allometry: An adjustment for the effects of phylogenetic constraint. *American Journal of Physical Anthropology*, *93*, 95–107.

Sparacello, V. S., Pearson, O. M., Coppa, A., & Marchi, D. (2011). Changes in robusticity in an Iron Age agropastoralist group: The Samnites from the Alfedena necropolis (Abruzzo, Central Italy). *American Journal of Physical Anthropology*, *144*, 119–130.

Stock, J. T., & Pfeiffer, S. (2001). Linking structural variability in long bone diaphyses to habitual behaviors: Foragers from the Southern African Later Stone Age and the Andaman Islands. *American Journal of Physical Anthropology*, *115*, 337–348.

Stock, J. T., & Shaw, C. N. (2007). Which measures of diaphyseal robusticity are robust? A comparison of external methods of quantifying the strength of long bone diaphyses to cross-sectional geometric properties. *American Journal of Physical Anthropology*, *134*, 412–423.

Sumner, D. R., Mockbee, B., Morse, K., Cram, T., & Pitt, M. (1985). Computed tomography and automated image analysis of prehistoric femora. *American Journal of Physical Anthropology*, *68*(2), 225–232.

Trinkaus, E., Churchill, S. E., & Ruff, C. (1994). Postcranial robusticity in Homo. II: Humeral bilateral asymmetry and bone plasticity. *American Journal of Physical Anthropology*, *93*, 1–34.

Turner, C. H. (1998). Three rules for bone adaptation to mechanical stimuli. *Bone*, *23*(5), 399–407.

Weaver, T. D. (2003). The shape of the Neandertal femur is primarily the consequence of a hyperpolar body form. *Proceedings of the National Academy of Sciences of the United States of America*, *100*(12), 6926–6929.

Weiss, E. (2003). Effects of rowing on humeral strength. *American Journal of Physical Anthropology*, *121*, 293–302.

Wescott, D. J. (2005). Population variation in femur subtrochanteric shape. *Journal of Forensic Sciences*, *50*(2), 1–8.

Wescott, D. J., & Cunningham, D. L. (2006). Temporal changes in Arikara humeral and femoral cross-sectional geometry associated with horticultural intensification. *Journal of Archaeological Science*, *33*(7), 1022–1036.

Yushkevich, P. A., Piven, J., Hazlett, H. C., Smith, R. G., Ho, S., Gee, J. C., & Gerig, G. (2006). User-guided 3D active contour segmentation of anatomical structures: Significantly improved efficiency and reliability. *Neuroimage*, *131*(3), 1116–1128.
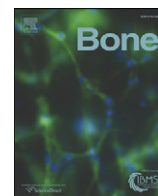

3

EXERCISE LOADING HISTORY AND FEMORAL NECK STRENGTH IN A SIDEWAYS FALL: A THREE-DIMENSIONAL FINITE ELEMENT MODELING STUDY

by

Abe S, Narra N, Nikander R, Hyttinen J, Kouhia R & Sievänen H, Nov 2016

Full Length Article

Exercise loading history and femoral neck strength in a sideways fall: A three-dimensional finite element modeling study

Shinya Abe [a,*], Nathaniel Narra [b], Riku Nikander [c,d,e], Jari Hyttinen [b], Reijo Kouhia [a], Harri Sievänen [f,**]

[a] Department of Mechanical Engineering and Industrial Systems, Tampere University of Technology, Tampere, Finland
[b] Department of Electronics and Communications Engineering, BioMediTech, Tampere University of Technology, Tampere, Finland
[c] Gerontology Research Center, Department of Health Sciences, University of Jyväskylä, Jyväskylä, Finland
[d] Central Hospital of Central Finland, Jyväskylä, Finland
[e] GeroCenter Foundation for Aging Research and Development, Jyväskylä, Finland
[f] The UKK Institute for Health Promotion Research, Tampere, Finland

A R T I C L E   I N F O

A B S T R A C T

Over 90% of hip fractures are caused by falls. Due to a fall-induced impact on the greater trochanter, the posterior part of the thin superolateral cortex of the femoral neck is known to experience the highest stress, making it a fracture-prone region. Cortical geometry of the proximal femur, in turn, reflects a mechanically appropriate form with respect to habitual exercise loading. In this finite element (FE) modeling study, we investigated whether specific exercise loading history is associated with femoral neck structural strength and estimated fall-induced stresses along the femoral neck. One hundred and eleven three-dimensional (3D) proximal femur FE models for a sideways falling situation were constructed from magnetic resonance (MR) images of 91 female athletes (aged 24.7 ± 6.1 years, >8 years competitive career) and 20 non-competitive habitually active women (aged 23.7 ± 3.8 years) that served as a control group. The athletes were divided into five distinct groups based on the typical loading pattern of their sports: high-impact (H-I: triple-jumpers and high-jumpers), odd-impact (O-I: soccer and squash players), high-magnitude (H-M: power-lifters), repetitive-impact (R-I: endurance runners), and repetitive non-impact (R-NI: swimmers). The von Mises stresses obtained from the FE models were used to estimate mean fall-induced stresses in eight anatomical octants of the cortical bone cross-sections at the proximal, middle, and distal sites along the femoral neck axis. Significantly ($p < 0.05$) lower stresses compared to the control group were observed: the H-I group — in the superoposterior (10%) and posterior (19%) octants at the middle site, and in the superoposterior (13%) and posterior (22%) octants at the distal site; the O-I group — in the superior (16%), superoposterior (16%), and posterior (12%) octants at the middle site, and in the superoposterior (14%) octant at the distal site; the H-M group — in the superior (13%) and superoposterior (15%) octants at the middle site, and a trend ($p = 0.07$, 9%) in the superoposterior octant at the distal site; the R-I group — in the superior (14%), superoposterior (23%) and posterior (22%) octants at the middle site, and in the superoposterior (19%) and posterior (20%) octants at the distal site. The R-NI group did not differ significantly from the control group. These results suggest that exercise loading history comprising various impacts in particular is associated with a stronger femoral neck in a falling situation and may have potential to reduce hip fragility.

© 2016 Elsevier Inc. All rights reserved.

1. Introduction

Bone structure adapts to habitual mechanical loading [1,2]. Walking, as the predominant form of human locomotion, causes higher compressive stress at the inferior cortex and smaller tensile stress at the superior cortex of the femoral neck. This asymmetric loading results in a thicker inferior and thinner superior cortical bone [3,4]. With aging, cortical thinning becomes evident; the thickness of the posterior part of the superolateral cortex, called the superoposterior cortex, declines from a mean 1.6 mm at the age of 25 to 0.3 mm at the age of 85 years in females [4,5]. Mayhew and colleagues [4] suggested that the thinning of the superoposterior cortex contributes significantly to hip fragility. Cortical thinning increases the elastic instability of the cortical shell and can lead to a fracture because of local buckling under compressive load [4]. When one falls sideways, the superolateral cortex experiences unusually high compressive stress due to a high impact force imposed on the greater trochanter [6,7]. The peak magnitude of such a fall-induced stress can

be 4 times greater than the stress induced by normal gait [3]. Accordingly, it has been speculated that the fracture initiates from this thin cortical layer of the superolateral region [4,7,8]. Several finite element (FE) modeling and cadaveric experimental studies have consistently shown that a sideways fall exposes the femoral neck to the greatest risk of a fracture [7,9–13]. Indeed, over 90% of hip fractures are directly caused by falls [14,15]. Therefore, if the superolateral cortical thickness could be maintained or even increased with appropriate exercise training, bone strength may be maintained and hip fracture risk reduced in old age.

In our previous studies [16,17], we found that female athletes with a history of high impact and/or impact exercises from unusual directions have higher areal bone mineral density (aBMD), section modulus, and thicker cortical bone of the femoral neck including the superolateral cortex. However, the influence of this exercise-induced structural benefit on femoral neck strength in the sideways fall was not examined. Several FE modeling studies have been conducted to obtain a better understanding of the hip fracture mechanism [3,6,9,11–13,18–22]. To the best of our knowledge, however, no FE modeling study has so far been conducted to investigate the influence of specific exercise loading history on the structural strength of the femoral neck in a falling situation. In particular, it is not known whether specific exercise loading history is associated with lower stresses during a fall.

The purpose of the present study is to investigate whether the femoral necks adapted to distinct exercise loading patterns show different stress profiles in a sideways fall. For this purpose, proximal femur FE models were created from three-dimensional (3D) image data of 111 female participants with distinct exercise loading histories. These results are expected to provide further insight into the potential of specific exercise types in strengthening the proximal femur and alleviating hip fracture risk.

2. Materials and methods

2.1. Participants

Magnetic resonance (MR) image data of proximal femurs from 91 adult female athletes (aged 24.7 ± 6.1 years) competing actively at national or international level and 20 habitually active, but non-competitive female control participants (aged 23.7 ± 3.8 years) were obtained from our previous study [17]. The study protocol was approved by the Ethics Committee of the Pirkanmaa Hospital District, and written informed consent was obtained from each participant before the study.

The athletes were recruited from national sports associations and local athletic clubs, and the control participants were mostly students from local medical and nursing schools. The control participants did recreational exercise 2–3 times a week, but had previously never taken part in any competitive sports. The athletes comprised nine triple-jumpers, ten high-jumpers, nine soccer players, ten squash players, 17 power-lifters, 18 endurance runners, and 18 swimmers. According to our previous exercise classification scheme [16,23], the athletes were divided into five different groups based on the typical loading patterns of their sports: high-impact (H-I) (triple- and high-jumpers); odd-impact (O-I) (soccer and squash players); high-magnitude (H-M) (power-lifters); repetitive-impact (R-I) (endurance runners); and the repetitive, non-impact group (R-NI) (swimmers).

Wearing only light indoor clothing without shoes, the body height and weight of the participants were measured using standard methods. Questionnaires were completed by all participants in order to obtain their training history including weekly sport-specific training hours and the number of training sessions during at least the five preceding years. Other information such as medications, diseases, menstrual status, use of hormonal contraceptives, calcium intake, alcohol, smoking, coffee consumption, and previous injuries and fractures was also collected [17].

2.2. MR image scanning procedure

The hip regions of all participants were scanned using a 1.5-T MR imaging system (Avanto Syngo MR B15, Siemens, Erlangen, Germany). The scanned region covered the proximal femur from the top of the femoral head to the subtrochanteric level of the femoral diaphysis. Using two half-Fourier acquisition single-shot turbo spin-echo localization series, sagittal, axial, and coronal images of the hip region of the dominant side were scanned. The reconstructed imaging plane was adjusted so that the cross-sectional plane of the femoral neck was perpendicular to the femoral neck axis. The MR imaging sequence used was a standardized axial T1-weighted gradient echo volumetric interpolated breath-hold (VIBE)-examination with the following parameters: FOV 35 × 26 cm, TR 15.3 ms, TE 3.32 ms, slice thickness 1 mm without gaps, echo train length = 1, flip angle = 10°, matrix 384 × 288, the in-plane resolution (pixel size) 0.9 mm × 0.9 mm [17].

2.3. FE model construction

The MR images of all participants were first manually segmented by delineating the periosteal and endocortical boundaries of the cortical bone using a touch panel (Wacom Tablet Cintiq 12WX, Wacom Technology Corp., Vancouver, WA, USA) with ITK-SNAP (www.itksnap.org) image processing software [24]. The in vivo precision of periosteal and endocortical delineations of the femoral neck cortex is about 1% [17, 25]. The segmented bone geometries were then converted into a volume mesh using the free mesh generation MATLAB (MathWorks, Inc., Natick, MA, USA) tool called iso2mesh [26]. The surface was then smoothed in MeshLab (Visual Computing Lab – ISTI – CNR, http://meshlab.sourceforge.net/) using a method described by Taubin [27]. This method was chosen for its known performance in minimizing the shrinkage of the geometry during the smoothing process. The smoothed proximal femur geometries were subsequently imported into SolidWorks (SolidWorks Corp., Waltham, MA, USA) for the generation
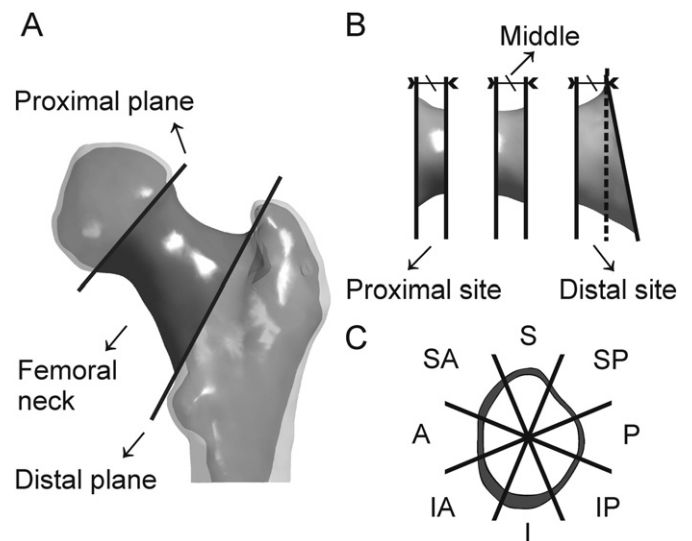

Fig. 1. Division of the femoral neck volume into anatomical sites and octants for the estimation of octant cortical stresses. (A) Posterior view of proximal femur. Dark grey-colored geometry defines the femoral neck geometry of interest. The proximal cross-sectional plane of the defined neck geometry was located at the femoral head-neck junction dividing the femoral head and the femoral neck. The distal plane was adjusted so that the distal plane met following conditions: its superior side is close to trochanteric fossa-greater trochanter junction, its anterior side is close to intertrochanteric line, and its inferior side is close to the lesser trochanter. This distal plane divides the trochanteric region and the femoral neck. (B) The division of the defined femoral neck regions into proximal, middle, and distal sites. The length of the superior surface was kept same for all sites. (C) The equal 45° anatomical octant division in the cross-section of the femoral neck. The femoral neck axis was used as the center of octant division.

of 3D solid bodies. The resulting proximal femur geometry comprised individually segmented cortical bone and trabecular bone volumes, the latter denoting the volume within the endocortical bone boundary. Although trabecular bone is truly a porous structure, in the present study it was modeled as a non-porous homogeneous material.

The individual 3D solid body geometries of the proximal femur were finally imported into ANSYS 16.1 (ANSYS Inc., Houston, PA, USA) for the FE meshing and model analysis. The ANSYS Academic Research license was obtained from CSC – IT Center for Science Ltd. (Espoo, Finland). First, the femoral neck geometry was defined (Fig. 1), and then similar boundary conditions (BCs) from the previous studies [22,28] were used in the present study. Force and restraining BCs were applied through the femoral head and trochanter-protecting polymethyl methacrylate (PMMA) caps, and aluminum distal pot (Fig. 2). A 10-noded tetrahedral finite element was used to mesh all materials. The element size was set to 1 mm for the entire proximal femur bone geometry, the caps, and the boundary between the distal end of the bone and the distal pot. The body of the distal pot, away from the boundary, was meshed with a 4 mm element size. The maximum error in octant stress (described in Section 2.4) was estimated based on the converged solution that was obtained by extrapolating the results from the 3 mm, 2 mm, 1.5 mm, 1 mm, and 0.75 mm FE mesh models. The estimated errors were 6.7%, 4.2%, 3.4%, 2.4%, and 2.1% for the 3 mm, 2 mm, 1.5 mm, 1 mm, 0.75 mm meshes, respectively. Based on these findings, a 1 mm mesh element size for the models in this study was deemed satisfactory. On average, each bone model comprised approximately 1,600,000 elements and 2,300,000 nodes. The cortical and trabecular bones of the proximal femur were modeled as homogeneous isotropic, linear elastic materials. Young's moduli of 17 GPa [29–31], 1500 MPa [30,31], 70 GPa [22], and 2 GPa [22] were set for the cortical, trabecular bone, the aluminum distal pot, and the protecting PMMA caps, respectively. Poisson's ratio was assumed as 0.33 [29–31] for all materials.
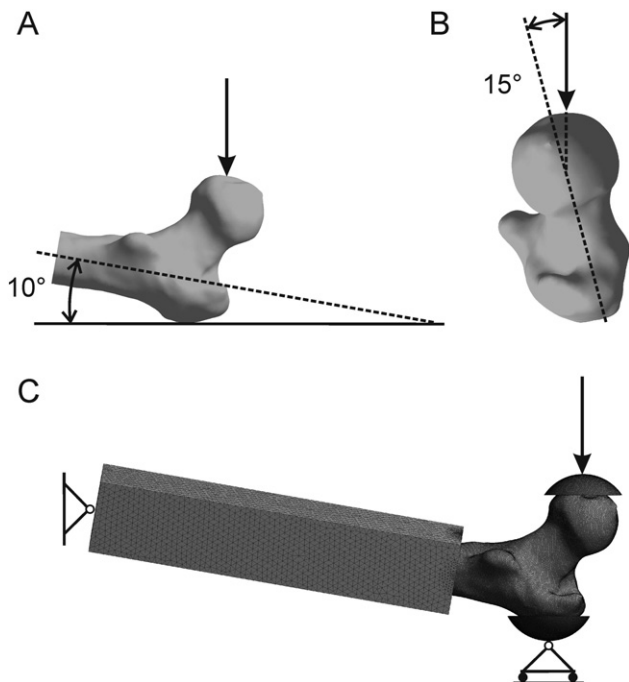

Fig. 2. Loading/falling angles (A & B) and boundary conditions of the FE model. The femoral shaft was tilted at 10° with respect to the ground (A) and the femoral neck was internally rotated by 15° (B). Force was applied to the whole upper face of the head-protecting cap, at a described angle. A 200 mm long aluminum pot was placed at 15–20 mm below the most projected part of the lesser trochanter of each proximal femur. A hinge-type constraining boundary condition was applied to nodes of the distal face of the aluminum pot. This allowed nodes at the hinge-axis to freely rotate in the quasi-frontal plane, while all other degrees of freedom were constrained. Greater trochanter cap's surface nodes were restrained in the direction of the force (C).

To simulate sideways falling, the most commonly used force direction from previous experimental studies [10,32,33] was chosen. The femoral shaft was tilted at 10° with respect to the ground and the femoral neck was internally rotated by 15° (Fig. 2) [10,32,33]. The individual impact force was estimated using the equation proposed by Bouxsein et al. [34]:

$$F_{peak} = \sqrt{2gh_{cg}KM},$$

where g is the gravitational constant (9.81 m/s^2), h_{cg} is the height of the center of gravity of the body assumed as $0.51 \times$ height (m), K is the stiffness constant (71 kN/m), and M is the effective mass calculated by ($^7/_{20} \times$ total body mass).

The force described above was then applied to the entire upper face of the femoral head cap at a defined angle while the trochanter cap was restrained in the direction of the force (Fig. 2) [22]. The femoral head and trochanter caps covered a depth of 5 mm of the femoral head and the lateral side of the trochanter [6]. The distal pot was placed at 15–20 mm below the most projected part of the lesser trochanter of each proximal femur. The distance between the most proximal part of the proximal femur to the distal part of the aluminum pot was in the range of 280–306 mm and was similar to the previous study [35]. A hinge-type restraining BC was applied to the distal side of the aluminum pot. This allowed nodes at the hinge-axis to freely rotate in the quasi-frontal plane, while all other degrees of freedom were constrained [22, 28].

2.4. FE derived stress within the femoral neck cortical bone

From each FE model, the nodal cortical von Mises stresses were calculated for the entire femoral neck region. These von Mises stresses were imported into MATLAB for further post-FE analysis. The entire femoral neck region was first divided into three sub-volumes along the femoral neck axis: proximal, middle, and distal volumes. For clarity, these sub-volumes are henceforth referred to as proximal, middle, and distal sites (Fig. 1). This division was performed so that the length of the most superior surface was equal for each site. Next, these three sites were divided into equal 45° octant regions each representing different anatomic directions of the respective cross-section of the femoral neck. This octant division was performed similar to previous studies [4, 17,36,37] except that the femoral neck axis was used as a reference for the center of the octant instead of the geometric centroid. In the present study, the femoral neck axis was defined similar to a previous study [38] so that it goes through the center of the femoral head and the geometric center of the thinnest femoral neck cross-section. The center of the femoral head was identified as the center of the sphere that best fitted the periosteal surface. The octants were anatomically defined as inferior (I), inferoanterior (IA), anterior (A), superoanterior (SA), superior (S), superoposterior (SP), posterior (P), and inferoposterior region (IP) (Fig. 1). For each individual proximal femur FE model, the mean cortical von Mises stresses in each octant (*octant cortical stress*) were calculated for all three sites.

2.5. Statistical analysis

Statistical analyses were performed with SPSS 22.0 (IBM Corp., Armonk, NY, USA). Mean and SD were given as descriptive statistics. Differences in octant cortical stresses in the three sites between each exercise group and the control group were estimated by multivariable analysis of covariance (MANCOVA) using the individual impact force as a covariate. Exercise groups were not compared to each other. Sidak correction was used to control for multiple comparisons in the post-hoc tests. Logarithmic transformations of the octant cortical stresses were performed prior to MANCOVA to control skewness of the data. Percentage differences of the octant cortical stress between each

exercise loading group and control group were calculated by taking anti-log of the impact force-adjusted mean octant cortical stress. A p value of <0.05 was considered statistically significant.

3. Results

3.1. Descriptive data of participants

Table 1 shows the descriptive data of age, sport-specific training hours/week, training sessions/week, duration of competitive career, height, body weight (BW), and estimated impact force in each exercise loading and control group. Further details of body composition and muscular performance have been reported previously [17]. In addition to a competitive career of >8 years, athletic participants clearly had much longer training hours and more training sessions per week compared with the non-competitive habitually active control participants.

3.2. Octant cortical stresses in general

Fig. 3 shows the unadjusted mean octant cortical stresses for proximal, middle, and distal femoral neck sites for each group. At the proximal site, higher stress levels were generally observed in the inferior and inferoposterior regions, while at the middle site higher stress levels were generally evident in the superior, superoposterior, and posterior regions. At the distal site, higher stresses were generally observed in the posterior region and became prominent in the superoposterior region. Fig. 4 presents example subjects from each group of the study population to illustrate typical stress distributions in each group. Stresses higher than 185 MPa were observed in the region spanning the superoposterior and posterior part of the femoral neck. Notably, a large contiguous area of >185 MPa stresses can be seen in the stress distributions of the repetitive non-impact group (R-NI) and the control proximal femora. Table 2 shows the impact force-adjusted mean percentage differences in octant cortical stresses for the proximal, middle, and distal femoral neck sites between each exercise loading group and the control group.

3.2.1. Proximal octant stress

The high-impact (H-I) group had significantly lower octant stresses ($p < 0.05$) than in the control group in the inferior (21%), inferoanterior (29%), superoanterior (9%), superoposterior (12%), posterior (15%), and inferoposterior (17%) octants. The odd-impact (O-I) group had significantly lower stresses in the superoposterior (14%) and posterior (12%) octants. The high-magnitude (H-M) group had significantly lower stresses in the superoposterior (16%) and posterior (12%) octants. The repetitive-impact (R-I) group had significantly lower stresses in the inferior (14%), inferoanterior (19%), anterior (16%), superoanterior (13%), superior (12%), superoposterior (21%), posterior (22%), and inferoposterior (15%) octants.

3.2.2. Middle octant stress

The H-I group had significantly lower octant stresses ($p < 0.05$) than in the control group in the inferior (32%), inferoanterior (29%), anterior (16%), superoposterior (10%), posterior (19%), and inferoposterior

(25%) octants. The O-I group had significantly lower stresses in the inferior (17%), inferoanterior (17%), anterior (14%), superoanterior (14%), superior (16%), superoposterior (16%), and posterior (12%) octants. The H-M group had significantly lower stresses in the superior (13%) and superoposterior (15%) octants. The R-I group had significantly lower stresses in the inferior (20%), inferoanterior (21%), anterior (18%), superoanterior (13%), superior (14%), superoposterior (23%), posterior (22%), and inferoposterior (17%) octants. Also, a trend for lower stresses when compared to controls was observed in the H-I group in the superoanterior ($p = 0.07$, 11%) octant.

3.2.3. Distal octant stress

The H-I group had significantly lower octant stresses ($p < 0.05$) than in the control group in the inferior (24%), inferoanterior (18%), superoposterior (13%), posterior (22%), and inferoposterior (22%) octants. The O-I group had significantly lower stresses in the inferior (16%), inferoanterior (13%), and superoposterior (14%) octants. The R-I group had significant lower stresses in the inferior (17%), inferoanterior (17%), anterior (18%), superoanterior (18%), superoposterior (19%), posterior (20%), and inferoposterior (16%) octants. Also, trends for lower stresses when compared to controls were observed in the H-I group in the anterior ($p = 0.06$, 15%) and superoanterior ($p = 0.06$, 16%) octants. In the O-I group, trends for lower stresses were observed in the superoanterior ($p = 0.08$, 14%) and posterior ($p = 0.07$, 9%) octants. In the H-M group, similar trends were observed in the superoposterior ($p = 0.07$, 9%) octant and in the superior ($p = 0.08$, 17%) octant in the R-I group.

4. Discussion

In this large FE modeling study of female athletes, the association of specific exercise loading history with femoral neck structural strength in a sideways falling situation was elaborated. As expected from the findings of previous studies [6,7], high stresses were primarily distributed over the superolateral cortex region of the femoral neck: specifically, in the superior, superoposterior, and posterior octants at the middle site, and in the superoposterior and posterior octants at the distal sites. Present results suggest that exercise loading history during adolescences and early adulthood that involves either high impacts (H-I), impacts from unusual directions (O-I), a large number of repetitive impacts (R-I), or extreme muscle forces (H-M) is associated with significantly lower (10–23%) fall-induced stresses at these vulnerable femoral neck regions (the five octants listed above) when compared to the control group. Importantly, the highest octant stresses were observed in the fracture-prone posterior part of the superolateral cortex region (superoposterior octant in the distal site in Fig. 1 and Fig. 3), which is in agreement with the findings of a study by Mayhew et al. [4]. We found that the femoral neck in the H-I, the O-I, and the R-I groups experienced significantly lower (13–19%) stress in this octant compared to the control group. Although a significant difference was not observed, the H-M group exhibited a trend for lower stress ($p = 0.07$, 9%) in the same octant. These results may translate into a reduced risk of hip fractures caused by falling.

The present findings are largely explained by the specific structural adaptation of the cortical bone to impact loading. Previously, Nikander

Table 1
Group characteristics.

| Group	n	Age (years)	Sport-specific training hours/week	Training sessions/week	Competing career (years)	Height (cm)	Weight (kg)	Impact force (N)
H-I	19	22.3 (4.1)	11.5 (2.3)	6.7 (1.4)	10.1 (3.4)	174 (6)	60.2 (5.4)	5102.1 (268.3)
O-I	19	25.3 (6.7)	9.3 (2.7)	5.7 (1.4)	9.6 (4.8)	165 (8)	60.8 (8.3)	4991.0 (450.5)
H-M	17	27.5 (6.3)	9.1 (2.7)	5.8 (2.0)	8.0 (4.7)	158 (3)	63.3 (13.2)	4974.0 (531.9)
R-I	18	28.9 (5.6)	10.9 (3.4)	8.7 (2.1)	12.4 (6.7)	168 (5)	53.7 (3.4)	4737.8 (198.2)
R-NI	18	19.7 (2.4)	19.9 (4.5)	11.4 (2.0)	9.1 (2.6)	173 (5)	65.1 (5.6)	5284.7 (251.1)
Control	20	23.7 (3.8)	2.8 (0.9)	2.8 (1.0)	–	164 (5)	60.0 (7.4)	4943.5 (363.6)

Mean and (SD).
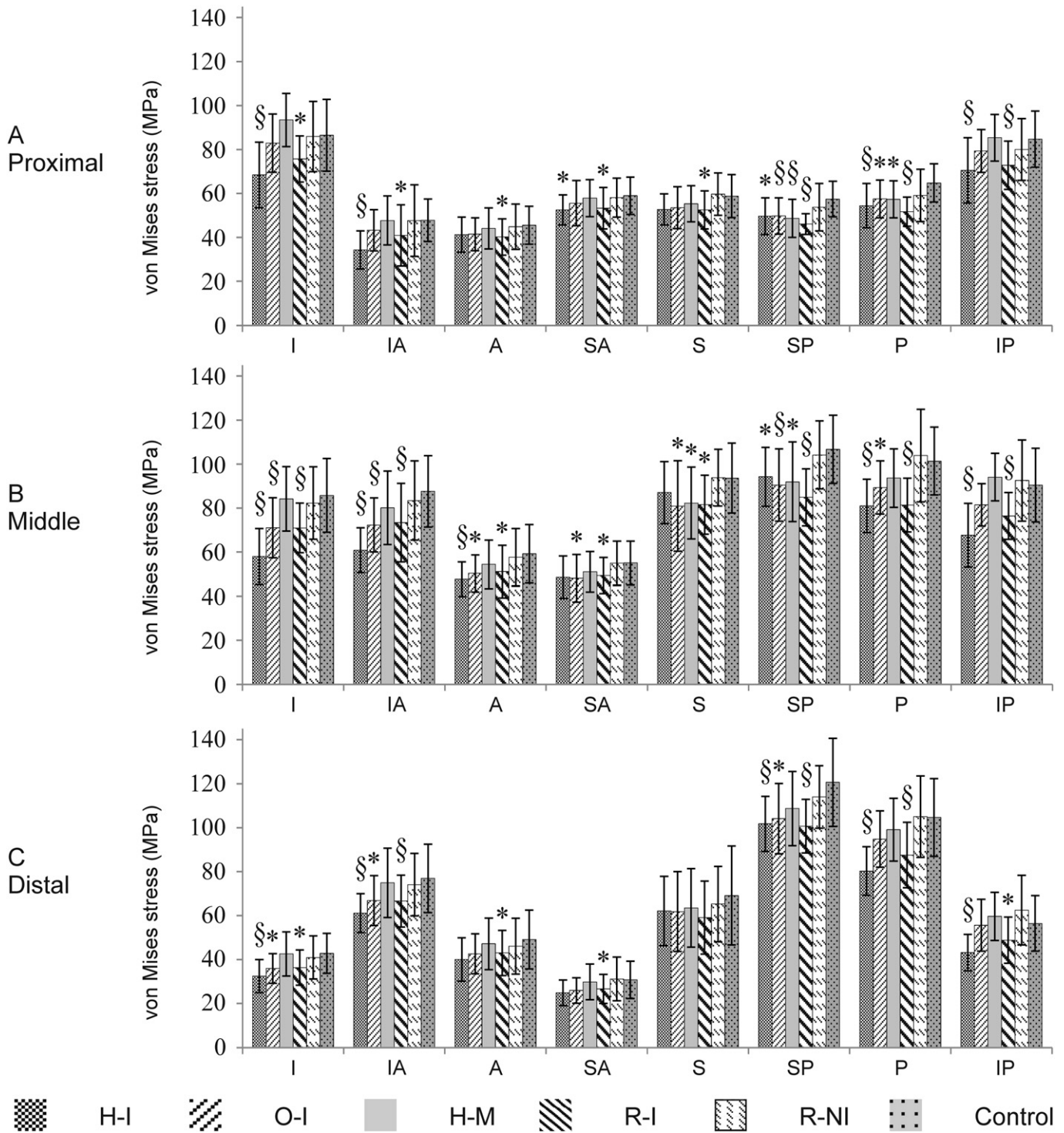
Fig. 3. Group unadjusted mean (SD) octant cortical stress at the proximal, middle, and distal sites of the femoral neck (see Fig. 1). Each bar represents each group's unadjusted mean octant stress with SD. According to the MANCOVA, * and § show the statistical significance of $0.01 \leq p < 0.05$ and $p < 0.01$ respectively.

et al. [17] found that the femoral neck of athletes in the H-I group had a thicker cortex in the inferior, anterior, and posterior quadrants, while the O-I group had a consistently thicker cortex in the anterior, posterior, and superior quadrants of the femoral neck. Notably, the lower stresses in the inferior, inferoanterior, and inferoposterior octant regions in the H-I group can be attributed to a very thick inferior cortex: approximately 60% thicker than in the habitually active control group [17].

A particularly interesting finding in the present study was that the femoral neck in the R-I (endurance runners) group also showed significant and similar low stresses to those observed in the H-I group.

Previously, Nikander et al. [17] reported that the cortical bone of the femoral neck in the R-I group was not thicker than in the control group. This indicates that the lower stresses in the R-I may be attributed to other geometrical factors, that is, the more circular shape of the femoral neck cross-section shown by Narra et al. [39]. Basically, a more circular bone is mechanically more robust in all directions than an oval shaped bone. Sievänen et al. [40] observed that physically more active medieval people had a more circular femoral neck cross-section in contrast to present-day people who have a more oval-shaped cross-section. It was estimated that the oval-shaped femoral neck of present-day people may experience 1.3–
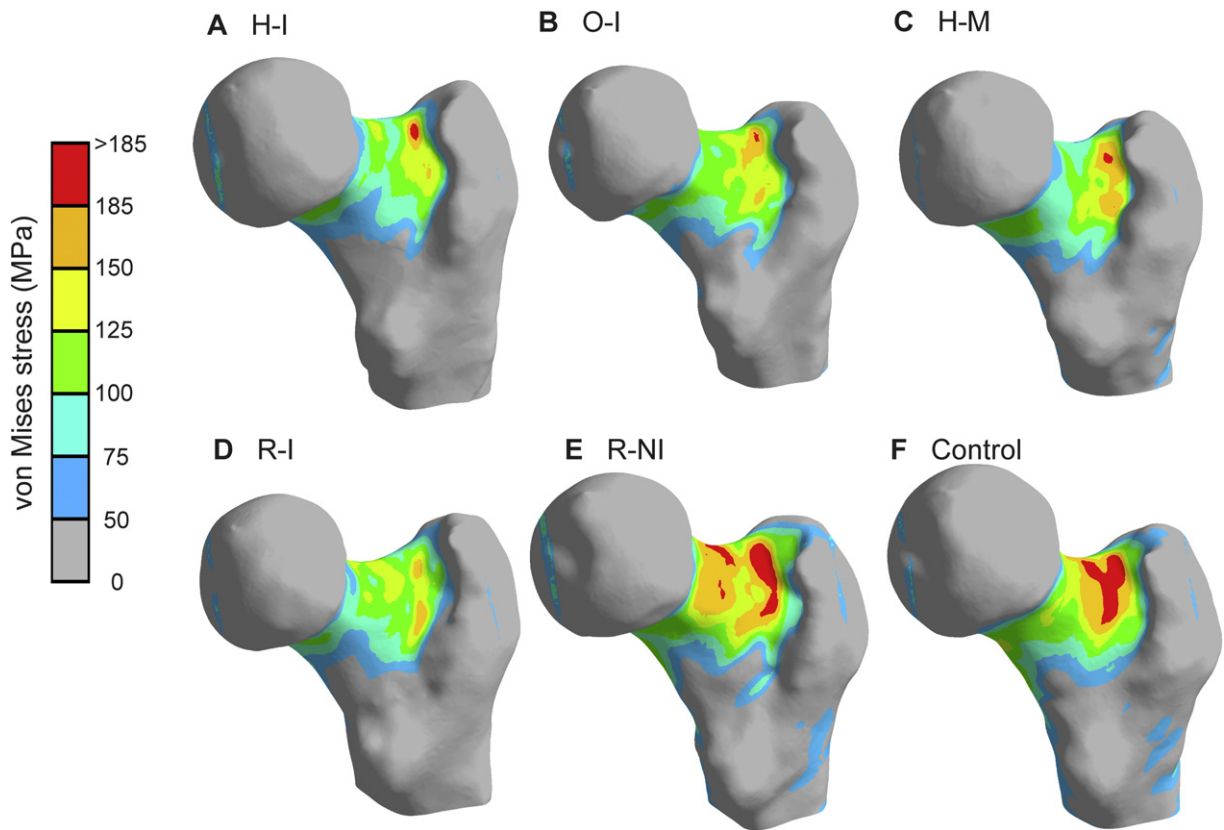
Fig. 4. Examples of typical von Mises stress distribution from each group. A, B, C, D, E, and F show an example stress distribution from the H-I, O-I, H-M, R-I, R-NI, and control groups, respectively.

1.5 times higher fall-induced stress in a sideways fall than the circular femoral neck of the medieval people [40]. This estimation is consistent with the results of the present study that show almost 20% lower stress in the R-I group than in the control group. Running (or walking) is a natural form of locomotion and a common type of exercise. In particular, the human skeleton is particularly fitted for endurance running [41], but as alluring as the present finding is from the evolutionary point of view, the beneficial results in the endurance running group remain at best speculative and warrant further elaboration.

The R-NI group showed no apparent reduction in stress at any femoral neck octant. This agrees with the findings by Nikander et al. [17] that showed no exercise-related benefit to the cortical geometry among swimmers. The typical movements in swimming require a lot of repetitive muscle contractions and can be intensive, but they are also smooth and without impacts. The H-M group, in turn, showed less reduced octant stresses compared to the control group than the H-I, O-I, and R-I groups did in spite of extreme muscle forces involved in power-lifting (e.g., a squat). Again, this is likely attributable to the inherent nature of movement. During H-M exercises, the movement is slow by nature, and therefore its rate of loading is low.

Moderate to high ground reaction forces and a high rate of force development due to the ground impact are common factors in exercise loading that seem to be beneficial for femoral neck strength. Peak vertical ground reaction forces are 12–20 times BW [42,43] for H-I exercise, 2.5–3.5 times BW [44–46] for O-I exercise, 2–3 times BW [47] for H-M exercise (squat), and 2–2.5 times BW [48,49] for R-I exercise while the estimated impact loading rates (BW s^{-1}) are about 400–480 BW s^{-1} [42], 20–180 BW s^{-1} [44,45], 5–6 BW s^{-1} [47], and 60–150 BW s^{-1} [48–50], respectively. In swimming, peak reaction force and loading rate at the push-off phase of turning are estimated to be <1.5 times BW [51,52] and <10 BW s^{-1} [51], respectively. Such a combination of reaction force and loading rate in the R-NI exercise seems to be insufficient to improve

femoral neck strength. While ground reaction force in the H-M exercise may be similar in magnitude to those in the O-I and R-I exercises, the rate of force development is significantly lower. In light of the results for the H-M group, this indicates that in spite of the moderate-to-high ground reaction force, the stimulus for beneficial geometric adaptation seems to be diminished by the lower rate of loading. Differing from power-lifting (squat, bench press, and deadlift), weightlifting movements such as the snatch, clean, and jerk are explosive and involve more impact: peak vertical ground reaction forces are 2.5–4 times BW and estimated impact loading rates vary from about 10–50 BW s^{-1} [53–56]. This warrants further investigation of femoral neck strength among weightlifters.

The mean starting ages of the competitive careers of the athletic participants were the following: H-I = 12.2 years; O-I = 15.7 years; H-M 19.5 years; R-I = 16.5 years; R-NI = 10.6 yrs. Accordingly, the H-M group started their sport-specific career the latest of any groups and their careers were also the shortest (mean 8 years) at the time of the study. The H-I group started their career at the age of 12.2 years, which is 7 years earlier than that of the H-M group. Indeed, the starting age of 19.5 years of the H-M group is almost close to skeletal maturity [57]. It is well established that starting the exercise training in early adolescence is the most beneficial for bone strength compared with a later start of training [58]. Lorentzon et al. [59] reported that higher aBMD, cortical bone size, and trabecular density were observed among those who started their training career before the age of 13 than those who started their training later. Further, the duration of the training in adolescence is associated with improved bone traits as well [59,60]. This being the case, the odds of finding a clear exercise-related reduction in fall-induced stress in the H-M group may have been attenuated. However, it is worth noting that starting intensive power-lifting exercises (squat, bench press, and deadlift) at an early age is not recommended, which may explain the later starting age in the H-M group. On the

Table 2
Impact force-adjusted mean percentage differences (95% CI) in octant cortical stresses for proximal, middle, and distal sites between each exercise group and control group.

	Proximal	Middle	Distal		Proximal	Middle	Distal
Inferior (I)				*Superior (S)*			
H-I	**−20.6** (−28.6 to −11.8)	**−32.2** (−39.1 to −24.6)	**−23.6** (−31.5 to −15.0)	H-I	**−8.2** (−14.5 to −1.2)	−5.8 (−12.9 to 1.8)	−6.2 (−18.6 to 7.8)
O-I	−3.4 (−11.5 to 5.7)	**−16.6** (−24.2 to −8.3)	**−15.7** (−23.4 to −7.3)	O-I	**−8.8** (−16.0 to −1.1)	**−15.5** (−23.5 to −6.7)	−9.6 (−22.1 to 4.6)
H-M	**9.4** (0.2 to 19.5)	−1.1 (−10.6 to 9.4)	−1.1 (−12.1 to 11.1)	H-M	−5.8 (−13.2 to 2.2)	**−12.5** (−20.1 to −4.0)	−6.9 (−20.2 to 8.7)
R-I	**−13.5** (−20.8 to −5.5)	**−20.0** (−27.1 to −12.4)	**−17.0** (−25.3 to −7.8)	R-I	**−12.3** (−19.5 to −4.6)	**−13.9** (−20.8 to −6.5)	**−17.0** (−28.4 to −3.7)
R-NI	−0.2 (−10.3 to 10.8)	−3.2 (−13.6 to 8.7)	−4.3 (−14.9 to 7.7)	R-NI	0.5 (−8.0 to 9.5)	0.5 (−7.5 to 9.1)	2.6 (−12.2 to 19.8)
InferoAnterior (IA)				*SuperoPosterior (SP)*			
H-I	**−28.6** (−36.1 to −19.9)	**−29.4** (−35.1 to −23.0)	**−18.0** (−24.2 to −11.1)	H-I	**−11.9** (−17.9 to −5.3)	**−9.8** (−15.5 to −3.6)	**−12.9** (−18.6 to −6.9)
O-I	−9.2 (−18.1 to 0.5)	**−17.2** (−24.1 to −9.8)	**−12.9** (−20.3 to −4.7)	O-I	**−13.5** (−19.6 to −7.1)	**−16.1** (−22.6 to −8.8)	**−13.5** (−20.0 to −6.4)
H-M	−0.9 (−11.5 to 10.8)	−8.8 (−17.3 to 0.6)	−2.7 (−12.1 to 7.9)	H-M	**−15.7** (−22.2 to −8.6)	**−14.5** (−21.5 to −6.9)	**−9.4** (−16.3 to −2.1)
R-I	**−18.5** (−29.3 to −6.4)	**−20.6** (−28.1 to −12.1)	**−16.8** (−23.9 to −9.0)	R-I	**−20.7** (−25.5 to −15.5)	**−22.6** (−27.9 to −16.7)	**−19.3** (−24.6 to −13.8)
R-NI	−7.5 (−20.7 to 7.8)	−4.3 (−14.2 to 6.8)	−0.9 (−10.4 to 9.8)	R-NI	−6.2 (−14.1 to 2.2)	−0.5 (−7.7 to 7.3)	−0.5 (−7.5 to 7.3)
Anterior (A)				*Posterior (P)*			
H-I	−6.0 (−13.9 to 2.8)	**−16.2** (−23.5 to −8.4)	**−14.7** (−24.2 to −4.0)	H-I	**−14.7** (−20.9 to −8.1)	**−19.3** (−25.0 to −13.2)	**−21.5** (−26.8 to −15.6)
O-I	−8.6 (−16.5 to 0.1)	**−14.3** (−21.9 to −5.7)	**−12.5** (−22.2 to −1.5)	O-I	**−11.5** (−17.0 to −5.4)	**−11.7** (−17.8 to −5.3)	**−9.0** (−15.3 to −2.0)
H-M	−2.9 (−12.2 to 7.2)	−7.3 (−16.4 to 2.7)	−3.2 (−14.6 to 9.9)	H-M	**−11.7** (−17.4 to −5.5)	**−7.5** (−14.0 to −0.3)	−4.7 (−12.0 to 3.2)
R-I	**−15.5** (−23.5 to −6.6)	**−18.0** (−26.3 to −8.7)	**−18.2** (−27.0 to −8.1)	R-I	**−21.8** (−26.8 to −16.6)	**−21.5** (−27.1 to −15.5)	**−20.0** (−25.9 to −13.5)
R-NI	1.2 (−9.4 to 12.9)	1.6 (−9.8 to 14.3)	−0.9 (−14.2 to 14.2)	R-NI	−8.0 (−15.2 to 0.1)	1.4 (−7.5 to 11.0)	3.3 (−5.6 to 12.8)
SuperoAnterior (SA)				*InferoPosterior (IP)*			
H-I	**−9.0** (−15.0 to −2.8)	−11.3 (−19.2 to 2.6)	**−15.7** (−25.6 to −4.5)	H-I	**−16.6** (−24.0 to −8.6)	**−25.4** (−32.6 to −17.3)	**−22.2** (−29.9 to −13.4)
O-I	−6.2 (−13.6 to 1.5)	**−13.5** (−21.6 to −4.7)	**−14.1** (−23.7 to −3.0)	O-I	−6.0 (−12.1 to 0.6)	**−8.6** (−15.7 to −1.1)	−0.2 (−10.4 to 10.9)
H-M	−1.8 (−8.8 to 5.9)	−6.9 (−15.2 to 2.1)	−2.1 (−14.6 to 12.2)	H-M	1.2 (−5.8 to 8.6)	5.4 (−3.3 to 14.8)	6.7 (−4.7 to 19.5)
R-I	**−13.3** (−20.0 to −6.0)	**−12.7** (−20.2 to −4.7)	**−17.6** (−27.5 to −6.5)	R-I	**−15.3** (−21.5 to −8.6)	**−17.0** (−24.0 to −9.5)	**−15.9** (−24.7 to −5.8)
R-NI	−0.5 (−7.9 to 7.7)	0.9 (−9.0 to 11.7)	4.2 (−11.7 to 22.9)	R-NI	−5.8 (−13.7 to 2.7)	0.7 (−9.5 to 12.3)	9.4 (−3.9 to 24.5)

Statistically significant *p* values (*p* < 0.05) based on MANCOVA are shown in bold.

other hand, it is likely that the H-M group was involved in various, less specific exercise training during adolescence.

Observed reductions in the octant stress (10–30%) along the femoral neck in the sideways falling situation, attributable to exercise-induced structural adaptations, may be clinically important. It is noteworthy that the control group was comprised of young healthy women who did recreational exercises 2–3 times a week. Thus, our control participants were physically active, but not athletes. This being the case, it is possible that actual exercise-induced benefit in the femoral neck strength in sideways falling could be even higher when compared with the average, less physically active population.

As to the clinical relevance of the present results, caution is needed. Since the data were obtained from young female athletes, the results cannot be extrapolated to the general population. Despite the clear benefits, H-I exercise does not provide a panacea against hip fragility and fractures. Extreme impact forces (12–20 times BW) [42,43] in the H-I exercises are obviously too risky not only for older people but also for sedentary people regardless of age. Since the O-I and R-I exercises produce moderate impacts, the risk of musculoskeletal injuries remains lower. Thus, exercise involving impacts from unusual directions and a large number of repeated impacts may offer a more feasible and equally effective option to increase femoral neck strength. For the young, physically active, and/or fit

people, not only O-I and R-I exercises but also appropriate H-I exercises are feasible in order to maintain and/or increase femoral neck strength. It is worth mentioning that along with O-I and R-I exercises (e.g. jogging), H-M exercises (squat, deadlift, etc.) may also be beneficial for the overall health of the proximal femur for people with a sedentary background or the elderly. This is, of course, contingent on the people having no preexisting musculoskeletal maladies, having sufficient mobility, and weights being chosen according to their physical conditioning.

Another important question is whether the exercise-induced skeletal benefits from early adulthood can be sustained into old age. It is known that the exercise-induced bone thickening during growth occurs through new bone formation on the periosteal bone surface, while the age-related bone loss takes place at the endocortical bone surface [2]. Should the femoral neck cortical bone be thicker during young adulthood, it may be more resistant against fractures in old age. It is noteworthy that retired ice hockey and soccer players > 60 years old have lower fracture risk compared to matched controls despite some loss in exercise-induced high aBMD due to retirement from sports [61]. This finding indicates that the exercise-induced structural benefits to the femoral neck during young adulthood may be sustained into old age and highlights the importance of exercise in adolescence and young adulthood in terms of preventing future hip fractures. Further, the effect of exercise on bone may vary

depending on the period of life. During adolescence, exercise can increase bone strength, and continued exercise may help maintain exercise-induced bone strength in adulthood. Moreover, exercise may attenuate a decrease in bone strength due to age-related bone loss [60].

The major strength of the present study is the large total sample size of 111 individual FE models that represent a variety of distinct exercise loading histories. This makes the present study one of the largest proximal femur FE modeling studies. Further, the large total sample size made it possible to divide the athletes into smaller subgroups, which enabled us to investigate the association of the distinct exercise loading pattern with femoral neck strength in a sideways falling situation. However, the marginal differences in the H-M group, despite group-differences of a similar magnitude, indicate limited statistical power in some subgroup analyses.

In addition to somewhat limited statistical power, there are other limitations as well. The main limitation was the use of the MR images for the construction of the proximal femur geometry which was not validated against actual mechanical testing. While QCT would have provided high-resolution image data on femoral neck geometry and bone apparent density, MR imaging has been found to be adequately valid for the assessment of cortical geometry [25,62]. The pixel size in the previous QCT-based proximal femur studies [13,19,20] has been around 0.5 mm in contrast to the 0.9 mm pixel size in the present study. Obviously, a higher in-plane resolution would have provided a more accurate segmentation of the cortical bone. Therefore, to comply with valid QCT-based proximal femur FE modeling studies, we adopted similar BCs and loading conditions [22,28]. In the present study, however, trabecular bone was modeled as a non-porous homogeneous structure in contrast to its actual non-uniform structure [63], which could cause <10% error in the maximum stress reported in the literature [19]. However, according to Koivumäki et al., inclusion of the trabecular bone in the sideways falling FE models may not play a crucial role, and the proximal femoral strength can be evaluated with reasonable accuracy using a cortical bone FE model only [64]. Further, Holzer et al. [65] reported that the complete removal of the trabecular bone led to a relatively small reduction in bone strength while the cortical bone is primarily responsible for load bearing and transmitting forces. Indeed, the present study mainly focused on evaluating the influence of cortical geometry on the stress distribution in the simulated sideways fall while modeling the trabecular bone as non-porous homogeneous material in every individual model. While the use of QCT-based FE models would have also allowed the estimation of inhomogeneous elastic properties using the voxel-based Hounsfield unit data (density) [11–13,18–22], the assumption of homogeneous material properties is acceptable. Taddei et al. [19] compared the homogeneous proximal femur bone model with the inhomogeneous model and found only a marginal improvement in accuracy of prediction; R^2 between FE predicted stress and experimental stress was 0.91 for the inhomogeneous model and 0.89 for the homogeneous model. Finally, exposing fertile young adult women to ionizing radiation from QCT for non-diagnostic purposes would have been ethically unacceptable.

5. Conclusion

The present FE study is the first study that employed a large number of individual 3D proximal femur FE models obtained from young adult female athletes representing distinct exercise loading patterns. The results showed that the athletes with a history of impact exercises from endurance running induced repetitive impacts, soccer and squash induced odd direction impact, to extreme vertical jumping sports showed clinically relevant lower stresses at the fracture prone regions of the femoral neck in a sideways falling simulation. In addition to impacts, high magnitude strength training may also be beneficial for maintaining the robustness of the femoral neck. This requires further study, however. The results of this study also give new insights into the prevention of hip fragility with targeted exercises.

Disclosures

All authors state that they have no conflicts of interest.

Authorship

All authors contributed to the study design. NN, RN, JH, and HS were responsible for the data collection. Modeling and simulation were performed by SA and supervised by JH and RK. Data analysis was performed by SA, NN, RN, RK, and HS. The manuscript was drafted by SA and HS. All authors are responsible for revising and approving the final version of manuscript. SA takes responsibility for the integrity of the data analysis.

References

[1] H.M. Frost, Bone's mechanostat: a 2003 update, Anat. Rec. A. Discov. Mol. Cell Evol. Biol. 275 (2003) 1081–1101.
[2] C. Ruff, B. Holt, E. Trinkaus, Who's afraid of the big bad Wolff?: "Wolff's law" and bone functional adaptation, Am. J. Phys. Anthropol. 129 (2006) 484–498.
[3] J.C. Lotz, E.J. Cheal, W.C. Hayes, Stress distributions within the proximal femur during gait and falls: implications for osteoporotic fracture, Osteoporos. Int. 5 (1995) 252–261.
[4] P.M. Mayhew, C.D. Thomas, J.G. Clement, N. Loveridge, T.J. Beck, W. Bonfield, C.J. Burgoyne, J. Reeve, Relation between age, femoral neck cortical stability, and hip fracture risk, Lancet 366 (2005) 129–135.
[5] K.E. Poole, P.M. Mayhew, C.M. Rose, J.K. Brown, P.J. Bearcroft, N. Loveridge, J. Reeve, Changing structure of the femoral neck across the adult female lifespan, J. Bone Miner. Res. 25 (2010) 482–491.
[6] E. Verhulp, B. van Rietbergen, R. Huiskes, Load distribution in the healthy and osteoporotic human proximal femur during a fall to the side, Bone 42 (2008) 30–35.
[7] P.M. de Bakker, S.L. Manske, V. Ebacher, T.R. Oxland, P.A. Cripton, P. Guy, During sideways falls proximal femur fractures initiate in the superolateral cortex: evidence from high-speed video of simulated fractures, J. Biomech. 42 (2009) 1917–1925.
[8] R.D. Carpenter, G.S. Beaupré, T.F. Lang, E.S. Orwoll, D.R. Carter, New QCT analysis approach shows the importance of fall orientation on femoral neck strength, J. Bone Miner. Res. 20 (2005) 1533–1542.
[9] C.M. Ford, T.M. Keaveny, W.C. Hayes, The effect of impact direction on the structural capacity of the proximal femur during falls, J. Bone Miner. Res. 11 (1996) 377–383.
[10] T.P. Pinilla, K.C. Boardman, M.L. Bouxsein, E.R. Myers, W.C. Hayes, Impact direction from a fall influences the failure load of the proximal femur as much as age-related bone loss, Calcif. Tissue Int. 58 (1996) 231–235.
[11] J.H. Keyak, S.A. Rossi, K.A. Jones, H.B. Skinner, Prediction of femoral fracture load using automated finite element modeling, J. Biomech. 31 (1997) 125–133.
[12] J.H. Keyak, H.B. Skinner, J.A. Fleming, Effect of force direction on femoral fracture load for two types of loading conditions, J. Orthop. Res. 19 (2001) 539–544.
[13] M. Bessho, I. Ohnishi, T. Matsumoto, S. Ohashi, J. Matsuyama, K. Tobita, M. Kaneko, K. Nakamura, Prediction of proximal femur strength using a CT-based nonlinear finite element method: differences in predicted fracture load and site with changing load and boundary conditions, Bone 45 (2009) 226–231.
[14] J.A. Grisso, J.L. Kelsey, B.L. Strom, G.Y. Chiu, G. Maislin, L.A. O'Brien, S. Hoffman, F. Kaplan, Risk factors for falls as a cause of hip fracture in women. The Northeast Hip Fracture Study Group, N. Engl. J. Med. 324 (1991) 1326–1331.
[15] J. Parkkari, P. Kannus, M. Palvanen, A. Natri, J. Vainio, H. Aho, I. Vuori, M. Järvinen, Majority of hip fractures occur as a result of a fall and impact on the greater trochanter of the femur: a prospective controlled hip fracture study with 206 consecutive patients, Calcif. Tissue Int. 65 (1999) 183–187.
[16] R. Nikander, H. Sievänen, A. Heinonen, P. Kannus, Femoral neck structure in adult female athletes subjected to different loading modalities, J. Bone Miner. Res. 20 (2005) 520–528.
[17] R. Nikander, P. Kannus, P. Dastidar, M. Hannula, L. Harrison, T. Cervinka, N.G. Narra, R. Aktour, T. Arola, H. Eskola, S. Soimakallio, A. Heinonen, J. Hyttinen, H. Sievänen, Targeted exercises against hip fragility, Osteoporos. Int. 20 (2009) 1321–1328.

[18] J.H. Keyak, S.A. Rossi, K.A. Jones, C.M. Les, H.B. Skinner, Prediction of fracture location in the proximal femur using finite element models, Med. Eng. Phys. 23 (2001) 657–664.

[19] F. Taddei, L. Cristofolini, S. Martelli, H.S. Gill, M. Viceconti, Subject-specific finite element models of long bones: an in vitro evaluation of the overall accuracy, J. Biomech. 39 (2006) 2457–2467.

[20] M. Bessho, I. Ohnishi, J. Matsuyama, T. Matsumoto, K. Imai, K. Nakamura, Prediction of strength and strain of the proximal femur by a CT-based finite element method, J. Biomech. 40 (2007) 1745–1753.

[21] Z. Yosibash, N. Trabelsi, C. Milgrom, Reliable simulations of the human proximal femur by high-order finite element analysis validated by experimental observations, J. Biomech. 40 (2007) 3688–3699.

[22] E. Schileo, L. Balistreri, L. Grassi, L. Cristofolini, F. Taddei, To what extent can linear finite element models of human femora predict failure under stance and fall loading configurations? J. Biomech. 47 (2014) 3531–3538.

[23] R. Nikander, H. Sievänen, K. Uusi-Rasi, A. Heinonen, P. Kannus, Loading modalities and bone structures at nonweight-bearing upper extremity and weight-bearing lower extremity: a pQCT study of adult female athletes, Bone 39 (2006) 886–894.

[24] P.A. Yushkevich, J. Piven, H.C. Hazlett, R.G. Smith, S. Ho, J.C. Gee, G. Gerig, User-guided 3D active contour segmentation of anatomical structures: significantly improved efficiency and reliability, NeuroImage 31 (2006) 1116–1128.

[25] H. Sievänen, T. Karstila, P. Apuli, P. Kannus, Magnetic resonance imaging of the femoral neck cortex, Acta Radiol. 48 (2007) 308–314.

[26] Q. Fang, D.A. Boas, Tetrahedral mesh generation from volumetric binary and gray-scale images, Proc. - 2009 IEEE Int. Symp. Biomed. Imaging From Nano to Macro, ISBI 2009IEEE 2009, pp. 1142–1145.

[27] G. Taubin, Curve and surface smoothing without shrinkageProc. - 1999 IEEE Int. Conf. Comput. Vis. 1995, pp. 852–857.

[28] B. Helgason, S. Gilchrist, O. Ariza, J.D. Chak, G. Zheng, R.P. Widmer, S.J. Ferguson, P. Guy, P.A. Cripton, Development of a balanced experimental-computational approach to understanding the mechanics of proximal femur fractures, Med. Eng. Phys. 36 (2014) 793–799.

[29] M. Lengsfeld, J. Kaminsky, B. Merz, R.P. Franke, Sensitivity of femoral strain pattern analyses to resultant and muscle forces at the hip joint, Med. Eng. Phys. 18 (1996) 70–78.

[30] G.N. Duda, M. Heller, J. Albinger, O. Schulz, E. Schneider, L. Claes, Influence of muscle forces on femoral strain distribution, J. Biomech. 31 (1998) 841–846.

[31] K. Polgár, H.S. Gill, M. Viceconti, D.W. Murray, J.J. O'Connor, Strain distribution within the human femur due to physiological and simplified loading: finite element analysis using the muscle standardized femur model, Proc. Inst. Mech. Eng. H. 217 (2003) 173–189.

[32] A.C. Courtney, E.F. Wachtel, E.R. Myers, W.C. Hayes, Effects of loading rate on strength of the proximal femur, Calcif. Tissue Int. 55 (1994) 53–58.

[33] A.C. Courtney, E.F. Wachtel, E.R. Myers, W.C. Hayes, Age-related reductions in the strength of the femur tested in a fall-loading configuration, J. Bone Joint Surg. Am. 77 (1995) 387–395.

[34] M.L. Bouxsein, P. Szulc, F. Munoz, E. Thrall, E. Sornay-Rendu, P.D. Delmas, Contribution of trochanteric soft tissues to fall force estimates, the factor of risk, and prediction of hip fracture risk, J. Bone Miner. Res. 22 (2007) 825–831.

[35] O. Ariza, S. Gilchrist, R.P. Widmer, P. Guy, S.J. Ferguson, P.A. Cripton, B. Helgason, Comparison of explicit finite element and mechanical simulation of the proximal femur during dynamic drop-tower testing, J. Biomech. 48 (2015) 224–232.

[36] S.L. Manske, T. Liu-Ambrose, D.M. Cooper, S. Kontulainen, P. Guy, B.B. Forster, H.A. McKay, Cortical and trabecular bone in the femoral neck both contribute to proximal femur failure load prediction, Osteoporos. Int. 20 (2009) 445–453.

[37] C.D. Thomas, P.M. Mayhew, J. Power, K.E. Poole, N. Loveridge, J.G. Clement, C.J. Burgoyne, J. Reeve, Femoral neck trabecular bone: loss with ageing and role in preventing fracture, J. Bone Miner. Res. 24 (2009) 1808–1818.

[38] J.D. Wilson, W. Eardley, S. Odak, A. Jennings, To what degree is digital imaging reliable? Validation of femoral neck shaft angle measurement in the era of picture archiving and communication systems, Br. J. Radiol. 84 (2011) 375–379.

[39] N. Narra, R. Nikander, J. Viik, J. Hyttinen, H. Sievänen, Femoral neck cross-sectional geometry and exercise loading, Clin. Physiol. Funct. Imaging 33 (2013) 258–266.

[40] H. Sievänen, L. Józsa, I. Pap, M. Järvinen, T.A. Järvinen, P. Kannus, T.L. Järvinen, Fragile external phenotype of modern human proximal femur in comparison with medieval bone, J. Bone Miner. Res. 22 (2007) 537–543.

[41] D.M. Bramble, D.E. Lieberman, Endurance running and the evolution of Homo, Nature 432 (2004) 345–352.

[42] M.R. Ramey, K.R. Williams, Ground reaction forces in the triple jump, Int. J. Sport. Biomech. 1 (1985) 233–239.

[43] A. Heinonen, H. Sievänen, H. Kyröläinen, J. Perttunen, P. Kannus, Mineral mass, size, and estimated mechanical strength of triple jumpers' lower limb, Bone 29 (2001) 279–285.

[44] N. Smith, R. Dyson, L. Janaway, Ground reaction force measures when running in soccer boots and soccer training shoes on a natural turf surface, Sport. Eng. 7 (2004) 159–167.

[45] M.K. Dayakidis, K. Boudolos, Ground reaction force data in functional ankle instability during two cutting movements, Clin. Biomech. 21 (2006) 405–411.

[46] K. Ball, Loading and performance of the support leg in kicking, J. Sci. Med. Sport 16 (2013) 455–459.

[47] P.A. Swinton, R. Lloyd, J.W. Keogh, I. Agouris, A.D. Stewart, A biomechanical comparison of the traditional squat, powerlifting squat, and box squat, J. Strength Cond. Res. 26 (2012) 1805–1816.

[48] C.F. Munro, D.I. Miller, A.J. Fuglevand, Ground reaction forces in running: a reexamination, J. Biomech. 20 (1987) 147–155.

[49] S. Logan, I. Hunter, J.T. Hopkins, J.B. Feland, A.C. Parcell, Ground reaction force differences between running shoes, racing flats, and distance spikes in runners, J. Sport. Sci. Med. 9 (2010) 147–153.

[50] B. Kluitenberg, S.W. Bredeweg, S. Zijlstra, W. Zijlstra, I. Buist, Comparison of vertical ground reaction forces during overground and treadmill running. A validation study, BMC Musculoskelet. Disord. 13 (2012) 235.

[51] A.D. Lyttle, B.A. Blanksby, B.C. Elliott, D.G. Lloyd, Investigating kinetics in the free-style flip turn push-off, J. Appl. Biomech. 15 (1999) 242–252.

[52] B.A. Blanksby, D.G. Gathercole, R.N. Marshall, Force plate and video analysis of the tumble turn by age-group swimmers, J. Swim. Res. 11 (1996) 40–45.

[53] P. Comfort, M. Allen, P. Graham-Smith, Comparisons of peak ground reaction force and rate of force development during variations of the power clean, J. Strength Cond. Res. 25 (2011) 1235–1239.

[54] P. Comfort, M. Allen, P. Graham-Smith, Kinetic comparisons during variations of the power clean, J. Strength Cond. Res. 25 (2011) 3269–3273.

[55] W. Baumann, V. Gross, K. Quade, P. Galbierz, A. Schvvirtz, The snatch technique of world class weightlifters at the 1985 World Championships, Int. J. Sport Biomech. 4 (1988) 68–89.

[56] M.A. Lauder, J.P. Lake, Biomechanical comparison of unilateral and bilateral power snatch lifts, J. Strength Cond. Res. 22 (2008) 653–660.

[57] H. Haapasalo, P. Kannus, H. Sievänen, M. Pasanen, K. Uusi-Rasi, A. Heinonen, P. Oja, I. Vuori, Development of mass, density, and estimated mechanical characteristics of bones in Caucasian females, J. Bone Miner. Res. 11 (1996) 1751–1760.

[58] P. Kannus, H. Haapasalo, M. Sankelo, H. Sievänen, M. Pasanen, A. Heinonen, P. Oja, I. Vuori, Effect of starting age of physical activity on bone mass in the dominant arm of tennis and squash players, Ann. Intern. Med. 123 (1995) 27–31, http://dx.doi.org/10.7326/0003-4819-123-1-199507010-00003.

[59] M. Lorentzon, D. Mellström, C. Ohlsson, Association of amount of physical activity with cortical bone size and trabecular volumetric BMD in young adult men: the GOOD study, J. Bone Miner. Res. 20 (2005) 1936–1943.

[60] C.A. Boreham, H.A. McKay, Physical activity in childhood and bone health, Br. J. Sports Med. 45 (2011) 877–879.

[61] A. Nordström, C. Karlsson, F. Nyquist, T. Olsson, P. Nordström, M. Karlsson, Bone loss and fracture risk after reduced physical activity, J. Bone Miner. Res. 20 (2005) 202–207.

[62] B.R. Gomberg, P.K. Saha, F.W. Wehrli, Method for cortical bone structural analysis from magnetic resonance images, Acad. Radiol. 12 (2005) 1320–1332.

[63] A.G. Robling, A.B. Castillo, C.H. Turner, Biomechanical and molecular regulation of bone remodeling, Annu. Rev. Biomed. Eng. 8 (2006) 455–498.

[64] J.E. Koivumäki, J. Thevenot, P. Pulkkinen, V. Kuhn, T.M. Link, F. Eckstein, T. Jämsä, Cortical bone finite element models in the estimation of experimentally measured failure loads in the proximal femur, Bone 51 (2012) 737–740.

[65] G. Holzer, G. von Skrbensky, L.A. Holzer, W. Pichl, Hip fractures and the contribution of cortical versus trabecular bone to femoral neck strength, J. Bone Miner. Res. 24 (2009) 468–474.

4

RICCI-FLOW BASED CONFORMAL MAPPING OF THE PROXIMAL FEMUR TO IDENTIFY EXERCISE LOADING EFFECTS

by

Narra N, Abe S, Dimitrov V, Nikander R, Kouhia R, Sievänen H & Hyttinen J,

(*Submitted*)